9-30-1996

Design of a Two-Chamber-NO_2-Fluorescence-Cell

Volker Schmid
Portland State University

Recommended Citation
Schmid, Volker, "Design of a Two-Chamber-NO_2-Fluorescence-Cell" (1996). *Dissertations and Theses.* Paper 5263.
https://doi.org/10.15760/etd.7136

THESIS APPROVAL

The abstract and thesis of Volker Schmid for the Master of Science in Physics were presented September 30, 1996 and accepted by the thesis committee and the department.

COMMITTEE APPROVALS:

[redacted]
Robert J. O'Brien, Chair

[redacted]
Erik Bodegom

[redacted]
M. Aslam K. Khalil

[redacted]
Gerhard Recktenwald
Representative of the Office
of Graduate Studies

DEPARTMENT APPROVAL:

[redacted]
Erik Bodegom, Chair
Department of Physics

****

ACCEPTED FOR PORTLAND STATE UNIVERSITY BY THE LIBRARY

by [redacted] on 13 Dec. 1996

ABSTRACT

The abstract of the thesis of Volker Schmid for the Master of Science in Physics presented September 30, 1996.

Title: Design of a Two-Chamber-NO_2-Fluorescence-Cell

Nitrogen oxides control the photochemical production of ozone O_3 in the lower atmosphere and influence the concentration of the hydroxyl radical HO in the troposphere. As an important member of the nitrogen oxide family, NO_2 plays a significant role in serving as the only known source of ozone (through photolysis) in the lower atmosphere and as sink for HO via formation of nitric acid. Therefore, accurate measurements of nitrogen dioxide are essential for the understanding of the processes that determine the distribution of tropospheric ozone and for assessing the impact of human activity on the troposphere.

Although reliable and sensitive techniques for the direct measurement of nitric oxide NO have been developed, these results could not be fully applied to direct NO_2 measurements. The purpose of the present study was to further develop a low pressure laser-excited fluorescence technique for measuring NO_2 by introducing the idea of a Two-Chamber-Fluorescence-Cell. Theoretical considerations of the performance of such a cell and the flow regime within the cell were done in order to

assess the optimum cell design and the conditions for optimum operation. Measurements on a provided two-chambered test cell were done to verify the theoretical predictions made. This test cell has been explored with a Nd:YAG pumped dye laser (100mW@564nm, 30Hz) and a supplied NO_2 concentration of 100ppm.

The theoretical results suggest that the concept of a Two-Chamber-NO_2-Fluorescence-Cell yields an improved sensitivity compared to present direct techniques for measuring NO_2. In addition, experimental results give a better understanding of how to realize the initial idea of an operating Two-Chamber-NO_2-Fluorescence-Cell.

DESIGN OF A TWO-CHAMBER-NO_2-FLUORESCENCE-CELL

by

VOLKER SCHMID

A thesis submitted in partial fulfillment of the
requirements for the degree of

MASTER OF SCIENCE
in
PHYSICS

Portland State University
1996

ACKNOWLEDGMENTS

I would like to thank Dr. R.J. O'Brien for giving me the opportunity to work under his supervision without attempting to convert me into a chemist, and for sharing his never-ending flow of ideas. It was very inspiring to work for him. Special thanks to Dr. L. George for her encouragement, as well as to Dr. T.M. Hard for his knowledgeable advice on numerous topics and practical help. It was very pleasant to work with them and have their support.

I would also like to thank my fellow grad student P. Herman, and R. Zupan from the machine shop, whose work provided the basis for this project. Thanks to Eddeee and Nathan for never getting tired of correcting the spelling and grammar mistakes in my thesis, and special thanks to Andy for his generous help while preparing my thesis defense presentation.

Finally, I would like to express my deepest gratitude to my parents and family, who never lost faith in me, and provided me with great support in every situation to make all this possible.

TABLE OF CONTENTS

LIST OF FIGURES

LIST OF TABLES

CHAPTER I

INTRODUCTION

Several studies have shown that nitrogen oxides play an important role in tropospheric chemistry. NO_X (=NO+NO_2) compounds control the photochemical production of ozone O_3 and influence the concentration of the hydroxyl radical HO in the troposphere.

The crucial importance of the hydroxyl radical lies in its responsibility for the removal of a variety of atmospheric species and therefore in a prevention of large accumulations of hydrocarbons and most trace gases in the atmosphere. HO is a fragment of the very stable water molecule to which it tends to revert by abstracting a hydrogen atom from its reaction partner.

The removal of organic compounds is initiated by the oxidation with HO as follows:

$$RH + HO \text{ ---> } R + H_2O. \qquad (R1)$$

R includes any organic fragment consisting of carbon, hydrogen and other atoms such as O, N, etc.. Further reactions of the oxidized hydrocarbons involving increased aqueous solubility lead either to a rapid scavenging from the atmosphere by wet or

dry deposition, or to a complete oxidation to CO_2. Nitric acid HNO_3 and sulfuric acid H_2SO_4, formed by reaction of HO with NO_X, H_2S and SO_2 respectively, are major components of acid precipitation, which has been given credit for the widely spread *Waldsterben* in Europe, a dramatic decline of forest.

Tropospheric Ozone is of fundamental importance because of its role in the generation of the hydroxyl radical, which assures the present composition of our atmosphere.

$$O_3 + h\nu\ (\lambda \leq 310nm) \text{ ---> } O(^1D) + O_2 \qquad (R2)$$

$$O(^1D) + H_2O \text{ ---> } 2HO \qquad (R3)$$

Ozone is also reacting with alkenes producing aldehydes, ketones, and acids, as well as inorganics such as CO, CO_2, and H_2O. Due to phytotoxic and poisonous properties of Ozone, elevated Ozone levels cause damage to human and vegetative health.

By controlling the concentration of these important photochemical oxidants, increasing anthropogenic emissions of NO_X could affect the balance of the atmosphere. It becomes clear that accurate knowledge of NO_X distribution in the troposphere is essential for the understanding of the processes that determine the distribution of tropospheric ozone.

Direct measurement techniques of NO have already been achieved, which are reliable for low NO concentrations. In addition, a lot of effort has been done to extend those results on direct NO_2 measurements. Still, direct measurement

techniques for low concentrations of NO_2 lack on reliability and remain a field of study.

SOURCES OF NITROGEN DIOXIDES

Nitrogen oxides are released into the atmosphere both naturally and by anthropogenic emission. Major sources of NO_X in the troposphere appear to be fossil-fuel combustion, lightning, biomass burning, oxidation of ammonia, microbial processes in soils, input from the stratosphere and input of NO_X by stratospheric aircrafts .

Nitric oxide is produced by high temperature chemical processes during combustion of fossil fuels, from nitrogen present in fuel and from oxidation of nitrogen in the air. Smaller amounts of NO_2 are produced by the further oxidation of NO. Trace amounts of other species such as HNO_3 are also formed. The fraction of the total NO_X which is emitted as NO is often assumed to be greater than 90% [Finlayson-Pitts and Pitts, 1986].

Biomass burning is mostly associated with land clearance for agriculture in the tropics and burning of savannas, with smaller contributions from the use of wood as a fuel and from forest wild fires [Logan, 1983]. It contributes to anthropogenic as well as to natural emissions. Table 1 shows the estimated annual global anthropogenic emissions of NO_X.

Table 1. Estimated Annual Global Anthropogenic Emissions of NO_X

Source Category	Emissions[a] (10^6 metric tons per year)
Fossil fuel combustion	69
Biomass burning[b]	39
TOTAL	108

Source: Logan, 1983.
[a] Expressed as NO_2.
[b] Includes both controlled (e.g. land clearance) and uncontrolled (e.g. forest wild fires) burning.

Another source of fixed nitrogen is lightning discharge, which provides together with microbial activity in soils the largest natural sources for NO_X, although the amount of their contribution has been a topic of controversy.

Stratospheric injection of nitrogen oxides is possible due to their production in the stratosphere by reaction of $O(^1D)$ with nitrous oxide N_2O, which is emitted via microbial processes in soil and natural waters. N_2O does not contribute to photochemistry in the troposphere by direct photolysis and is chemically inactive there, but it plays an important role in controlling stratospheric ozone concentrations and is recognized as a chemically and radiatively active greenhouse gas [US EPA,1994].

Input of NO_X by stratospheric aircrafts is estimated to contribute an amount comparable to the injection from the stratosphere and has only a small effect on ozone concentrations in the troposphere [Crutzen and Gidel, 1983]. Remaining sources of NO_X are oxidation of ammonia in the atmosphere, emissions due to volcanic eruptions and contributions from the world's oceans. Contribution from NO_X due to volcanic eruptions and input from the oceans are assumed to be rather small. Major natural sources of NO_X and estimated emissions are shown in Table 2.

Table 2. Major Natural sources of NO_X and Estimated Emissions[a]

Source	Emissions[a] (10^6 metric tons per year) Stedman and Shetter (1983)	Logan (1983)
Lightning	10	10
Stratospheric injection	3	2
Ammonia oxidation	3	3-33
Biomass burning[b]	16	39
Soil emission	33	26
TOTAL	65	96-126

[a] Expressed as NO_2.
[b] Includes both controlled (e.g. land clearance) and uncontrolled (e.g. forest wild fires) burning.

CHEMISTRY OF THE TROPOSPHERE

Nitrogen oxides are emitted primarily in the troposphere in the form of nitric oxide. NO reacts with ozone to form nitrogen dioxide. Solar radiation dissociates the formerly formed NO_2 and the released oxygen atom can react with O_2 regenerating ozone.

$$NO + O_3 \text{ ---> } NO_2 + O_2 \qquad \text{(R4)}$$

$$NO_2 + h\nu \text{ ---> } NO + O \qquad \text{(R5)}$$

$$O + O_2 + M \text{ ---> } O_3 + M \qquad \text{(R6)}$$

These three rapid reactions are known as the O_3-NO-NO_2 photostationary state. However the three reactions shown above do not result in a net production of ozone. The nullcycle of the photostationary state above could be altered by the occurrence of significant side reactions which can lead to a loss or production of ozone [Calvert and Stockwell, 1983].

The possible conversion of nitric oxide to NO_2 by reaction with hydroperoxyl and the organic peroxy radical (reaction R8 and R9) could bypass the ozone consumption reaction R4. This enables nitric oxide to be oxidized to nitrogen dioxide without destroying ozone.

$$R + O_2 + M \text{ ---> } RO_2 + M \qquad (R7)$$

$$RO_2 + NO \text{ ---> } NO_2 + RO \qquad (R8)$$

$$HO_2 + NO \text{ ---> } NO_2 + OH \qquad (R9)$$

Therefore sufficiently high sources of NO_X (above ~30ppt [Logan, 1983]) are able to generate enhanced ozone concentrations in the troposphere. Reaction R9 also plays an important role in the chemistry of the hydroxyl radical by converting HO_2 into HO.

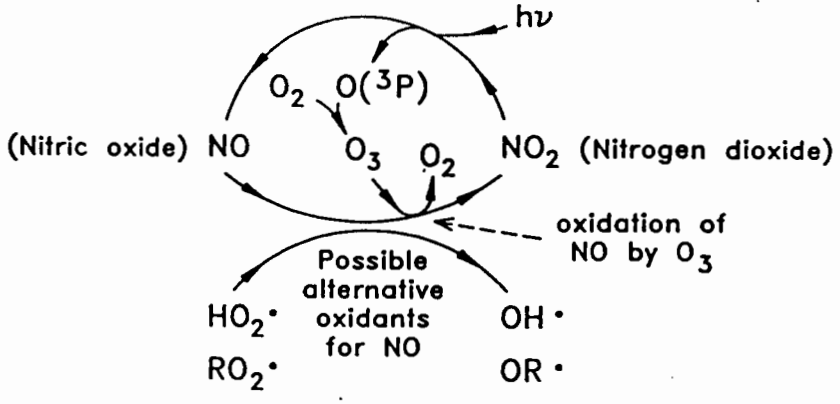

Figure 1. The NO_X-ozone cycle. The cycle is driven by sunlight; brown-colored nitrogen dioxide gas (NO_2) absorbs a photon and is dissociated into nitric oxide (NO) and a highly reactive oxygen atom, which combines with an oxygen molecule to form ozone (O_3). The ozone can be reduced back to O_2 by reaction with nitric oxide. O_3 cannot exceed the amount of nitrogen oxides in the air unless an alternative means of regenerating NO_2 exist; this can be provided by free radicals such as HO_2 or RO_2 in hydrocarbon-contaminated air [Hemond and Fechner, 1994].

Another considerable contribution of NO_X to generation of ozone occurs due to its role as a catalyst in ozone-producing reaction cycles in the troposphere. Such reaction cycles clearly occur during photochemical smog episodes, but they should also take place in the background troposphere during the oxidation of CO, CH_4, and nonmethan hydrocarbons, if sufficient NO is present [Crutzen and Gidel, 1983].

The removal of nitrogen oxides takes place by their conversion to nitric acid.

$$HO + NO_2 + M \text{ ---> } HNO_3 + M \qquad \text{(R10)}$$

By means of its high solubility in water, rainout (wet deposition) or surface (or dry) deposition of HNO_3 are the most important removal processes of NO_X in the troposphere. Due to these processes the lifetime of NO_X varies in a range of hours to a couple of days [Logan, 1983]. Surface removal of HNO_3 and NO_2 dominates removal by precipitation in the vicinity of sources. However, when averaged globally surface removal seems to compete in magnitude with wet deposition of nitrate. Surface deposition of NO_2 (and to a lesser extent of NO) leads also to loss of NO_X in the troposphere. A simplified nitrogen oxide reaction scheme is illustrated in Figure 2.

An important influence on NO_X levels in the remote troposphere is long range transport of bound nitrogen from polluted or source areas. Organic nitrates have been recognized to serve as temporary reservoir of nitrogen oxides.

$$RO_2 + NO \text{ ---> } RONO_2 \qquad \text{(R11)}$$

$$RO_2 + NO_2 \text{ ---> } ROONO_2 \qquad \text{(R12)}$$

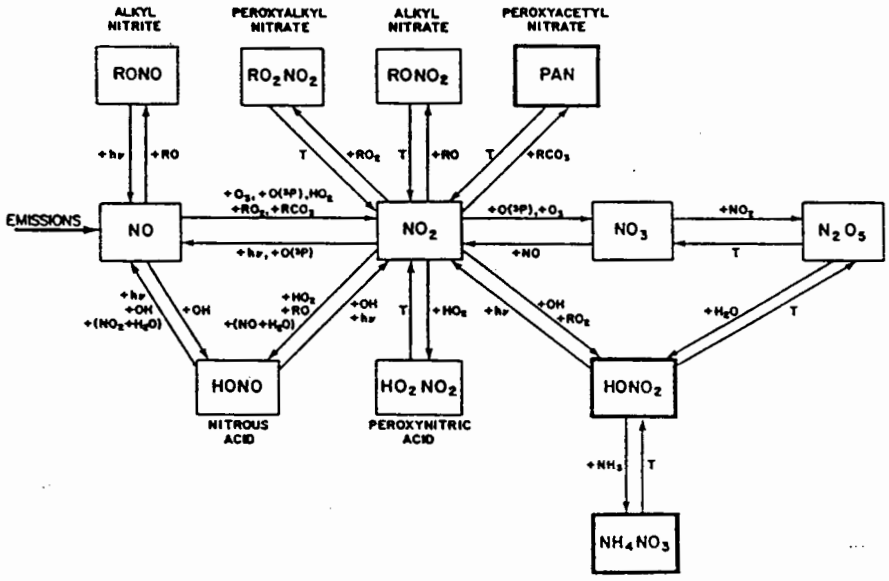

Figure 2. Simplified nitrogen oxide reaction scheme [Seinfeld, 1986].

Of special interest among the organic nitrate is peroxyacetyl nitrate (PAN), the most important organic nitrate in tropospheric chemistry. Also of significant importance is peroxypropionyl (PPN) which is produced in ambient air but at lesser concentrations than PAN. Nitrogen oxides present in the form of PAN can be as much or more abundant than the inorganic form [Singh *et al.*, 1985]. Photolysis of PAN appears to be negligible compared to thermal decomposition, and its lifetime with respect to photolysis in the troposphere ranges from 55-193 days [Finlayson-Pitt and Pitt, 1986]. Therefore PAN is a significant reservoir for NO_Y (= NO_X + HNO_2 + HNO_3 + HO_2NO_2 + NO_3 + N_2O_5 + PAN + particulate nitrates) in urban areas as well as in the middle and upper troposphere, where acetylperoxy radicals may be available through the decomposition of C_2H_6 and C_3H_8 [Logan, 1983]. PAN is toxic and

irritating, capable of causing health effects and damage to materials. Peroxynitric acid (HO_2NO_2) can serve as reservoir for NO_2 at low temperatures, reaction R 14 .

Temporary reservoir species NO_Y can release NO or NO_2 via reactions R 13 - R 17, and provide by this means the generation of tropospheric ozone via photolysis of NO_2. This leads to ozone formation in regions remote from NO_X sources.

$$RO_2NO_2 \text{ ---> } RO_2 + NO_2 \quad \text{(R13)}$$

$$HO_2NO_2 \text{ ---> } HO_2 + NO_2 \quad \text{(R14)}$$

$$N_2O_5 + h\nu \text{ ---> } NO_2 + NO_3 \quad \text{(R15)}$$

$$NO_3 + h\nu \text{ ---> } NO_2 + O \quad \text{(R16)}$$

$$NO_3 + h\nu \text{ ---> } NO + O_2 \quad \text{(R17)}$$

Due to the significant anthropogenic influence on the tropospheric sources of NO_X and a possible long range transport of NO_X to remote areas, increasing tropospheric ozone levels are conceivable.

FLUORESCENCE SPECTRUM OF NITROGEN DIOXIDE

One possible method to monitor atmospheric NO_2 is to take advantage of certain features of its fluorescence. The fluorescence spectrum of nitrogen dioxide is very complex and has withstood its full analysis. It consists of sharp bands superimposed on an apparent continuum.

Ab initio calculations predict four electronic states, $^2A_1$, $^2B_2$, $^2B_1$ and $^2A_2$ which can all interact with each other and contribute to the spectrum in the visible

region. Figure 3 shows electronic energy as a function of bond angle for the low-lying electronic states of NO_2.

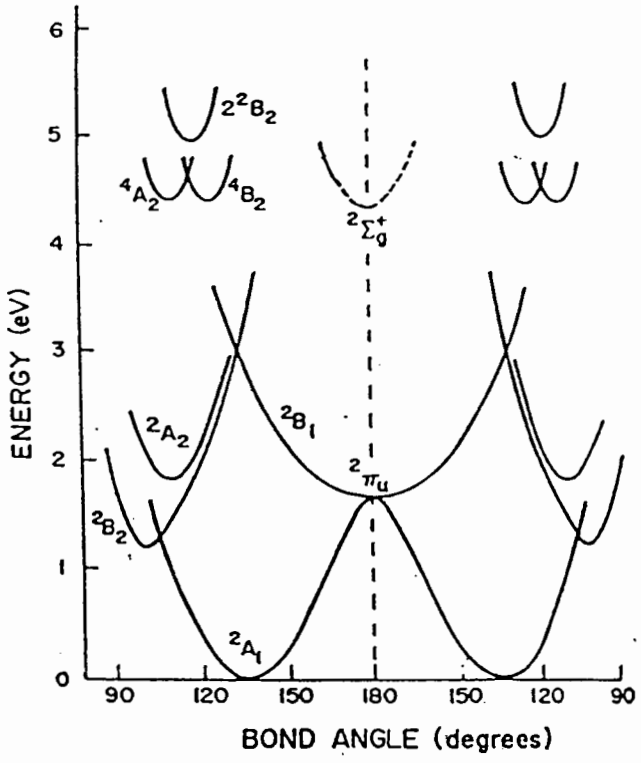

Figure 3. NO_2 energy level diagram. [Gillespie *et al.*, 1975]

High-lying vibronic levels of the $^2A_1$ ground state are mixed with vibronic levels of the excited electronic states, causing perturbations of these states and or formation of mixed states. The perturbed $^2B_2$ state has been found to be responsible for the most of the intensity emitted in the visible and near infrared region of the spectrum. Another contribution has been suggested to come from the $^2B_1$ state.

The sharp banded structure in the visible spectra of NO_2 has been predicted and shown to originate from the two major band systems in this region: the $^2B_2$ - $^2A_1$

and $^2B_1$ -$^2A_1$ system. The continuum of NO_2 fluorescence has been a field of intense study and controversy. It has been believed that this quasicontinuum arises from overlapping vibronic bands in high density, due to vibronic coupling between the electronic states, and mixing and perturbation of those states causing deterioration of selection rules and forbidden transitions. A histogram of the vibronic band origins in the spectral range from 14879.8cm^{-1} to 17518.1cm^{-1} with corresponding band intensities can be seen in Figure 4.

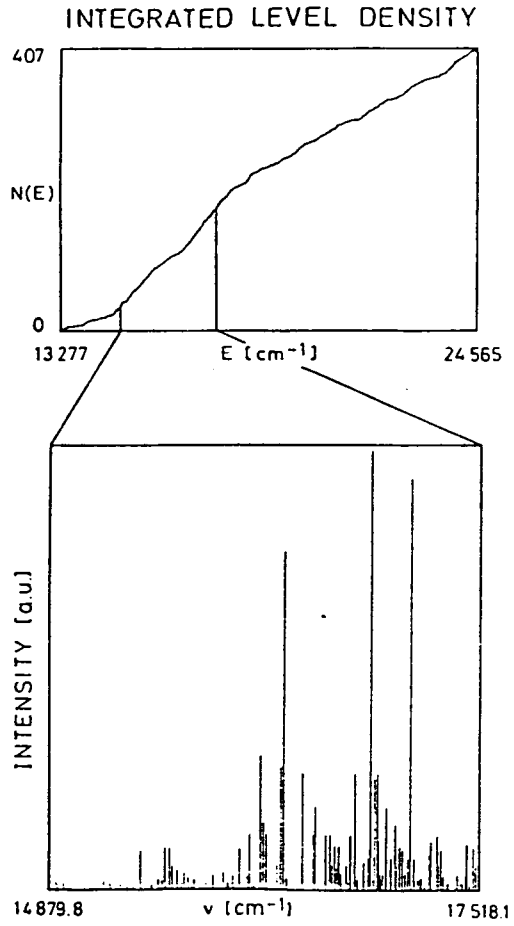

Figure 4. a) Integrated level density
b) Histogram of vibronic band origins in the spectral range from 14879.8cm^{-1} to 17518.1cm^{-1} with the corresponding band intensities [Persch *et al.*, 1988].

Another still not fully resolved anomaly of NO_2 fluorescence is that the perturbed upper electronic states exhibit fluorescence lifetimes more than two orders of magnitude longer than the values calculated from their integrated absorption coefficient. This anomaly has been explained in terms of the complex processes mentioned above, but still remains a field of study.

MEASURING TECHNIQUES FOR NITROGEN DIOXIDE

In order to monitor low concentrations of NO_2, several measurement techniques have been accomplished and have been a field of extensive research. Detection of NO_2 is possible by using direct and indirect methods. Techniques based on NO determination have been generally used for indirect measurement techniques. NO_2 is converted to NO by photolytic, thermal or chemical techniques. The detection of NO is realized by monitoring the chemiluminescence from electronically excited NO_2 formed by reaction of nitric oxide with ozone [Kley and Mc.Fahrland, 1980]. Although very sensitive and accurate, nitric oxide chemiluminescence (NO-CL) suffers from interference of certain tropospheric nitrogen species. This interference occurs mainly in highly polluted locations [Fehsenfeld *et al.*, 1990]. Another source of uncertainty is the conversion of NO_2 into NO, since other members of the NO_y family get converted as well.

Another technique for measuring low concentrations of NO_2 is provided by the Two-Photon Laser-Induced Fluorescence methology (TP-LIF) is [Bradshaw *et*

al., 1985]. Recent measurements were accomplished by photofragmentation of NO_2 via a laser and following quantitative detection of the NO fragment by using the TP-LIF [Sandholm *et al.*,1990].

Various direct measurements of NO_2 have been developed, e.g. the long path optical absorption and tunable diode laser absorption spectroscopy (TDLAS) [Fehsenfeld *et al.*, 1990]. However, the time resolution of those methods is limited by long spatial and temporal averaging.

By using the laser excited fluorescence (LEF) technique at low pressures [George *et al.*, 1991], it has been shown, that direct measurements of low concentration of NO_2 are possible with sensitivities comparable with the techniques mentioned above. Kinetical studies of systems perturbed from the equilibrium state provide suitable averaging times which depend on the relaxation time of the system. Employing the low pressure LEF technique, problems due to conversion of NO_2 to NO for indirect NO_2-CL or background problems do not exist or are limited. Problems occur when species other than NO_2 absorb at the same wavelength and fluoresce with similar lifetimes. But due to the broad spectrum of NO_2, suitable excitation wavelengths can be chosen. This technique has a great potential for further research.

A ground-based intercomparison of NO_2 measurements compared indirect techniques (photolysis/ NO-chemiluminescence and the Luminox detector) with a direct method (TDLAS) for detection of NO_2 [Fehsenfeld *et al.*, 1990]. Similar results for all three instruments were reported for NO_2 concentrations above 2ppbv.

The photolysis/NO-CL and TDLAS instruments showed further agreement only for NO_2 concentrations greater than 0.4ppbv.

An intercomparison of airborne NO_2 measurements involved two indirect techniques (two-photon NO laser-induced fluorescence system with laser photolysis of NO_2 to NO, an NO/O_3 chemiluminescence detector with arc lamp photolysis of NO_2 to NO and one using $FeSO_4$ for conversion of NO_2 to NO) and one direct technique (TDLAS) [Gregory *et al.*,1990]. The instrument using $FeSO_4$ for NO_2 conversion was excluded later due to its behavior of converting PAN to NO and therefore providing an artifact signal. For mixing ratios to 100 or 200pptv data sets showed a 30-40% correlation among the different techniques. However, when data sets were restricted to mixing ratios smaller than 50pptv, little correlation among the measurements was observed [Gregory *et al.*,1990]. Further results indicated that at all observed concentrations the correlation among the two indirect techniques was better than their correlation to the direct technique.

With further refinement of the low pressure LEF technique [George *et al.*, 1991], a highly sensitive method for NO_2 detection might be developed, which could provide new insight into the question of reliability of the direct and indirect techniques.

CHAPTER II

DEVELOPMENT OF A TWO-CHAMBER-NO_2-FLUORESCENCE-CELL

The idea of the Two-Chamber-NO_2-Fluorescence-Cell is mainly based on the FAGE technique (Fluorescence Assay by Gas Expansion), [Hard *et al.*, 1984], used for determination of NO_2 [George *et al.*, 1991]. This technique involves the low pressure excitation of NO_2 to an upper electronic state by a light source of appropriate wavelength and the subsequent detection of its fluorescence. Based on the results, it has been shown, that a direct, low pressure, laser induced fluorescence technique can be developed for detecting NO_2 at low concentrations. In order to be able to detect NO_2 with its relatively low fluorescence yield, high photon excitation rates are required. These can be provided by laser. However, laser excitation results in a large background pulse due to Rayleigh, Raman and Mie scattering of the sample to be detected as well as scattering of photons off the components of the detection cell.

In order to limit and reduce the background signal and its negative influence on the detection system, e.g. saturation of the photomultiplier tube (PMT), the technique takes advantage of the temporal characteristics of the scattering and fluorescence processes. While the scattering of photons occurs simultaneously with

the laser pulse, the fluorescence of NO_2 persists longer due to excitation at low pressure. The fluorescence decay follows Equation 1,

$$N = N_0 \exp\left[-\frac{t}{\tau_{eff}}\right] \tag{1}$$

where N is the number of detected fluorescent photons and the τ_{eff} effective lifetime of the NO_2 excited state in presence of collisions with foreign gas molecules [Kirzinis *et al.*, 1984]. Since NO_2 fluorescence originates from different states, all those excited states contribute to the effective fluorescence lifetime. The effective fluorescence lifetime can be calculated with

$$\tau_{eff} = \frac{1}{\left(k_q[M] + k_f\right)} \tag{2}$$

where k_q represents the quenching rate constant and k_f the rate constant for spontaneous emission.

Operating at low pressure reduces collisional quenching and therefore causes a lengthening of the fluorescence lifetime. This can be seen in Figure 5. By detection of the fluorescence at a certain time after the laser pulse, the background due to scattering can be reduced. Since Rayleigh and Mie scattering depend proportionally on the pressure, scattering is also reduced with decreasing pressure.

In addition to the temporal discrimination between scattered and fluorescence photons achieved with the FAGE-NO_2 technique, the Two-Chamber-Detection-Cell also provides a spatial discrimination by separating the respective excitation and detection zones from each other. This contributes to a higher sensitivity of the system

since heavy saturation effects of the PMT are mostly removed by positioning the PMT at a distance from the excitation zone and therefore away from the laser beam. Hereby only a fraction of the initially scattered photons gets detected. Saturation effects are minimized.

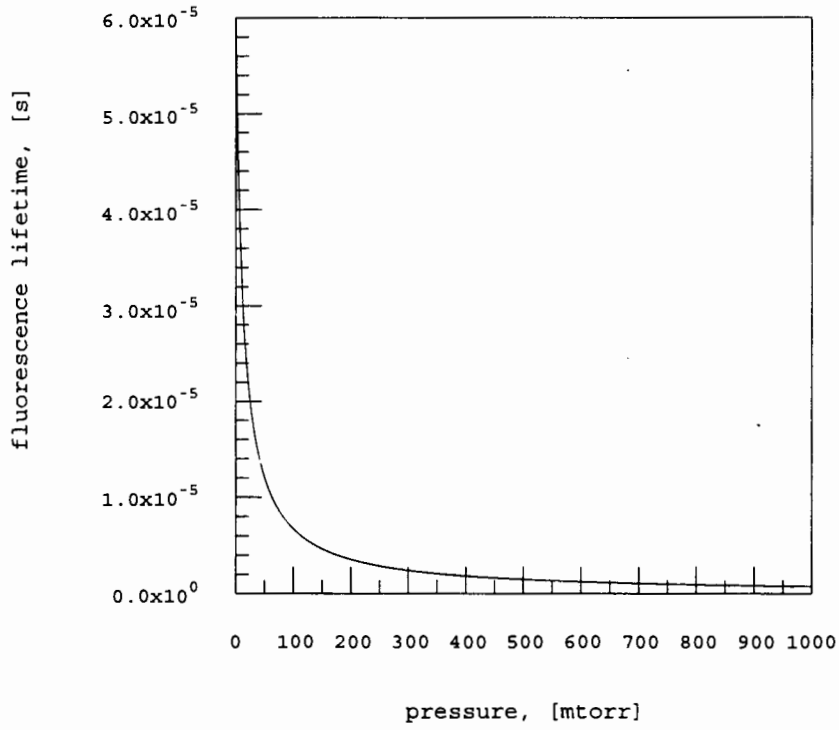

Figure 5. Effective fluorescence lifetime versus pressure.

Since the fluorescence lifetime is increased and the lifetime of the background decreased with reduced pressure, it follows that an optimal signal-to-noise ratio (SNR) can be obtained at some value of the reduced pressure. One limit in reducing cell pressure is reached when a significant fraction of the emitting target molecules

radiate (rate constant k_f) *vs.* undergoing quenching (rate constant k_q). This limit is related to the half-quenching pressure of the target species ($[M_{1/2}]= k_f/ k_q$), at which pressure half the excited molecules fluoresce while half are quenched. At this point the fluorescence signal has dropped by one half relative to its value at atmospheric pressure [George *et al.*, 1991].

Figure 6 shows an abstracted profile of the Two-Chamber-Detection-Cell. Inflowing NO_2 molecules are excited in the excitation chamber to an upper electronic state by a laser pulse with appropriate wavelength crossing the flow perpendicular. The fluorescing NO_2 molecules flow into the detection chamber where their fluorescence is detected by a PMT, and then flow out toward the vacuum pump.

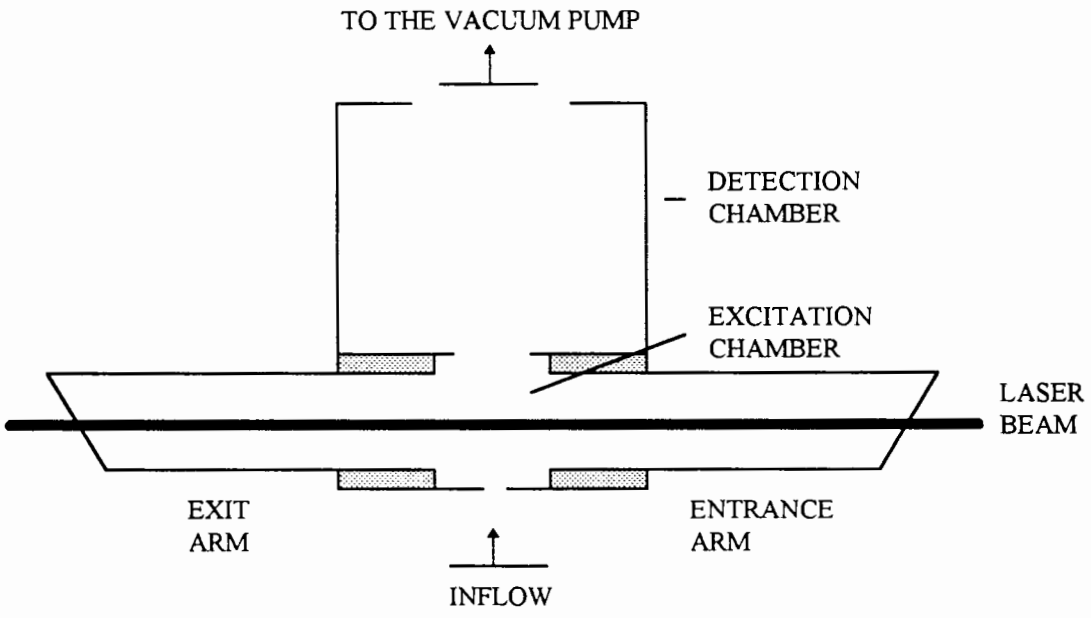

Figure 6. Abstracted profile of the Two-Chamber-Fluorescence-Cell.

FLUORESCENCE SIGNAL OF A TWO-CHAMBER-NO_2-FLUORESCENCE-CELL

In order to predict the performance of a Two-Chamber-NO_2-Fluorescence-Cell, an expression for the fluorescence signal must be found. This can be done by introducing the fluorescence signal Θ,

$$\Theta \equiv \bar{I}_0 \, \sigma_\lambda \Phi \tag{3}$$

where Θ is in photons $[NO_2]^{-1}$ s^{-1}, and $\bar{I}_0 = I_0 l$ in photons cm^2. I_0 represents the incident intensity of the laser beam, l the length with which a laser beam of a certain cross section passes the sample, σ_λ the absorption coefficient of the absorbing species and Φ the fluorescence quantum yield of the species to be detected. Maximizing the fluorescence signal with respect to the cell dimensions and chamber pressures gives an opportunity to determine the optimum operating parameters of the cell.

The fluorescence quantum yield, Φ, is defined as

$$\Phi = \frac{number \quad of \quad photons \quad emitted}{number \quad of \quad quanta \quad absorbed}. \tag{4}$$

The calculation of the fluorescence quantum yield requires consideration of the processes involved in excitation and fluorescence decay of NO_2. The following processes are relevant:

$$NO_2 + h\nu_{abs} \xrightarrow{I_a} NO_2^* \qquad \text{(R18)}$$

$$NO_2^* + M \xrightarrow{k_q} NO_2 + M \qquad \text{(R19)}$$

$$NO_2^* \xrightarrow{k_f} NO_2 + h\nu_{em} \qquad \text{(R20)}$$

where I_a represents the rate of light absorption, k_q is the quenching rate constant of the emitting state, M is the concentration of the quencher and k_f the rate constant for fluorescence emission. Only homogeneous NO_2 quenching is considered theoretically. The influence of wall quenching of NO_2^* while interacting with components of the cell has been neglected in the following considerations and remains a subject of experimental study. When the NO_2 molecule absorbs light, fluorescence and deactivation by quenching compete for the electronically excited state produced. The fluorescence decay starts immediately after excitation by the laser pulse in the excitation chamber at time t=0. The rate of disappearance of NO_2^* in the first chamber is given by

$$\frac{d[NO_2^*]}{dt} = -[NO_2^*](k_q[M_1] + k_f) \; . \qquad (5)$$

$[M_I]$ is the pressure in the first or excitation chamber. It is assumed that there is a uniform pressure in the first chamber. Integrating Equation 5 within the appropriate limits yields

$$\int_{[NO_2^*]_0}^{[NO_2^*]_1} \frac{d[NO_2^*]}{[NO_2^*]} = -\int_0^t (k_q[M_1] + k_f)dt \qquad (6)$$

$$\left[NO_2^*\right]_I = \left[NO_2^*\right]_0 \exp\left[-\left(k_q\left[M_I\right] + k_f\right)t\right] \tag{7}$$

where $[NO_2^*]_0$ is the given initial concentration of excited NO_2 molecules, $[NO_2^*]$.The rate of emission can be described by

$$\frac{d\left[h\nu_{em}\right]}{dt} = k_f\left[NO_2^*\right] . \tag{8}$$

By substituting Equation 7 into 8 and integration over the first chamber, Equation 6 becomes Equation 9.

$$\int_0^{[h\nu_{em}]_I} d\left[h\nu_{em}\right] = k_f \int_0^{tR_I} \left[NO_2^*\right]_0 \exp\left[-\left(k_q\left[M_I\right] + k_f\right)t\right]dt \tag{9}$$

The fluorescence yield of photons (FYP) from a given initial concentration of NO_2^* for the first chamber is:

$$\left[h\nu_{em}\right]_I = \frac{k_f\left[NO_2^*\right]_0}{\left(k_q\left[M_I\right] + k_f\right)}\left\{1 - \exp\left[-\left(k_q\left[M_I\right] + k_f\right)t_{RI}\right]\right\} \tag{10}$$

where t_{RI} stands for the residence time of the excited NO_2 molecules in the first chamber.

The rate of disappearance of NO_2^* in the second chamber is given by

$$\frac{d\left[NO_2^*\right]}{dt} = -\left[NO_2^*\right]\left(k_q\left[M_{II}\right] + k_f\right). \tag{11}$$

Integration of Equation 11 and substitution of Equation 7 into it, gives an expression for the loss of NO_2^* in the second chamber.

$$\int_{[NO_2^*]_I}^{[NO_2^*]_{II}} \frac{d[NO_2^*]}{[NO_2^*]} = -\left(k_q[M_{II}] + k_f\right) \int_{t_{RI}}^{t} dt \qquad (12)$$

$$[NO_2^*]_{II} = [NO_2^*]_0 \exp\left[-\left(k_q[M_I] + k_f\right)t_{RI} - \left(k_q[M_{II}] + k_f\right)t + \left(k_q[M_{II}] + k_f\right)t_{RI}\right] \qquad (13)$$

Substituting Equation 13 into Equation 8 results in the rate of emission for the second chamber.

$$\frac{d[h\nu_{em}]}{dt} = [NO_2^*]_0 \exp\left[-\left(k_q[M_I] + k_f\right)t_{RI} - \left(k_q[M_{II}] + k_f\right)t + \left(k_q[M_{II}] + k_f\right)t_{RI}\right] \qquad (14)$$

Integration of Equation 14 results finally in an equation for the FYP of the detection chamber, which can be seen in Equation 16.

$$\int_{[h\nu_{em}]_I}^{[h\nu_{em}]_{II}} d[h\nu_{em}] = k_f [NO_2^*]_0 \exp\left[k_q t_{RI}\left([M_{II}] - [M_I]\right)\right] \int_{t_{RI}}^{t_{RII}} \exp\left[-\left(k_q[M_{II}] + k_f\right)t\right] dt \qquad (15)$$

$$[h\nu_{em}]_{II} = \frac{k_f[NO_2^*]_0}{\left(k_q[M_{II}] + k_f\right)} \left\{\exp\left[-\left(k_q[M_I] + k_f\right)t_{RI}\right] - \exp\left[-\left(k_q[M_{II}] + k_f\right)t_{RII} + \left([M_{II}] - [M_I]\right)k_q t_{RI}\right]\right\} \qquad (16)$$

$[M_{II}]$ is the pressure in the detection chamber and is assumed to be uniform, and t_{RII} represents the residence time of the excited NO_2 molecules in the detection chamber.

Photons emitted in the first chamber do not get into the second chamber and therefore do not contribute to the FYP calculated for the second chamber. This assumption seems to be reasonable, since the cell geometry indicates that the number of photons which make it over to the second chamber by multiple reflection off the black coated cell walls appears to be negligible. The same assumption is made for photons that are emitted after the remaining excited NO_2 molecules leave the

detection chamber. Emitted photons originating from the first chamber or the connection to the pump would result in an offset to the FYP of the second chamber.

The initial concentration of the excited NO_2 molecules, that is the concentration at the end of the laser pulse, can be calculated starting from Beer's Law.

$$I_{abs} = I_0\left(1 - \exp\left[-\sigma_\lambda l\left[NO_2\right]\right]\right) \tag{17}$$

I_{abs} represents the photons absorbed per unit volume and time, I_0 the incident intensity, l the length with which a laser beam of a certain cross section passes the sample and σ_λ the absorption coefficient of the absorbing species. For small concentrations of $[NO_2]$ the expression can be rewritten in good approximation as

$$I_{abs} = I_0\sigma_\lambda l\left[NO_2\right]. \tag{18}$$

This gives an explicit expression for the number of NO_2 molecules excited at the end of a laser pulse with duration Δt,

$$\left[NO_2^*\right]_0 = I_0\Delta t\sigma_\lambda l\left[NO_2\right]. \tag{19}$$

In order to find an expression for the residence time of the target species in a reaction vessel with a fixed volume, two extreme cases can be considered. The first case is called exponential dilution and is characterized by a well mixed reaction chamber. Gases flowing into the reaction chamber get mixed instantaneously and are homogeneously distributed over the whole volume of the chamber. The residence

time is therefore a function of the volume, $V_{chamber}$, of the reaction vessel and the volume flow out of the vessel, $\dot{V}_{exit}$, and can be represented by

$$t_R = \frac{V_{chamber}}{\dot{V}_{exit}} . \tag{20}$$

In contrast to the first case, there is no mixing of the inflowing gases in the second case, called plug flow. Rather all species remain in their flow regime and its vicinity. The residence time of the plug flow case is characterized by the volume of the flow, V_{flow}, and the volume flow out of the vessel, $\dot{V}_{exit}$, and can be calculated as follows:

$$t_R = \frac{V_{flow}}{\dot{V}_{exit}} . \tag{21}$$

All other possible cases are an intermediate both of these extremes and require more complex considerations [Mehrabzadeh *et al.*, 1983].

As mentioned earlier, NO_2 molecules that are excited in the first chamber have to flow into the second chamber in order to detect their fluorescence decay. Since fluorescence is a time limited process, this has to occur before all excited molecules decay. To achieve this, a plug flow regime in the excitation chamber is desired. The large difference between the pressure inside the first chamber and ambient pressure results in a choked flow through the inflow nozzle and a jet expansion occurring outside the nozzle. The volume flow through a choked nozzle is given by

$$\dot{V} = 6283\,l r_0^{\,2} \tag{22}$$

where r_0 represents the radius of the nozzle (in cm) [Guthrie,1963]. Using the fact that $\dot{V}p = const.$ for a closed system, the volume flow out of the first chamber is characterized by

$$\dot{V}_{exit} = \frac{6283\,1 r_0^{\,2}[M_0]}{[M_1]}. \tag{23}$$

The shape of the occurring flow outside the nozzle resembles an expanding cone. This results in an geometrical expression for the volume of the flow in the first chamber

$$V = \frac{\Pi r_1^{\,2} l_1}{3}. \tag{24}$$

r_1 is the radius of the cone before entering the second chamber and l_1 is the length of the first chamber. By combining Equations 21, 23 and 24 àn expression for the residence time in the first chamber can be found.

$$t_{R1} = \frac{\Pi r_1^{\,2} l_1 [M_1]}{188493 r_0^{\,2}[M_0]} \tag{25}$$

However, an exponential dilution regime would be most desirable for the second chamber. Resultant longer residence times would ensure that a large fraction of excited NO_2 molecules decays within the detection chamber, except of those that are quenched by possible wall quenching while interacting with components of the cell. Similar considerations to the above lead to the following equation for the residence time in the second chamber for a flow regime characterized by exponential dilution.

$$t_{RII} = \frac{V_{chamber}\left[M_{II}\right]}{6283\,1r_0^{2}\left[M_0\right]} \tag{26}$$

As mentioned above, due to the given differences between the ambient pressure and the pressure in the first chamber, the gas flowing into the Two-Chamber-Detection-Cell undergoes a rapid jet expansion. This behavior is considered in more detail in the next section. Entering the first chamber, the jet becomes supersonic and goes through a standing normal shock wave at a certain distance downstream of the nozzle exit. It has been shown that the pressure behind the normal shock is about equal to the chamber pressure in the first chamber [Davidor, 1971]. Assuming an adiabatic expansion and using the ideal gas law, the concentration of NO_2 in the expanding jet after the standing normal shock wave is

$$\left[NO_2\right] = \left[NO_2\right]_0 \frac{p_1 T_0}{p_0 T_1}. \tag{27}$$

p_0 and p_1 represent the ambient pressure and the total pressure in the first chamber respectively, $[NO_2]_0$ is the initial concentration of NO_2 and $[NO_2]$ is the concentration in the first chamber. The absolute temperature in the jet after passing the normal shock is only slightly lower than the temperature of the flow, before entering the cell through the nozzle [Di Rosa *et al*, 1993]. Therefore Equation 27 can be simplified to

$$\left[NO_2\right] = \left[NO_2\right]_0 \frac{p_1}{p_0}. \tag{28}$$

In case the simplification of equal temperature in the whole cell fails, Equation 28 would still give a lower estimate of the NO_2 concentration present in the excitation chamber of the cell.

Finally, the fluorescence quantum yield, Φ, which is defined in Equation 4, can be written as:

$$\Phi = \frac{k_f[M_I]}{\left(k_q[M_{II}]+k_f\right)[M_0]}\left\{exp\left[-\left(k_q[M_I]+k_f\right)t_{RI}\right] - exp\left[-\left(k_q[M_{II}]+k_f\right)t_{RII} + \left([M_{II}]-[M_I]\right)t_{RI}k_q\right]\right\} \quad (29)$$

where t_{RI} and t_{RII} are taken from Equations 25 and 26 respectively.

Substituting Equation 29 into Equation 3 and using different pressure units (mtorr) leads to

$$\Theta = \frac{\bar{I}_0 \sigma_\lambda k_f p_1}{\left(\frac{k_q 0.133 p_2 N_a}{RT}+k_f\right)p_0}\left\{\begin{array}{l} exp\left[-\left(\frac{k_q 0.133 p_1 N_a}{RT}+k_f\right)\frac{V_{flowI}\,p_1}{62831 r_0^2 p_0}\right] \\ -exp\left[-\left(\frac{k_q 0.133 p_2 N_a}{RT}+k_f\right)\frac{V_{chII}\,p_2}{62831 r_0^2 p_0}+(p_2-p_1)\frac{V_{flowI}\,k_q 0.133 p_1 N_a}{62831 r_0^2 p_0 RT}\right] \end{array}\right\} \quad (30)$$

where r_0 is the radius of the inflow nozzle, in cm, V_{flowI} the volume of the flow in the first chamber, in cm^3, and V_{chII} the volume of the second chamber, in cm^3. N_a represents Avogadro's number. The pressures p_0, p_1 and p_2 are in mtorr. p_0 is set to be 760torr.

As mentioned at the beginning of this section, to obtain a highly sensitive detection device, the fluorescence signal has to be maximized. This is done with respect to the pressures in both of the chambers, the inflow through the nozzle and the geometrical shape of the whole cell. This can be done graphically. Hereby $[M_I]$ and $[M_{II}]$ are chosen to be the independent variables. However, the volume of the

flow in the excitation chamber, the volume of the detection chamber, and the radius of the inflow nozzle are set to be parameters of this function. These parameters are changed to evaluate their influence on the theoretical performance of the cell. The laser characteristics were calculated based on parameters of a laser system used in the experimental section. The laser had an average power of about 100mW@564nm, resulting in an absorption cross section, σ_λ, of 1.065 10^{-19} cm^2molec. Figures 7 to 10 show contour plots of Θ for a cell with an arbitrarily set flow volume in the first chamber V_{flowI} of 3.3cm^3, a radius r_0 of 25μm and a variable volume of the second chamber V_{chII}.

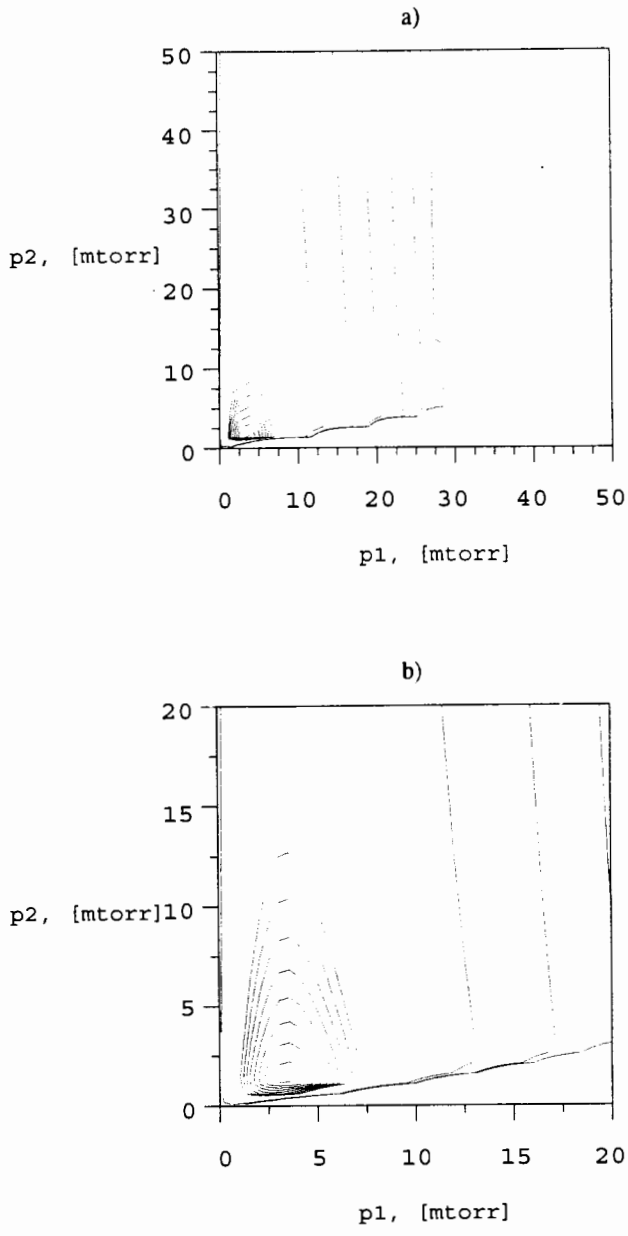

Figure 7. Contour plot of the Θ with V_{flowI}=3.3cm^3, V_{chII}=50cm^3 and r_0=25μm. The maximum Θ in the second chamber, $\Theta_{max\,II}$, is 5.29 10^{-8}photons$[NO_2]^{-1}s^{-1}$. The contours in a) represent Θ for 5.1 10^{-8},4.8 10^{-8},...,3.0 10^{-8},3.0 10^{-9},...,3.0 10^{-15}photons$[NO_2]^{-1}s^{-1}$. b) is an enlargement of a). Contours in b) represent Θ for 5.1 10^{-8},4.8 10^{-8},....,3.0 10^{-8},3.0 10^{-9}, ...,3.0 10^{-12} photons$[NO_2]^{-1}s^{-1}$.

The flow through the cell requires the pressure in the first chamber, p_1, to be larger than the pressure of the second chamber, p_2. Therefore only pressure combinations where $p_1 > p_2$ are to be considered. A maximum for this experimental set up can clearly be seen in the lower left corner of the plots. If one pressure value for p_1 is fixed and a straight vertical line is drawn from this pressure point, it can be observed that, while approaching the maximum from higher values of p_2, the spacing between the contours are considerably larger than after passing the maximum. This effect can be explained by different residence times of the excited NO_2 molecules in the second chamber. In addition, a different amount of quenching in the second chamber due to different pressures would also contribute to this behavior. Lowering p_2 is followed by small changes in quenching and a shortening of the residence time in the second chamber. This leads to slight changes in Θ until the optimum pressure of p_2 for the given set up is acquired. After passing the optimum pressure for p_2, the influence of the residence time becomes more dominant. Short residence times force the excited NO_2 molecules to pass the detection chamber before they are fully able to decay. In this case the fluorescence would mainly occur in the connection to the pump. Consequently, after passing the optimum pressure in the second chamber, Θ changes rapidly. Considering this, a different volume of the detection chamber for the same given set up of V_{flow1} and r_0 should lead to a shift in the position of the maximum Θ in the graph, which is confirmed in Figure 8.

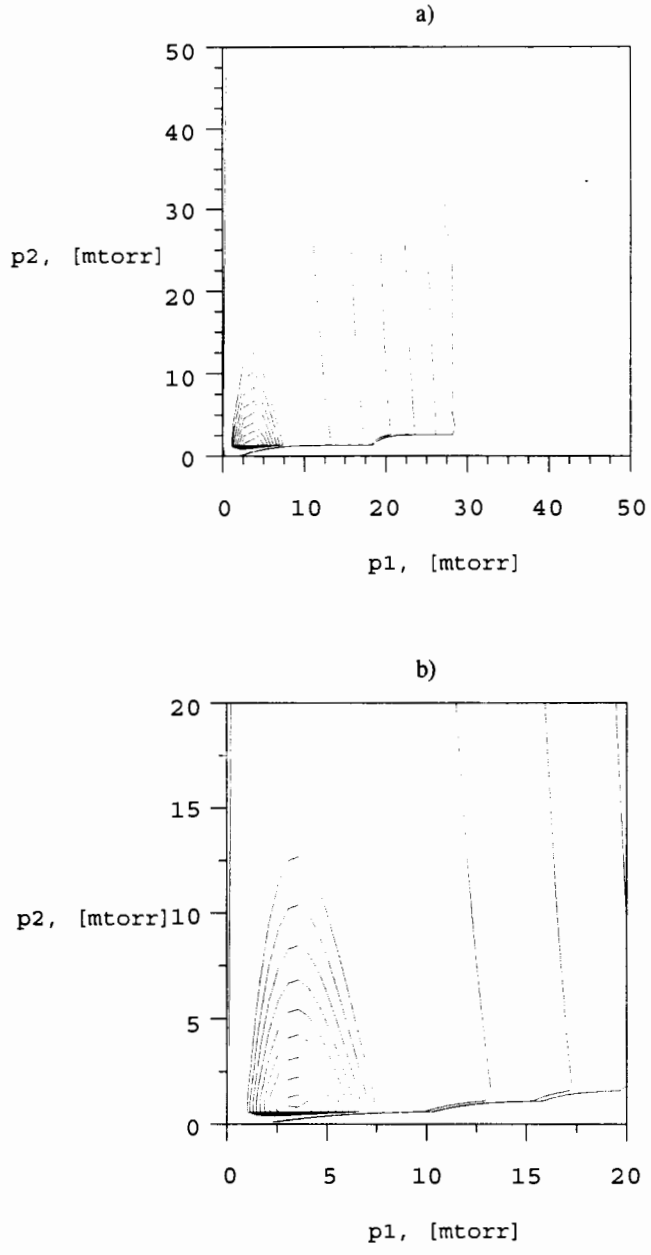

Figure 8. Contour plot of the Θ with V_{flowI}=3.3cm^3, V_{chII}=100cm^3 and r_0=25μm. The maximum Θ in the second chamber, $\Theta_{max\ II}$, is 5.53 10^{-8}photons$[NO_2]^{-1}s^{-1}$. The contours in a) represent Θ for 5.4 10^{-8},5.1 10^{-8},4.8 10^{-8}....,3.0 10^{-8},3.0 10^{-9},...,3.0 10^{-14} photons$[NO_2]^{-1}s^{-1}$. b) is an enlargement of a). Contours in b) represent Θ for 5.4 10^{-8},5.1 10^{-8},...,3.0 10^{-8}, 3.0 10^{-9},..., 3.0 10^{-12} photons$[NO_2]^{-1}s^{-1}$.

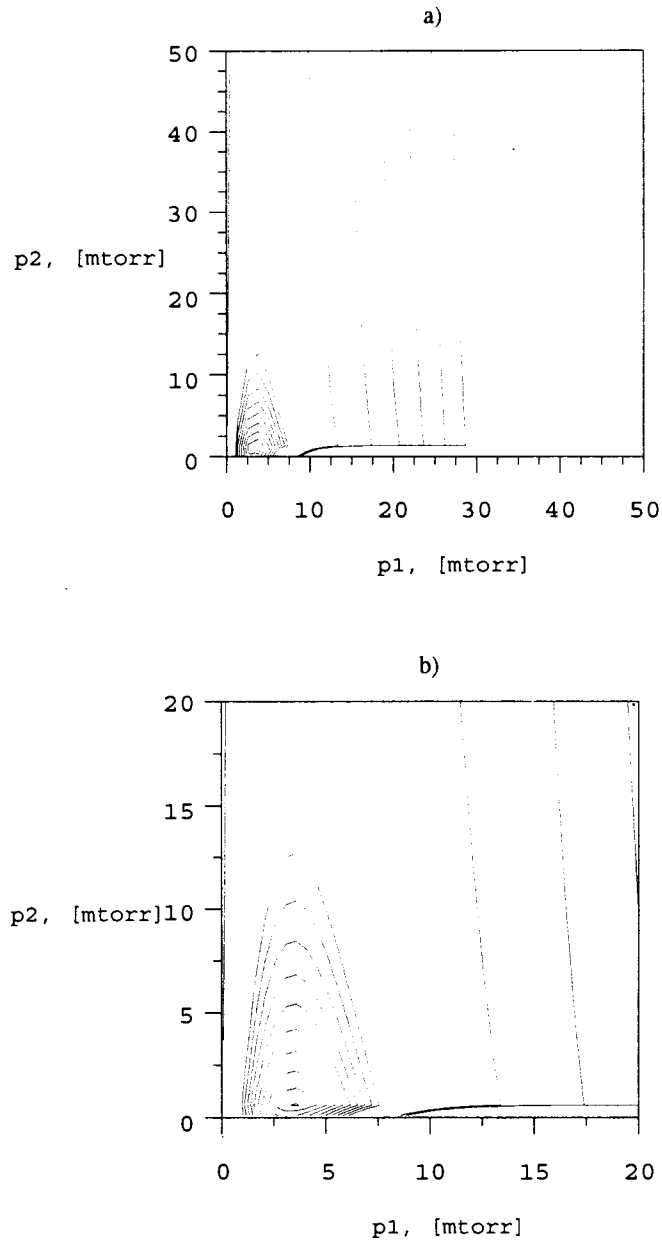

Figure 9. Contour plot of the Θ with V_{flowI}=3.3cm^3, V_{chII}=500cm^3 and r_0=25μm. The maximum Θ in the second chamber, $\Theta_{max\ II}$, is 5.77 10^{-8}photons$[NO_2]^{-1}s^{-1}$. The contours in a) represent Θ for 5.4 10^{-8},5.1 10^{-8},....,3.0 10^{-8},3.0 10^{-9},....,3.0 10^{-14} photons$[NO_2]^{-1}s^{-1}$. b) is an enlargement of a). Contours in b) represent Θ for 5.4 10^{-8},5.1 10^{-8},....,3.0 10^{-8},3.0 10^{-9} ,....,3.0 10^{-12} photons$[NO_2]^{-1}$ s^{-1}.

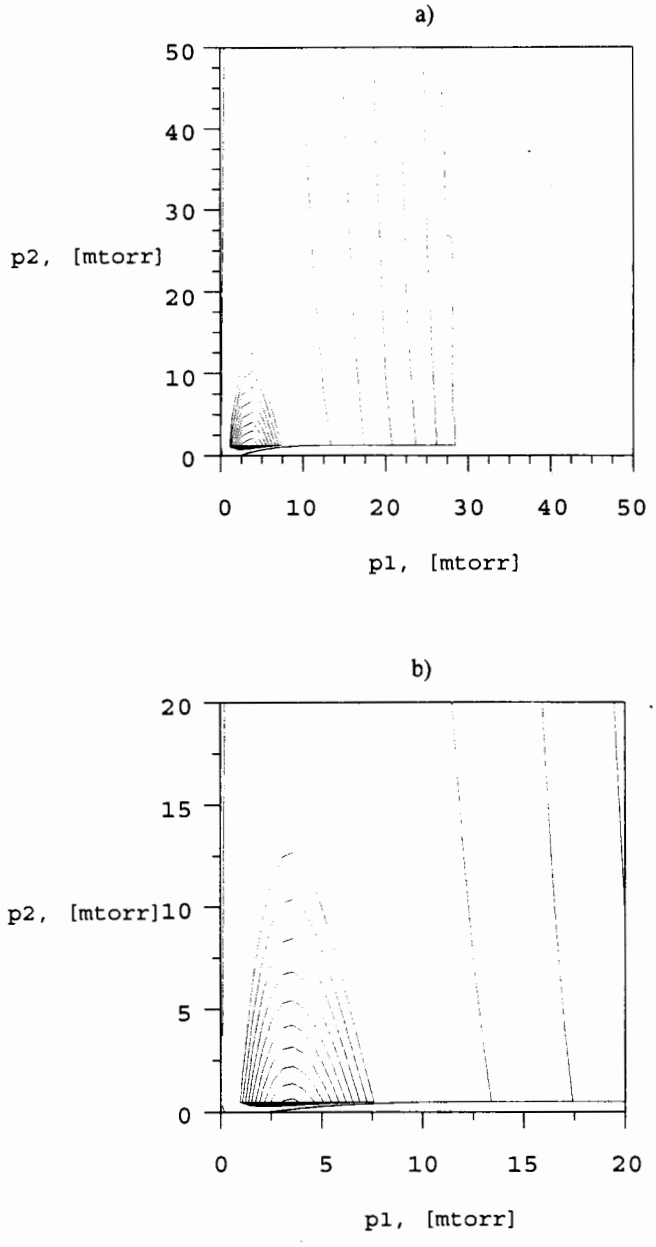

Figure 10. Contour plot of the Θ with V_{flowI}=3.3cm^3, V_{chII}=1000cm^3 and r_0=25μm. The maximum Θ in the second chamber, $\Theta_{max\ II}$, is 5.80 10^{-8}photons[NO_2]$^{-1}$s^{-1}. The contours in a) represent Θ for 5.4 10^{-8},5.1 10^{-8},....,3.0 10^{-8},3.0 10^{-9},3.0 10^{-10},....3.0 10^{-14} photons[NO_2]$^{-1}$s^{-1}. b) is an enlargement of a). Contours in b) represent Θ for 5.4 10^{-8}, 5.1 10^{-8},...,3.0 10^{-8}, 3.0 10^{-9},...,3.0 10^{-12} photons[NO_2]$^{-1}$s^{-1}.

In order to reach the optimum residence time at which the excited NO_2 molecules give off most of their fluorescence in the second chamber, the optimum pressure of p_2 has to shift toward lower values due to a chosen larger volume of the same chamber. The contour plot in Figure 8 clearly shows this behavior. Less quenching at lower pressures is responsible for the slight rise of Θ.

Further increase in volume of the second chamber leads to a further increase of Θ for this given set up, since the optimum pressure of p_2 shifts toward very small pressures. However, the increase in Θ declines permanently while the pressure of p_2 shifts toward very small values. In an infinitely large detection chamber, where all fluorescence that occurs from molecules entering the chamber would be detected, Θ would be 6.0 10^8 photons $[NO_2]^{-1}s^{-1}$ at very low pressures of p_2. The position of the maximum remains unchanged with respect to the pressure of p_1 for one given set up.

According to these results, for a set volume of flow in chamber one, V_{flow1}, and radius of the inflow nozzle, r_0, the size of the second chamber would have to be determined by the pressure combinations of p_1 and p_2 that could be accomplished by a given pumping system. In addition, it should be noted that the size of the second chamber would have to be sufficiently large to ensure high values of Θ which are close to the maximum possible Θ.

Now the influence of changes if the inflow into the cell is considered. This can be done by changing the radius of the inflow nozzle while keeping the flow volume in

the first chamber and the volume of the second chamber constant. Results are graphed in Figures 10, 11 and 12.

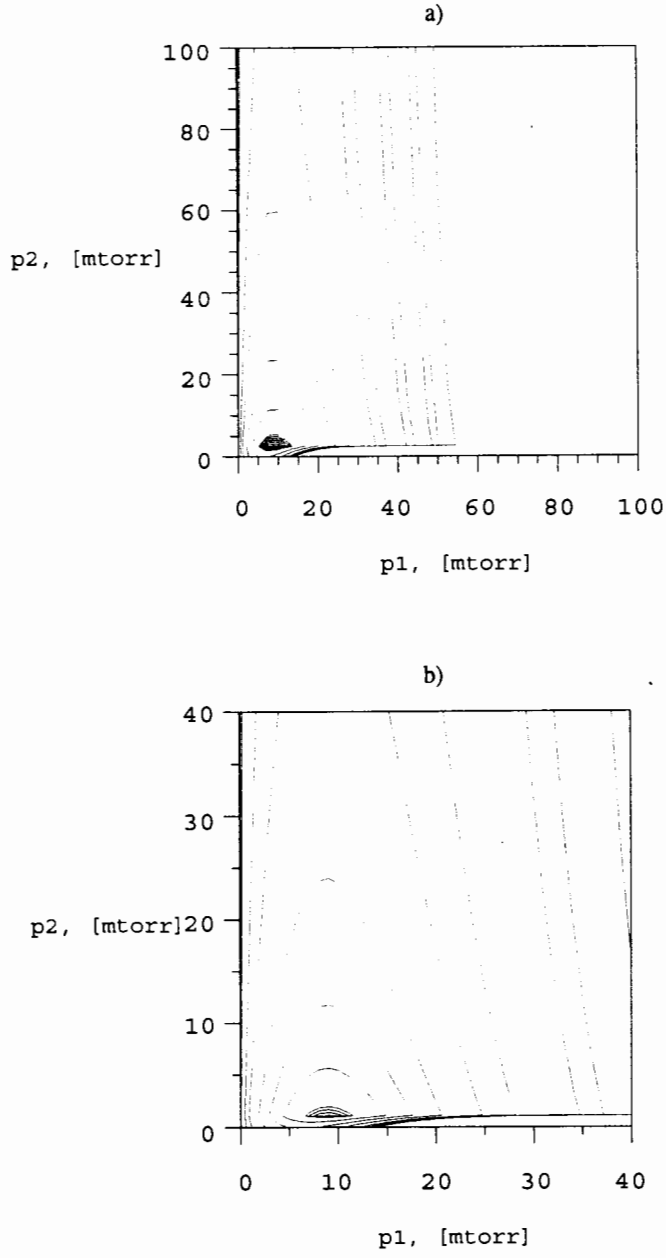

Figure 11. Contour plot of the Θ with V_{flowI}=3.3cm^3, V_{chII}=1000cm^3 and r_0=50μm. The maximum Θ in the second chamber, $\Theta_{max\ II}$, is 1.60 10^{-7} photons$[NO_2]^{-1}s^{-1}$. The contours in a) represent Θ for 1.60 10^{-7},1.57 10^{-7},1.54 10^{-7},1.51 10^{-7},1.2 10^{-7},9.0 10^{-8},...,3.0 10^{-8},6.0 10^{-8}, 3.0 10^{-8},1.5 10^{-8},3.0 10^{-9},....,1.5 10^{-11},3.0 10^{-12}photons$[NO_2]^{-1}s^{-1}$. b) is an enlargement of a). Contours in b) represent Θ for 1.60 10^{-7},1.57 10^{-7},1.54 10^{-7},1.51 10^{-7},1.2 10^{-7},9.0 10^{-8}, ...,3.0 10^{-8},6.0 10^{-8},3.0 10^{-8},1.5 10^{-8},3.0 10^{-9},1.5 10^{-9} photons$[NO_2]^{-1}s^{-1}$.

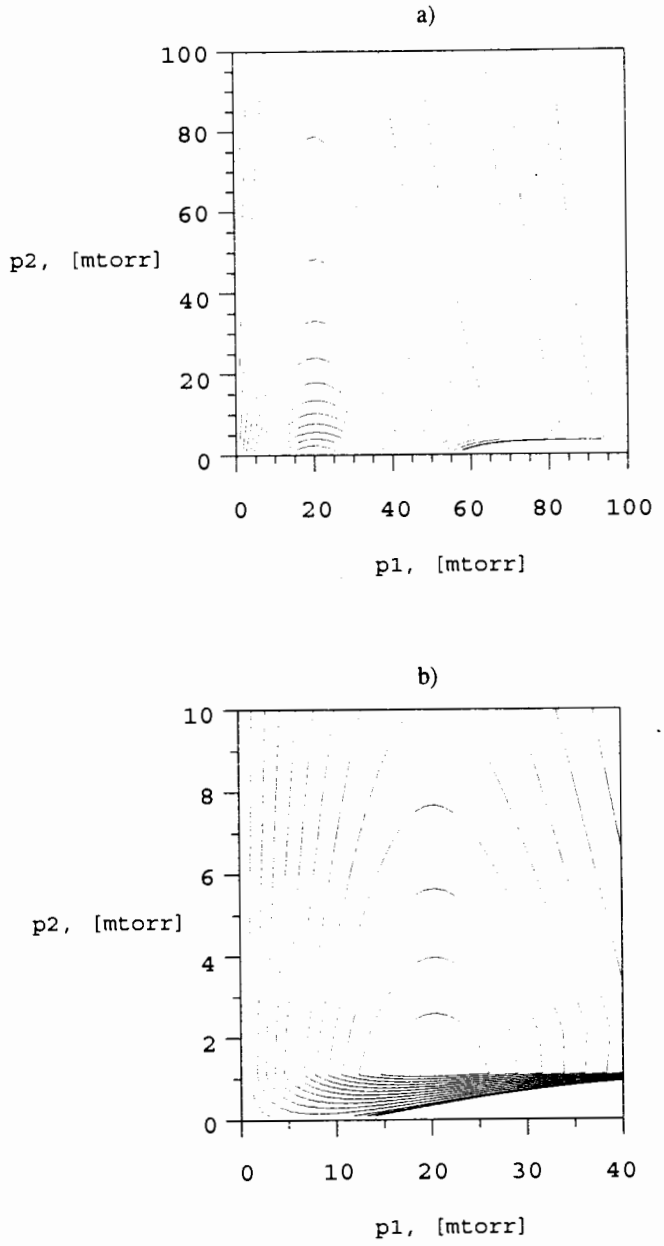

Figure 12. Contour plot of the Θ with V_{flowI}=3.3cm^3, V_{chII}=1000cm^3 and r_0=100μm. The maximum Θ in the second chamber, $\Theta_{max\ II}$, is 3.90 10^{-7} photons[NO_2]$^{-1}$s^{-1}.The contours in a) represent Θ for 3.63 10^{-7},3.32 10^{-7},3.02 10^{-7},2.70 10^{-7},2.40 10^{-7},....,3.0 10^{-8},1.5 10^{-8},3.0 10^{-9}, 1.5 10^{-9},3.0 10^{-10} photons[NO_2]$^{-1}$s^{-1}. b) is an enlargement of a). Contour represent Θ for 3.63 10^{-7},3.32 10^{-7},3.02 10^{-7},2.7 10^{-7},2.4 10^{-7},....,3.0 10^{-8},1.5 10^{-8} photons[NO_2]$^{-1}$s^{-1}.

The figures show that the maximum Θ shifts toward higher pressures p_1 in the first chamber and that its magnitude is also increasing with growing inflow. While the pressure shift is due to the increasing inflow, the rise of the magnitude of Θ can be explained by the higher absorption rates and the shorter residence times possible in the first chamber. Results would seem to encourage the use of a large nozzle diameter for high inflows into the cell.

The last parameter to evaluate is the flow volume in the first chamber. Similar to the considerations above, the volume of the second chamber and the radius of the inflow nozzle are held constant, while the flow volume of the first chamber is changed. Results are graphed in Figures 12, 13 and 14.

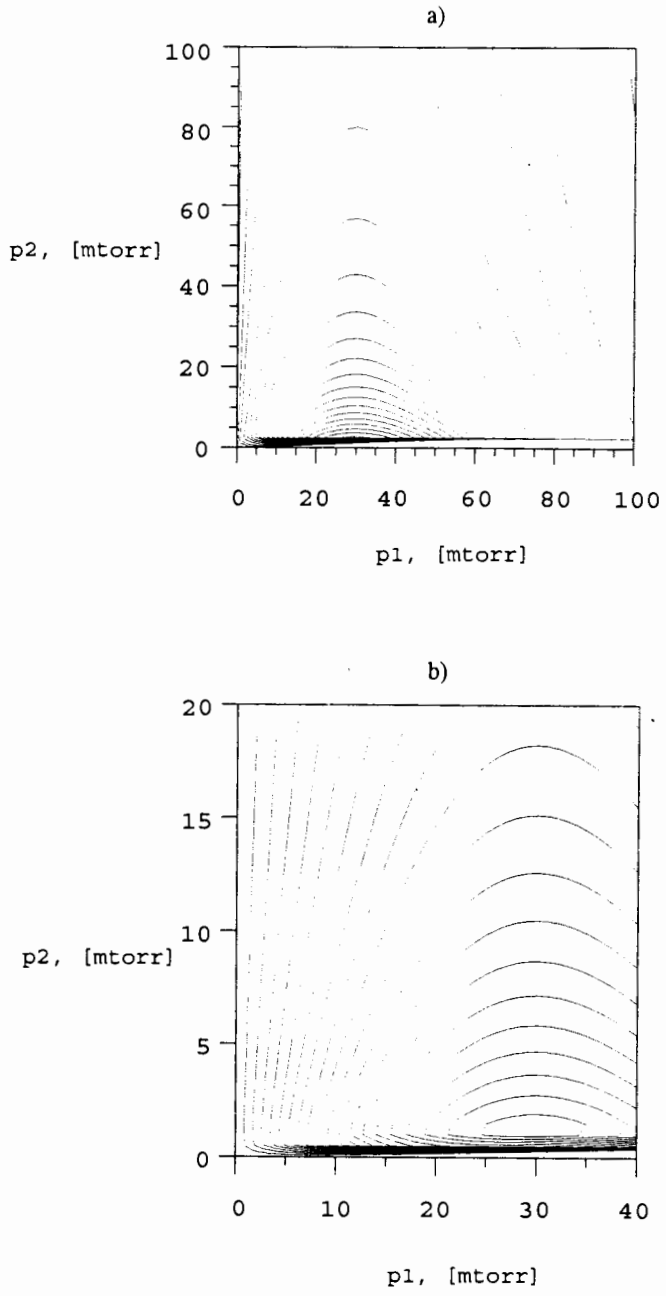

Figure 13. Contour plot of the Θ with V_{flowI}=1.7cm^3, V_{chII}=1000cm^3 and r_0=100μm. The maximum Θ in the second chamber, $\Theta_{max\,II}$, is 5.89 10^{-7} photons$[NO_2]^{-1}s^{-1}$. The contours in a) represent Θ for 5.7 10^{-7},5.4 10^{-7},.....,3.0 10^{-7},2.7 10^{-7},2.4 10^{-7},....,3.0 10^{-8},1.5 10^{-8},3.0 10^{-9} photons$[NO_2]^{-1}$ s^{-1}. b) is an enlargement of a). Contours in b) represent Θ for 5.7 10^{-7}, 5.4 10^{-7},....,3.0 10^{-7},2.7 10^{-7} ,2.4 10^{-7} ,....,3.0 10^{-8} photons$[NO_2]^{-1}s^{-1}$.

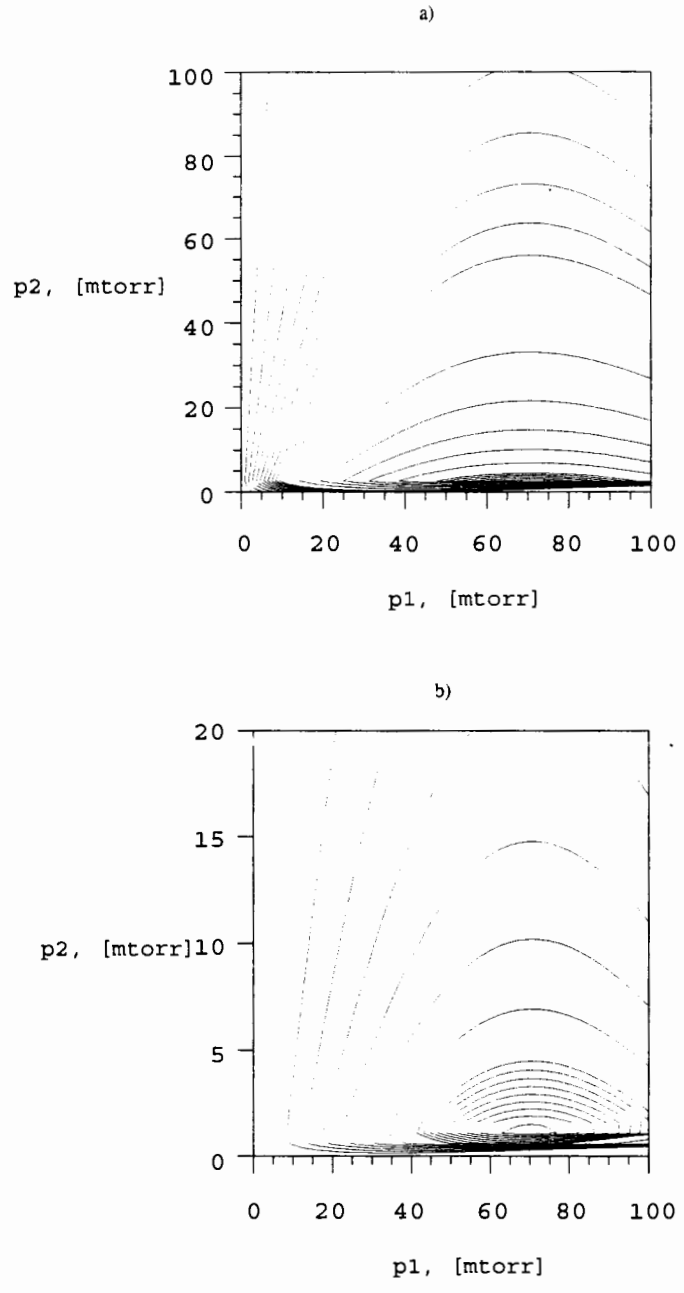

Figure 14. Contour plot of the Θ with V_{flowI}=1.0cm^3, V_{chII}=1000cm^3 and r_0=100μm. The maximum Θ in the second chamber, $\Theta_{max\ II}$, is 1.47 10^{-6} photons$[NO_2]^{-1}s^{-1}$. The contours in a represent Θ for 1.45 10^{-6},1.42 10^{-6},....,1.21 10^{-6},1.1 10^{-6},9.1 10^{-7},7.5 10^{-7},6.1 10^{-7},4.5 10^{-7}, 3.0 10^{-7}, 2.7 10^{-7},2.4 10^{-7}.....3.0 10^{-8} photons$[NO_2]^{-1}s^{-1}$. b) is an enlargement of a). Contours in b) represent Θ for 1.45 10^{-6},1.42 10^{-6},...,1.21 10^{-6},1.1 10^{-6},9.1 10^{-7},7.5 10^{-7}, 6.1 10^{-7},4.5 10^{-7},3.0 10^{-7} photons$[NO_2]^{-1}s^{-1}$.

The figures show that the maximum Θ shifts toward higher pressures of p_1. This leads to higher absorption rates and shorter residence times of the excited NO_2 molecules in the excitation chamber, but also to more quenching. The first two effects seem to overcome the reducing effect of quenching, which leads to an increasing magnitude of the maximum Θ with decreasing flow volume in the first chamber. The position of the maximum with respect to the pressure p_2 does not change.

All results suggest a cell design that is characterized by a small flow volume in the excitation chamber and large diameter of the inflow nozzle, as well as a sufficiently large detection chamber. A determining factor for the particular cell design is the capacity of the pump system and which pressure ranges can be achieved. A possible cell design is developed in Figure 15.

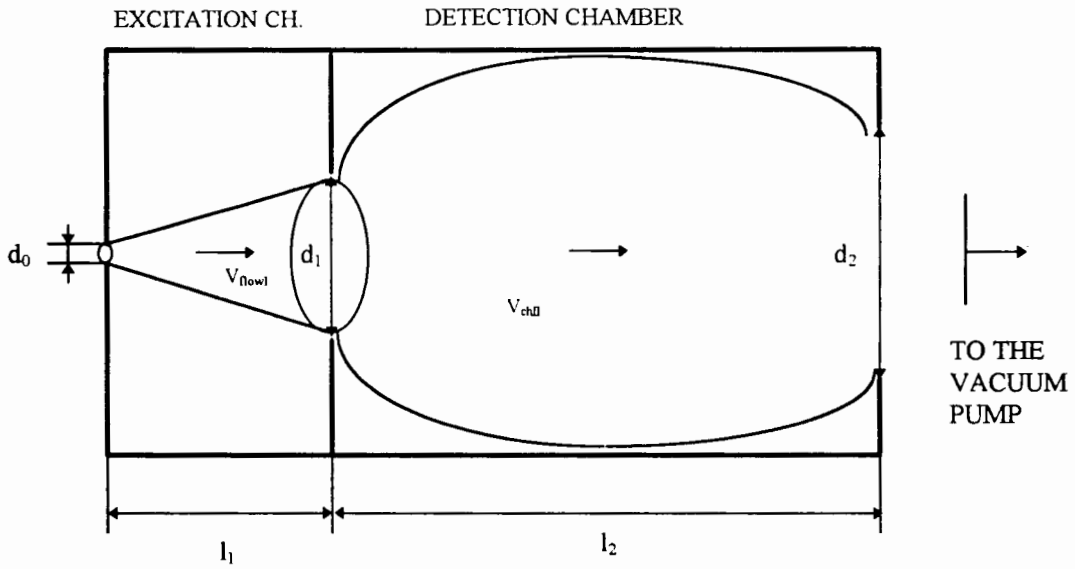

Figure 15. Abstraction of a possible design for the Two-Chamber-Detection-Cell.

The flow regime in the first chamber is characterized by plug flow, while the flow regime in the second chamber is assumed to be exponential dilution. How far these approximations hold is considered in the next section.

According to the results shown above, the parameters for the best performance could be chosen as r_0=100μm, V_{flowI}=1cm^3 and V_{chII}=1000cm^3. This gives a maximum Θ of 1.47 10^{-6}photons $[NO_2]^{-1}s^{-1}$ at p_1=70mtorr and p_2=1.2mtorr. At this particular pressure ratio for p_1/p_2 of about 0.017, the orifice between the two chambers would be choked. Choking of the orifice between both chambers of the cell would result in formation of a shock wave system in the detection chamber. Undergoing collisions between the excited molecules while passing these shock waves yield a nonradiative deactivation of these molecules. This results in a decrease of the fluorescence signal detected. To avoid the choking of the orifice, the pressure ratio of p_2/p_1 should be kept larger than 0.1.

Considering this, the pressure combination of p_1=70mtorr and p_2=8mtorr seems to be reasonable and gives a resulting fluorescence signal Θ of 1.00 10^{-6} photons $[NO_2]^{-1}$ s^{-1}. Let's assume a pumping system which could supply enough capacity to provide these pressures. What would the flow in both chambers look like?

FLOW REGIME IN A HYPOTHETICAL CELL

When a gas is exhausted through a nozzle to a pressure much below nozzle exit pressure, the free jet expands to the lower pressure very quickly, increasing the cross-sectional area of the jet and creating a "normal" shock and the typical "shock bottle" configuration of a highly underexpanded jet. A schematic of the highly

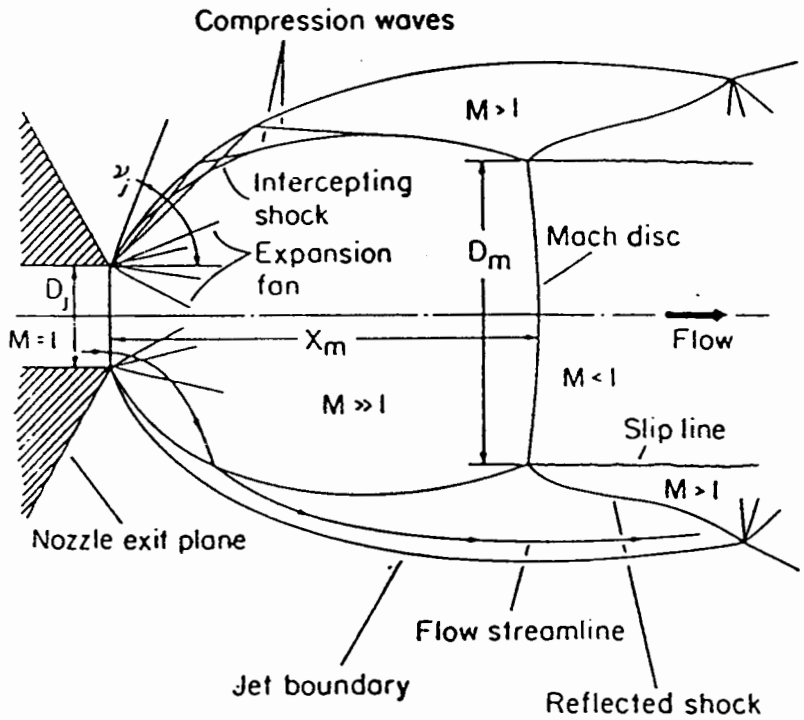

Figure 16. Schematic of underexpanded jet [Christ *et al.*, 1965]

An expansion fan forms at the nozzle lip as the flow expands into the low-pressure ambient gas. The expansion waves extend to the free pressure jet boundary and reflect as weak compression waves. These compression waves coalesce to form

the intercepting shock in the interior of the jet. The intercepting shock is an oblique shock behind which the flow is still supersonic but at a lower Mach number than the flow in the core of the jet. The Mach disk is a slightly curved shock that is normal to the flow at the jet axis. The flow downstream of the Mach disk is clearly subsonic whereas the flow behind the shock that reflects from the interaction of the intercepting shock and Mach disk is still supersonic [Christ *et al.*, 1965]. The jet is axisymmetric.

The jet flow downstream of the Mach disk is similar to incompressible flow since changes in density are very small. It has been shown [Ashkenas *et al.*, 1968] that the jet can be thought of as an expanding cone originating from a point on the axis in or close to the nozzle exit plane. Certain experimental results are also in accord with the idea that the observed Mach-disk diameters fall accurately within the expanding cone [Davidor *et al.*, 1971].

In order to model the flow regime in the Two-Chamber-Detection-Cell, a computer program (Quick and Simple) by G.Recktenwald and S.Forbes was employed. To overcome the limitation of the program which is that it only handles incompressible flows or compressible ones with a density change of less than 5% of the initial density, certain approximations have to be made. As mentioned before, the jet flow can be treated similar to incompressible flow behind the Mach disk. The idea, therefore, is to calculate characteristic properties like absolute temperature, static pressure or velocity for a location immediately behind the Mach disk, and use them as input for the model calculations. The length of the first chamber is then given by the

original length minus the location of the Mach disk. The Mach disk diameter provides the diameter of the inflow.

The axial distance from the nozzle exit to the Mach disk is

$$\frac{x_M}{D} = 0.67\left(\frac{p_0}{p_1}\right)^{\frac{1}{2}} \tag{30}$$

covering a wide range of pressure ratios and a variety of monatomic, diatomic, and triatomic gases, where p_0 is the ambient pressure outside the cell, p_1 the ambient pressure in the first chamber of the cell, and D the diameter of the used inflow nozzle [Christ *et al.*, 1965].

In order to obtain the Mach disk diameter, the following equation can be used [Addy *et al.*, 1981]

$$\frac{D_M}{D} = 0.36\left(\frac{p_0}{p_1} - 3.9\right)^{\frac{1}{2}}. \tag{31}$$

A calculation of the flow properties behind the Mach disk requires the knowledge of the Mach number of the flow in front of the Mach disk. This can be done by using the formula suggested by [Ashkenas *et al.*, 1968], for purely radial source flow

$$M = A\left(\frac{x - x_0}{D}\right)^{\gamma-1} - \frac{1}{2}\left(\frac{\gamma+1}{\gamma-1}\right) \Big/ A\left(\frac{x - x_0}{D}\right)^{\gamma-1} \tag{32}$$

The constants A and x_0 depend upon γ and are given for γ=1.4 by A=3.65 and x_0=0.4. Figure 17 shows the predicted Mach number distribution along the centerline.

The increase in Mach number in the expansion is the result of the conversion of thermal energy into directed kinetic energy. This process requires collisions among the molecules. With increased distance the stream density and the temperature are reduced, as well as the collision frequency. Absolute temperature, velocity, static pressure and density can be calculated by using the appropriate formulas for varying-area adiabatic flow and the according adiabatic relations, which are given in Equations 33 to 35 [Zucker, 1977].

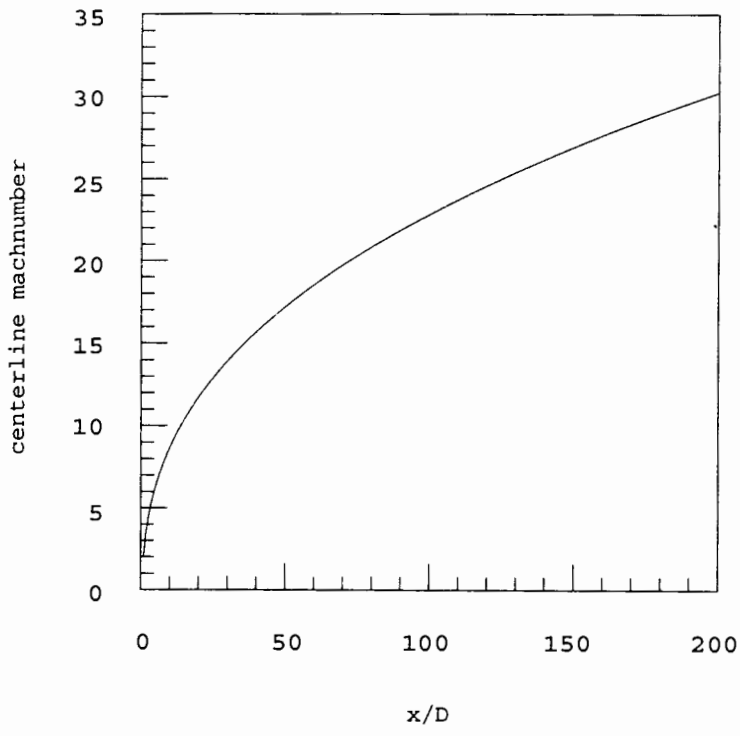

Figure 17. Mach number distribution along the centerline of the jet.

$$\frac{T_2}{T_1} = \frac{1 + \frac{(\gamma - 1)}{2} M_1^2}{1 + \frac{(\gamma - 1)}{2} M_2^2} \tag{33}$$

$$\frac{p_1}{p_2} = \left(\frac{T_2}{T_1} \right)^{\frac{\gamma}{1-\gamma}} \tag{34}$$

$$v = M \sqrt{R^* g \gamma T} \tag{35}$$

T_1, p_1 and M_1 are the initial absolute temperature, static pressure and Mach number at the centerline of the jet, respectively, and T_2, p_2 and M_2 the final conditions. R^* represents the gas constant for air and γ the adiabatical exponent for air. g is the acceleration constant. Using Equations 32 and 33, and substituting them into 35 leads to an expression for the absolute centerline velocity in terms of the ratio of distance over diameter of the inflow orifice, x/D. The result is graphed in Figure 18.

For any given fluid with a specific set of conditions entering a normal shock, there is only one set of conditions that can result after the shock. Conditions after the shock can be calculated by using Equations 36 to 39 [Zucker, 1977].

$$\frac{T_2}{T_1} = \frac{\left(1 + \frac{(\gamma - 1)}{2} M_1^2 \right) \left(\frac{2\gamma}{\gamma - 1} M_1^2 - 1 \right)}{\frac{(\gamma + 1)^2}{2(\gamma - 1)} M_1^2} \tag{36}$$

$$\frac{p_1}{p_2} = \frac{2\gamma}{\gamma + 1} M_1^2 - \frac{\gamma - 1}{\gamma + 1} \tag{37}$$

$$\frac{\rho_2}{\rho_1} = \frac{(\gamma + 1)}{(\gamma - 1)} \frac{M_1^2}{M_1^2 + 2} \tag{38}$$

$$v_2 = v_1 - \frac{2\sqrt{\gamma R^* T_1 g}}{\gamma + 1}\left(\frac{M_1^2 - 1}{M_1}\right) \tag{39}$$

T_1, p_1, ρ_1, v_1 and M_1 represent the temperature, static pressure, density, absolute velocity and Mach number at the centerline in front of the Mach disk, respectively, and T_2, p_2, ρ_2, v_2 and M_2 behind the Mach disk.

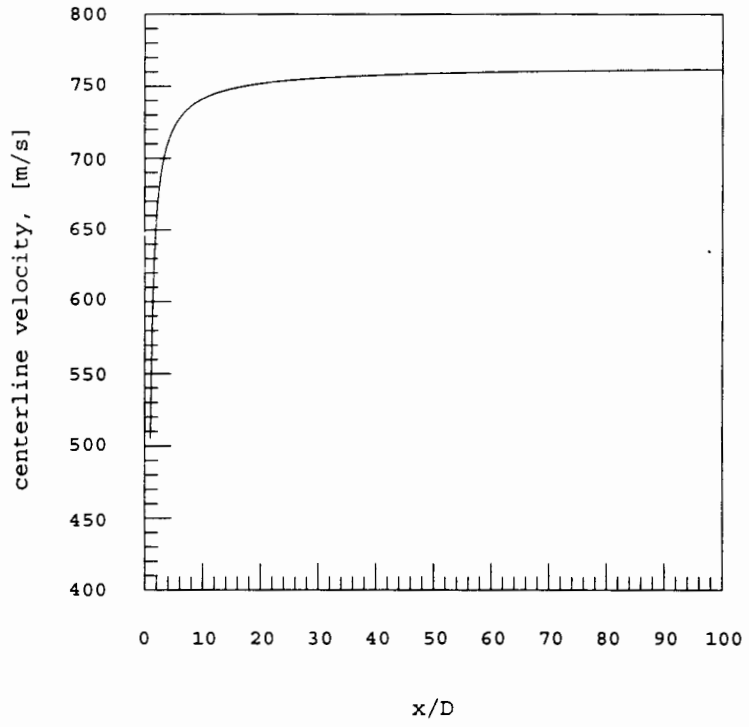

Figure 18. Centerline velocity before passing the Mach disk..

In order to model the flow regime in the Two-Chamber-Fluorescence-Cell, the dimensions of the cell have to be determined. This can be done by using the results of the former section. It has been assumed that there is a plug flow regime in the first chamber of the cell. This has been based on the fact that the jet expansion in the first chamber leads to an expanding cone, which characterizes the flow regime in this chamber. The Mach disk lies within the expanding cone. Since the volume of the expanding cone is known from the previous section, the distance between the Mach disk and the orifice between both chambers of the cell, as well as the radius of the same orifice can be calculated. Therefore, the radius of the orifice equals the radius of the expanding jet when passing into the second chamber. The distance from the inflow nozzle to the orifice between both chambers can be calculated by adding up the distances from inflow nozzle to the Mach disk and from Mach disk to the orifice. Since only the volume of the flow in the first chamber is fixed, the chamber volume itself can be chosen arbitrarily. The volume of the second chamber was set in the previous section. The dimensions of the second chamber were chosen with respect to an available experimental cell set-up. All calculations are based on an axisymmetric cell design.

The only parameter which is not fixed yet is the radius of the outflow orifice of the cell, r_2. This radius is going to be varied during the modeling and its influence on the flow regime of the second chamber of the cell is being evaluated. The results of that should give a better perspective about how far the desired flow regime of exponential dilution can be assumed in the second chamber. Figure 19 gives the

dimensions of the cell used and Table 3 shows predicted properties for a location in the jet directly behind the Mach disk that are used as input for the program to model the flow properties.

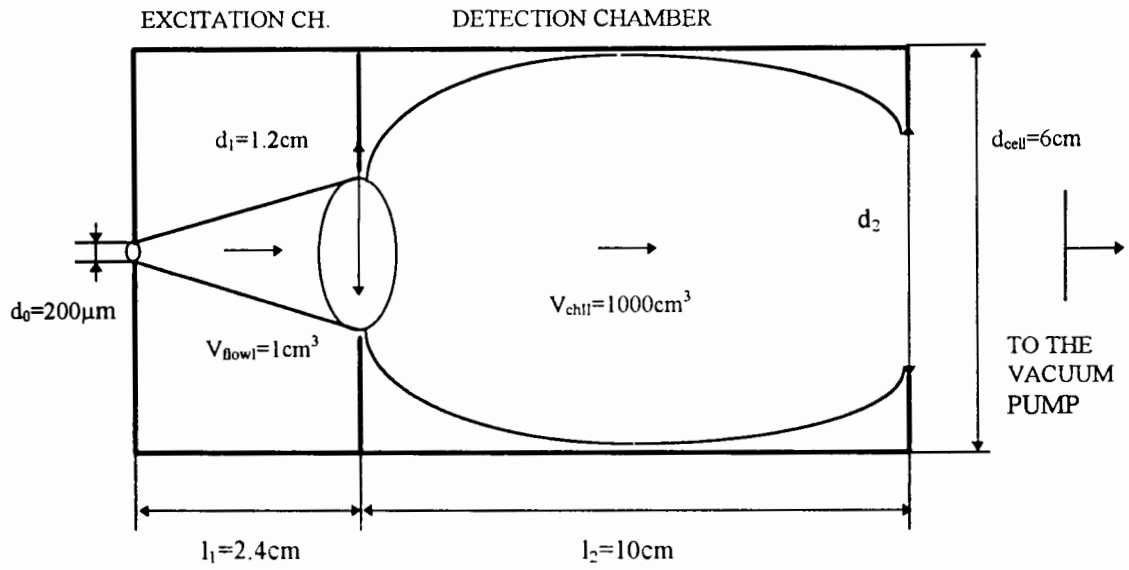

Figure 19. Possible design for the Two-Chamber-Fluorescence-Cell.

Table 3. Predicted flow characteristics for inflow nozzle diameter r_0=100μm, V_{flowI}=1cm^3 and V_{chII}=1000cm^3. Stagnation temperature T_t=290K and stagnation pressure p_t=760torr.

chamber pressures p_1 and p_2, [mtorr]	location and diameter of the Mach disk, [cm]	flow properties of the jet shortly behind the Mach disk
p_1=70 p_2=8	x_M=1.40 d_M=0.75	T=283K p=78mtorr v=128ms^{-1} ρ=1.292 10^{-4}kgm^{-3} μ=1.649 10^{-5}kgm^{-1}s^{-1} D=0.128m^{2}s^{-1}

As one can see in the calculations, the pressure of the second chamber, p_2, is neglected in the modeling of the flow regime in the cell. The following arguments

justify this approach. As long as the pressure difference between the first and second chambers is maintained so that the orifice between both chambers is not choked, molecules passing into the second chamber accelerate due to this pressure difference but still remain at subsonic velocity. A choking of the orifice would yield supersonic velocities of the molecules passing the orifice and would also result in formation of a shock wave system in the flow. Since the molecules in the flow remain at subsonic velocities, the approach of treating air as incompressible fluid is still valid. Therefore model results are expected to remain valid as well, with respect to the general behavior of the flow in the cell. Magnitudes of the velocities in the second cell may differ from their actual value.

Another approximation made is that p_2 is always kept to be 8mtorr regardless of the chosen radius of the outflow of the cell, r_2. This is only valid if the outflow orifice is not choked as well, in which case even an increasing pumping speed would not yield any pressure changes in the second chamber. Such conditions are practically impossible to guarantee if r_2 less than a few millimeters. Consequently, such values are excluded from the modeling.

The Reynolds number referring to the diameter of the Mach disk and the inflow properties directly behind the Mach disk was calculated to be 8.023 for all cases. The stagnation pressure in the reservoir is about 760torr and the stagnation temperature around 290K. This results in an absolute temperature at the nozzle exit of 244K and the static pressure of 401torr at the same location. Since a converging nozzle was used, the Mach number at the nozzle exit does not exceed the value of

one and the velocity for this special case is 313m/s. Under the assumption that the pressure in the first chamber is kept constant for all considered cases, the residence time of excited NO_2 molecules in the first chamber is 13.6μs.

Due to the rapid expansion it can be assumed that by the time the jet flow passes the Mach disk, no velocity profile has been fully developed yet. Therefore, a flat velocity profile has been chosen as a profile of the inflow into the first chamber. Figures 20, 21, 22 and 23 show the obtained velocity distributions of the axial velocity of the flow for the conditions mentioned above. "Slicing" of the surface plot along a certain location of the cell width would give the velocity profile at this point, as indicated by the two-dimensional plot.

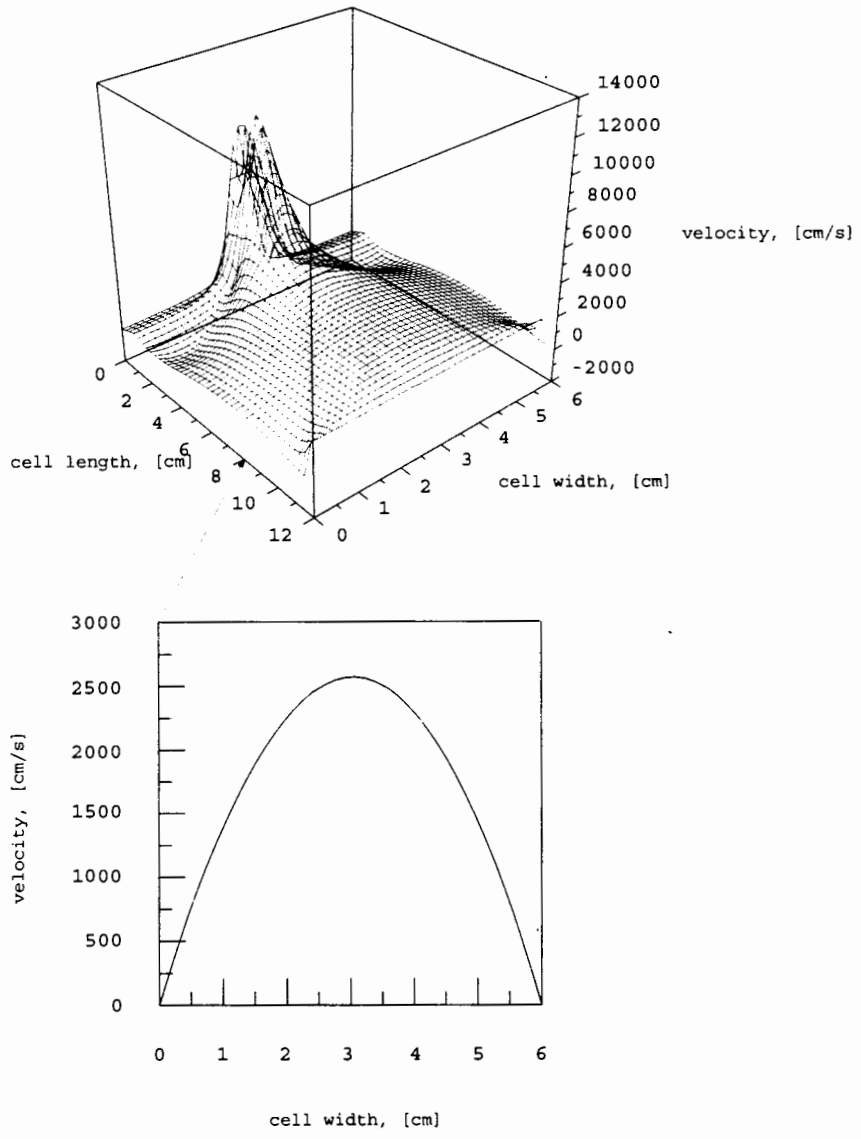

Figure 20. Velocity distribution for nozzle diameter of d_0=200μm, a diameter of the orifice between both chambers of the cell $d_{orifice}$=1.2cm and a diameter of the outflow opening d_2=6cm Re with respect to the Mach disk diameter and the flow properties behind the Mach disk was 8.023. QUICK was the numerical algorithm used with a grid size of 40x41.

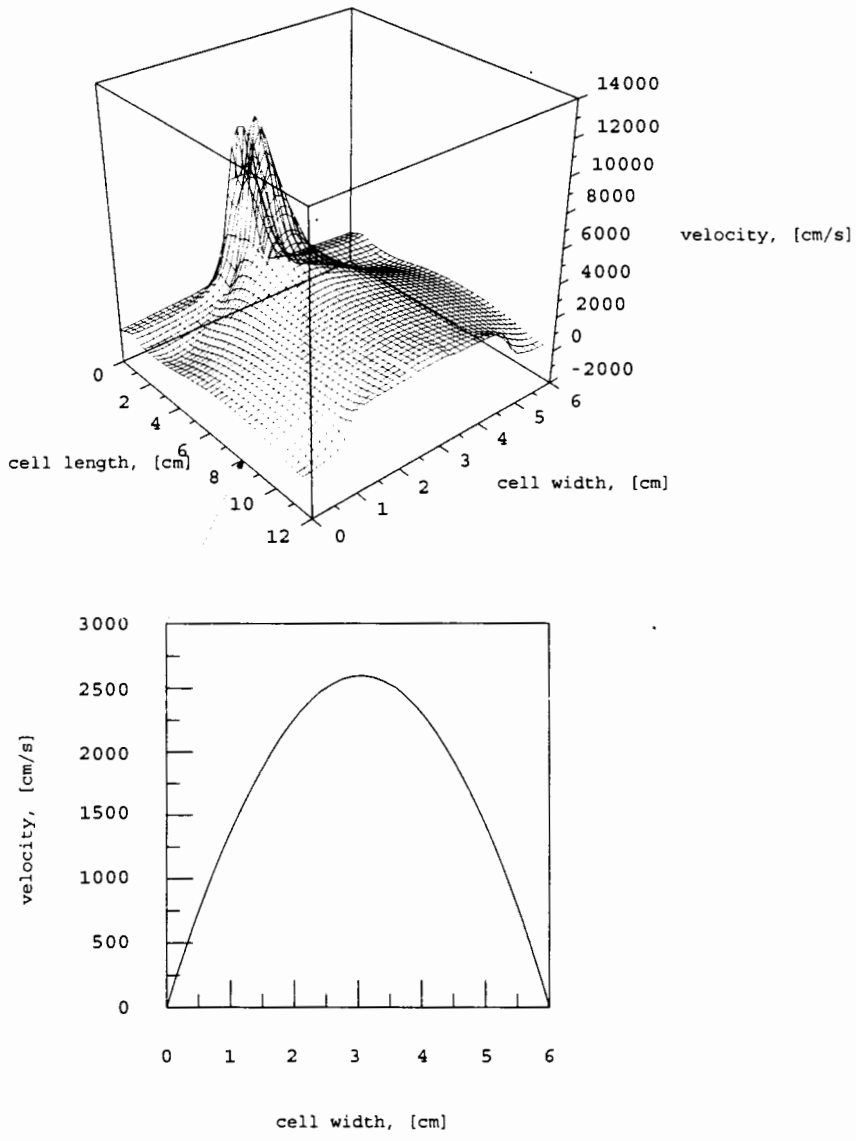

Figure 21. Velocity distribution for nozzle diameter of d_0=200μm, a diameter of the orifice between both chambers of the cell $d_{orifice}$=1.2cm and a diameter of the outflow opening d_2=4cm. Re with respect to the Mach disk diameter and the flow properties behind the Mach disk was 8.023. QUICK was the numerical algorithm used with a grid size of 40x41.

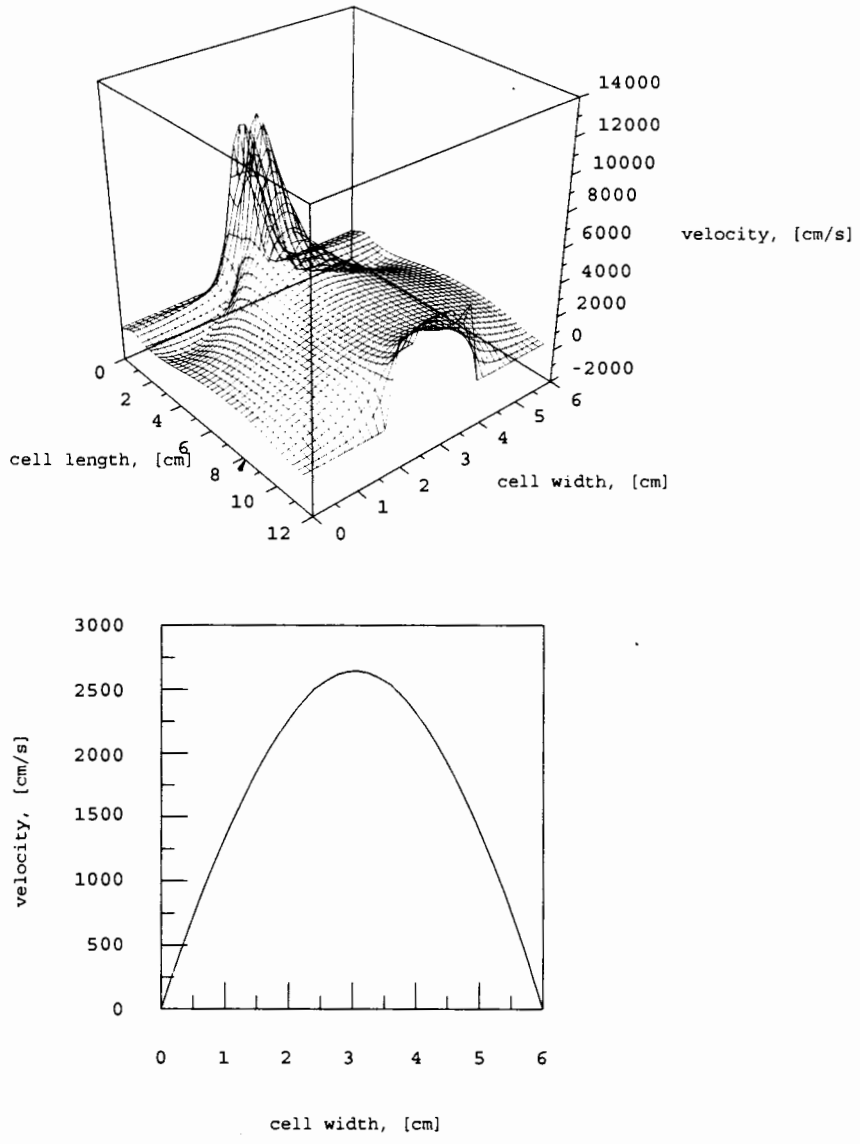

Figure 22. Velocity distribution for nozzle diameter of d_0=200μm. a diameter of the orifice between both chambers of the cell $d_{orifice}$=1.2cm and a diameter of the outflow opening d_2=2cm. Re with respect to the Mach disk diameter and the flow properties behind the Mach disk was 8.023. QUICK was the numerical algorithm used with a grid size of 40x41.

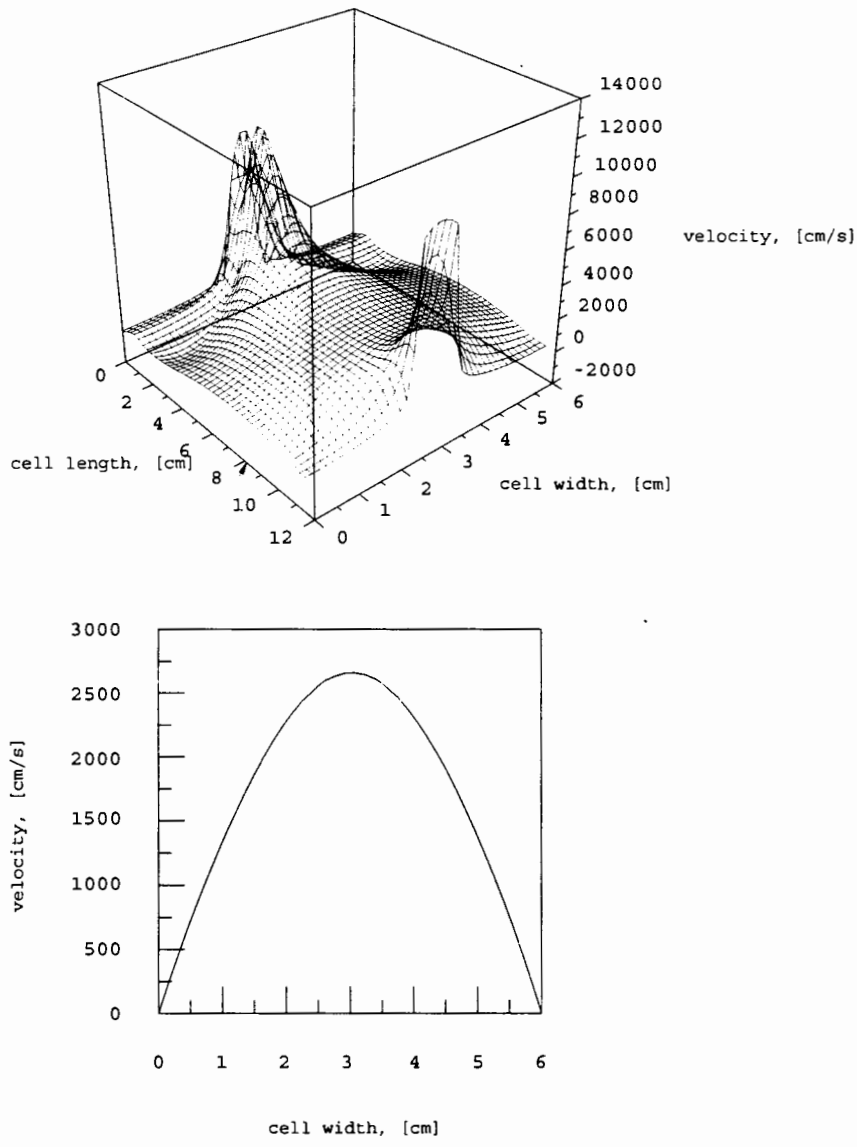

Figure 23. Velocity distribution for nozzle diameter of d_0=200μm, a diameter of the orifice between both chambers of the cell $d_{orifice}$=1.2cm and a diameter of the outflow opening d_2=1cm. Re with respect to the Mach disk diameter and the flow properties behind the Mach disk was 8.023. QUICK was the numerical algorithm used with a grid size of 40x41.

The graphs show that although the radius of the outflow is varied, the flow in the first chamber does not vary significantly. Incoming molecules slow down in the course of the jet expansion and accelerate again while passing the orifice between both chambers of the cell. Some minor eddies occur in the first chamber. However, the major part of the incoming molecules stays localized within the expanding cone of the jet and passes over into the detection chamber. There the flow expands further and reattaches to the wall of the chamber after a short distance. Velocities are dropping rapidly and then stay nearly constant. In like manner with the first chamber, eddies occur in the beginning of the second chamber. After reattachment, the velocity distribution on every point along the length of the second chamber seems to be parabola-like. Due to the outflow orifice, the flow velocities are increasing again. Different radii of the outflow orifice result in different outflow velocities. The flow regime in the second chamber can be characterized as an intermediate case between plug flow and exponential dilution. Due to the expanding flow in the second chamber with its parabola-like profile, incoming molecules would travel with different velocities at different points in the cell and therefore would stay in the second chamber with different long residence times depending on their position in the flow.

A compromise has to be made concerning the choice of the radius of the outflow orifice. This compromise is determined by the desire to minimize the radius in order to provide a closed detection chamber, and therefore reduce the background by blocking light coming from light leaks in the connection to the pump. On the other hand, the orifice has to be large enough, so that the pressure requirements can be met

to avoid choking the orifice. The shape of the flow modeled with the program indicates that a major fraction of the molecules coming into the excitation chamber through the nozzle would get into the second chamber before being quenched away. There they stay long enough so that all of their fluorescence decay can be detected by the detection device used before they leave the cell in the direction of the pump.

The volume of the first chamber does not seem to have major influences on the flow regime in the same chamber. This might be advantageous if one considers the fact that a large volume for the excitation chamber would reduce the amount of scattered photons which get reflected into the detection chamber and contribute there to the background signal. This is also in accord with the results of the preceding section which show that as long as the flow volume remains the same, different volumes of the excitation chamber would not influence the possible performance of the cell.

LIMITATIONS AND RELIABILITY OF THE MODEL RESULTS

A very important question to ask is how reliable these modeled results are and for which gas flows they are valid. The Knudsen number is a very important parameter to characterize flow regimes. It is dimensionless and defined as the ratio of the mean free path, λ, to a characteristic dimension of the flow system, d.

$$Kn = \frac{\lambda}{d} \tag{40}$$

There are two extreme flow cases. The first, viscous flow, occurs at Knudsen numbers lower than 0.01, when the mean free path is much smaller than the characteristic dimension of the flow system. Therefore the character of the gas flow is determined by gas-gas collisions. The flow has a maximum velocity in the center of the channel and zero velocity at the wall. When the mean free path is equal or greater than the characteristic dimension of the flow system, the flow properties are determined by gas-wall collisions and the effect of intermolecular collisions can be neglected. For most surfaces diffuse reflection at the wall is a good approximation. Each particle arrives at the surface, sticks, and is reemitted in a direction independent of its incident velocity. Therefore a particle entering the flow system has a chance of not being transmitted, but can return to the entrance. This flow region is referred to as free molecular flow and is characterized by Knudsen numbers of greater than one. In the region $1<Kn<0.01$ the flow is neither continuous nor molecular. This region is called the transition flow range. In this range, the velocity at the wall is not zero as in continuum flow and the reflection is not diffuse as in free molecular flow.

Concerning the modeling results, they are certainly reliable for the continuum flow region, and parts of the transition flow region as well. Since the flow in the transition region is not well understood, the generalization of this statement for the whole transition region is not possible. As soon as the transition to the molecular flow region occurred, the existence of the shock wave system that is due to collisions between the gas molecules vanishes. After the molecules leave the nozzle exit, they continue on their way without being affected by collisions with other molecules. The

resulting expansion cone is determined by the diameter of the nozzle between both chambers of the cell. This orifice would act similar to a skimmer. Reflected molecules off the surface of the skimmer would reentrain into the expanding jet within the first chamber. Subsequently, this would lead to a perturbation of the jet expansion by collisions between the reentrained molecules and the molecules within the expanding jet. However, this can be avoided by using the technique of differential pumping in the first chamber. Expanding jets in the molecular flow region do not suffer from huge quenching losses due to negligible collisions between molecules and the existence of no shock wave system. This can be useful unless the pressure to achieve this flow regime within the first chamber is below the half-quenching pressure.

DIFFUSION AND QUENCHING

Another question to consider is the effect of quenching and diffusion of the excited NO_2 molecules in the detection chamber of the cell. To clarify these relations, a simple one-dimensional model can be proposed.

A laser beam with the beam radius of r passes through a flow of air perpendicularly and excites NO_2 molecules which are located in the area that is limited by the laser beam. Figure 24 shows this for a laser beam with a radius r. The excited NO_2 molecules are assumed to be uniformly distributed over the whole excitation zone. This results in concentration gradient of excited NO_2 in x and forces diffusion of these excited NO_2 molecules along the x axis. There is no diffusion in the

direction of the y-axis. How far the assumptions made remain valid is discussed at the end of this section.

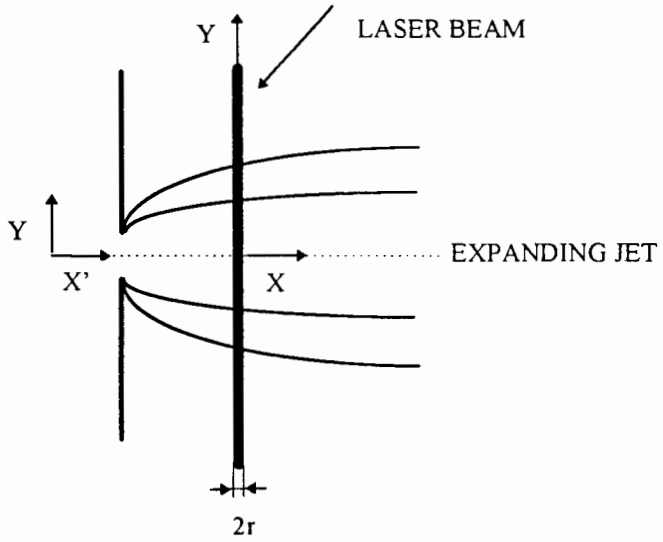

Figure 24. Schematic of the laser beam with radius r passing through an expanding jet perpendicularly.

Excited molecules at an arbitrarily chosen line of length 2r along x and width dy are called the instantaneous plane source of those molecules referring to their assumed, uniform distribution along the same axis. As soon as excitation of the NO_2 molecules occurs, the competing processes of fluorescence and quenching start, as well as diffusion of those molecules out of the initial excitation zone. This section shall clarify the relation between quenching and diffusion, and shall answer the question if it is reasonable to believe that diffusion processes do not significantly influence the performance of the proposed cell.

As shown in Equation 3, the rate of disappearance of excited NO_2 molecules can be described by

$$\frac{d\left[NO_2^*\right]}{dt} = -\left[NO_2^*\right]\left(k_q\left[M\right] + k_f\right) \tag{41}$$

which leads to an expression for the concentration of excited NO_2 molecules with respect to time.

$$\int_{\left[NO_2^*\right]_0}^{\left[NO_2^*\right]} \frac{d\left[NO_2^*\right]}{\left[NO_2^*\right]} = -\int_0^t \left(k_q\left[M\right] + k_f\right)dt \tag{42}$$

$$\left[NO_2^*\right] = \left[NO_2^*\right]_0 \exp\left[-\left(k_q\left[M\right] + k_f\right)t\right] \tag{43}$$

Time dependent diffusion processes are characterized by

$$\frac{\partial C}{\partial t} = D\frac{\partial^2 C}{\partial x^2} \tag{44}$$

where D is the diffusion coefficient and C the concentration of the substance to be considered. A solution of this partial differential equation for an instantaneous line source is

$$C(x,t) = \frac{\alpha}{\sqrt{t}}\exp\left[-\frac{x^2}{4Dt}\right]. \tag{45}$$

α is an arbitrary constant which has to be chosen with special reference to the case considered.

For an instantaneous plane source which has the initial concentration C_0 within the plane of one unit of area at a location -r<x<r, and no concentration at locations with |x|>r, the concentration at any point x at any time can be expressed by

$$C_P(x,t) = \frac{\alpha}{\sqrt{t}}\int_{x-h}^{x+h}\exp\left[-\frac{x^2}{4Dt}\right]dx. \tag{46}$$

The total amount of substance S present in an instantaneous plane source can be described by

$$S = A\int_{-\infty}^{\infty} C dx \,. \tag{47}$$

Since A is the area of the instantaneous plane source and its cross section is set to be of one unit of area, and C the concentration of the present substance at one line in the plane source, Equations 45 and 47 can be combined to give Equation 48

$$S = \frac{\alpha}{\sqrt{t}}\int_{-\infty}^{\infty} \exp\left[-\frac{x^2}{4Dt}\right] dx \,. \tag{48}$$

This equation can be solved by substitution of $\frac{x}{2\sqrt{Dt}}$ with ξ which leads to

$$S = 2\alpha\sqrt{D}\int_{-\infty}^{\infty} \exp\left[-\xi^2\right] d\xi \tag{49}$$

This gives an expression for α in the case of an instantaneous plane source of a substance S.

$$\alpha = \frac{S}{2\sqrt{D\pi}} \tag{50}$$

With this, Equation 46 becomes

$$C_P(x,t) = \frac{S}{2\sqrt{D\pi t}}\int_{x-r}^{x+r} \exp\left[-\frac{x^2}{4Dt}\right] dx \,. \tag{51}$$

According to the special case of excited NO_2 molecules, the total amount of substance in the plane source can be determined at any time by Equation 43. Applying this to Equation 51 results in Equation 52.

$$\left[NO_2^*\right](x,t) = \frac{\left[NO_2^*\right]_0}{2\sqrt{D\pi t}} \exp\left[-\left(k_q[M] + k_f\right)t\right] \int_{x-r}^{x+r} \exp\left[-\frac{x^2}{4Dt}\right] dx \qquad (52)$$

which can be rewritten as

$$\left[NO_2^*\right](x,t) = \frac{\left[NO_2^*\right]_0}{2} \exp\left[-(k_q[M] + k_f)t\right] \left(erf\left[\frac{r+x}{2\sqrt{Dt}}\right] + erf\left[\frac{r-x}{2\sqrt{Dt}}\right] \right) \qquad (53)$$

The assumptions of uniform pressure in the whole cell and constant velocity along the y-axis make it possible to apply the results to the proposed cell. As long as the velocity distribution along the y-axis stays constant, Equation 53 is valid for any point along the axis x'. According to the results obtained by modeling the flow regime in the proposed cell, this would be virtually true for molecules located in the core of the flow or in its closer vicinity. Therefore this assumption is certainly met by the flow in the first chamber with its nearly flat velocity profile in the core of the flow. For the broader, parabola like velocity profile in the second chamber, this equation can still be seen as rough approximation of the occurring processes.

Assuming the validity of these approximations, graphs of Figure 25 show the relative concentration distribution of excited NO_2 molecules along the x-axis at different times and therefore at different locations x' within the first chamber of the cell. Here quenching and diffusion occur simultaneously. Graphs in Figure 26 describe the same process but without quenching. The radius of the laser beam was chosen to be 0.5cm.

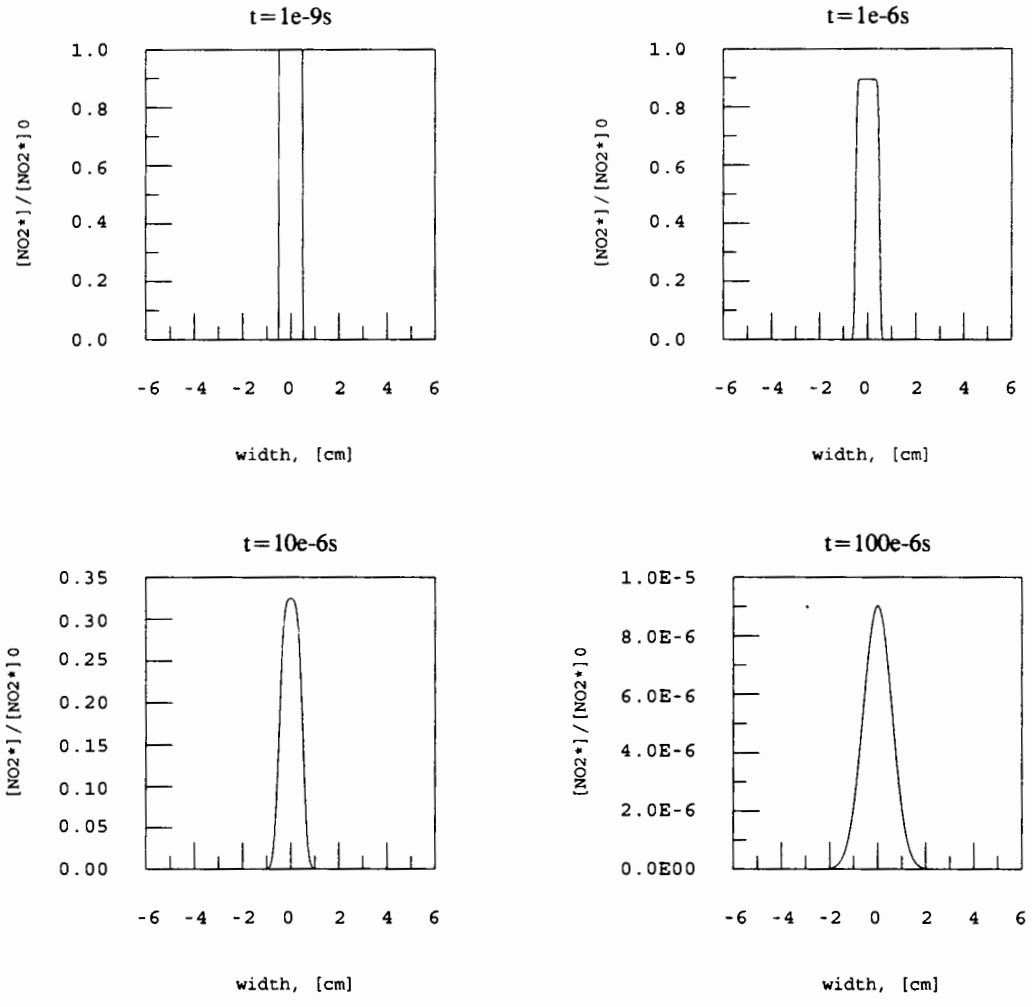

Figure 25. Relative concentration distribution of excited NO_2 molecules referring the conditions in the excitation chamber. Diffusion and quenching processes happen simultaneously.

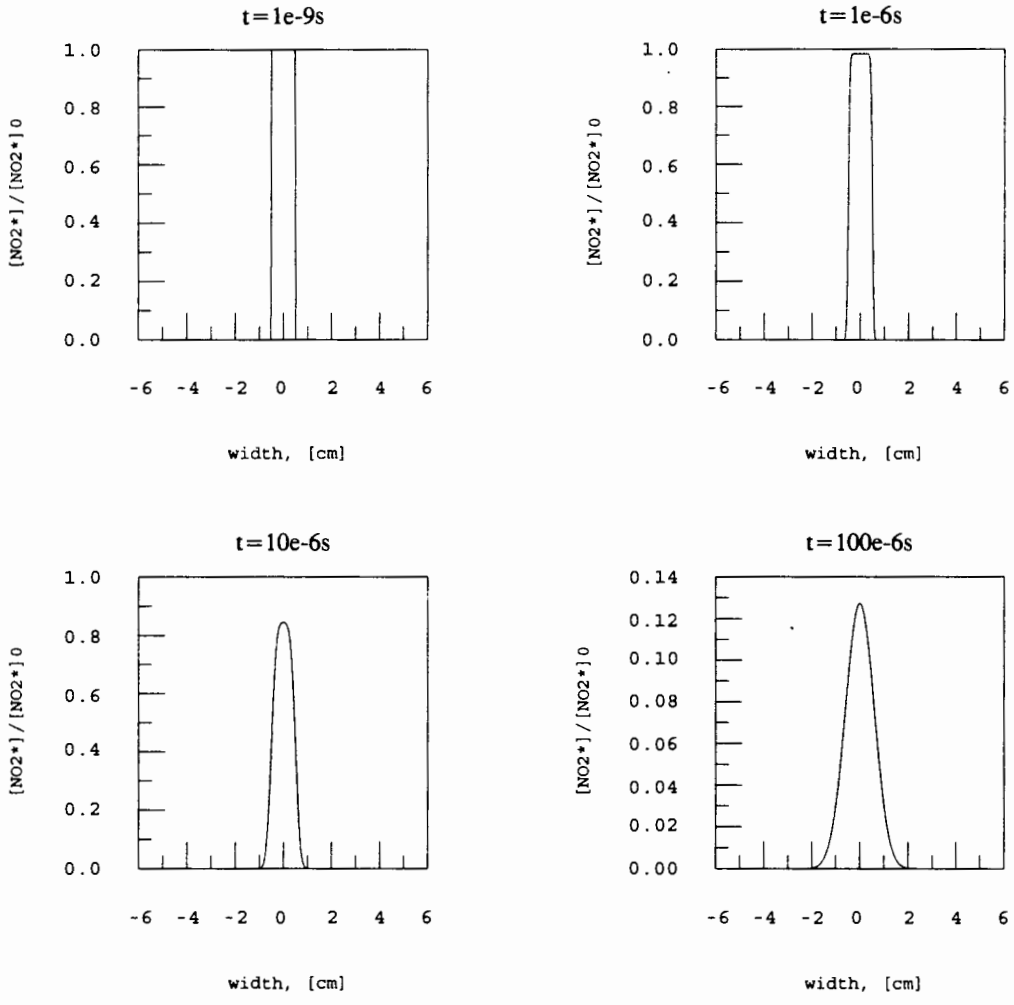

Figure 26. Relative concentration distribution of excited NO_2 molecules referring the conditions in the excitation chamber. Quenching processes are neglected.

Comparing the graphs for the case of simultaneous quenching and diffusion with the graphs for occurring diffusion without quenching shows that both processes occur uncoupled from each other. Graphs at the same times have the same shape of the distribution curve in common, but differ in magnitude of the relative concentration. Graphs also indicate that diffusion along the x-axis does not seem to prevent the excited NO_2 molecules from reaching the detection chamber, since even after 100μs the excited NO_2 molecules remain in the vicinity of the initial excitation zone. The residence time of the excited NO_2 molecules in the first chamber of the proposed cell set up is 14μs.

Diffusion in direction of the y-axis has not been considered due to the assumption of uniformly distributed excited NO_2 molecules along the y-axis throughout the laser beam passing the cell. This assumption is virtually true only for locations along the y-axis which are within the core of the flow or in its closer vicinity, due to the velocity profile there. Consequently, this results in a concentration gradient also in y direction. Since NO_2 molecules located outside the expanding cone are excited by the crossing laser beam as well, this concentration gradient seems to be rather small compared to the concentration gradient in x direction, and therefore can be neglected.

Comparing diffusion and quenching it must be said that quenching is the more dominant process of losing excited NO_2 for detection of their fluorescence. Diffusion seems to be negligible. As soon as the excited molecules pass into the detection

chamber, the lower pressure and therefore a different diffusion coefficient changes the succeeding concentration distributions. However, this does not change the general relationships between quenching and diffusion.

CHAPTER III

INTRODUCTION OF A TWO-CHAMBER-NO_2-FLUORESCENCE-CELL

In order to verify the theoretical predictions of the performance of a Two-Chamber-NO_2-Fluorescence-Cell, a detection cell was provided and experiments were done. The given detection cell was not built according the conclusions drawn from the theoretical considerations and does not exhibit the optimum performance possible by such a cell type. Also, the completed experiments do not serve the purpose of showing the detection limit of this new measurement technique for NO_2. The major focus of the experiments was to clarify the origin of the observed signals and to draw conclusions for the practical design of such a Two-Chamber-Fluorescence-Cell.

The following paragraphs shall show that it is possible to detect NO_2 directly by a two-chambered measuring technique and finally provide insight into what can be done to improve the performance of such a detection device.

EXPERIMENTAL DESIGN AND DESCRIPTION OF INSTRUMENTS

The employed laser was a Neodymium-Yttrium Aluminum Garnet (Nd:YAG) pumped dye laser that was operated with a repetition rate of 30Hz and an average

power of about (100mW@564nm). The advantage of this dye laser is its wavelength variability in a certain wavelength interval. Rhodamin6G Perchlorate with a laser output maximum at 563nm and a range from 552nm to 582nm was chosen as laser dye. Output power of the laser was monitored with a digital power meter (Scientech, Model 365) and recorded by a PC AT 386/20Mhz. In order to improve the beam profile of the laser, the laser beam was sent through a horizontal and vertical razor blade aperture before entering the cell. This leads to a slight power loss, but resulted in a reduced scattering signal detected by the PMT.

The detection cell was a coated aluminum block consisting of two chambers and ports for a laser beam entrance and exit arm, a nozzle port, a vacuum port and a PMT port. Figure 27 shows the profile of the Two-Chamber-Detection-Cell. Measurements of pressure were made with a DV6M thermocouple gauge from Hastings which was connected to both chambers of the detection cell via a three-way switch to ensure independent readings. A two-stage pump provided the necessary pumping speed to reach the desired low pressure region. This was also made possible by employing a 3-inch plastic vacuum hose as a connection between the pump and vacuum port of the cell, which proved to be superior to hoses with smaller diameters. Since the hose was transparent, a cover was necessary to prevent stray light from reaching the cell. This was ensured by wrapping several layers of black plastic foil around the hose.

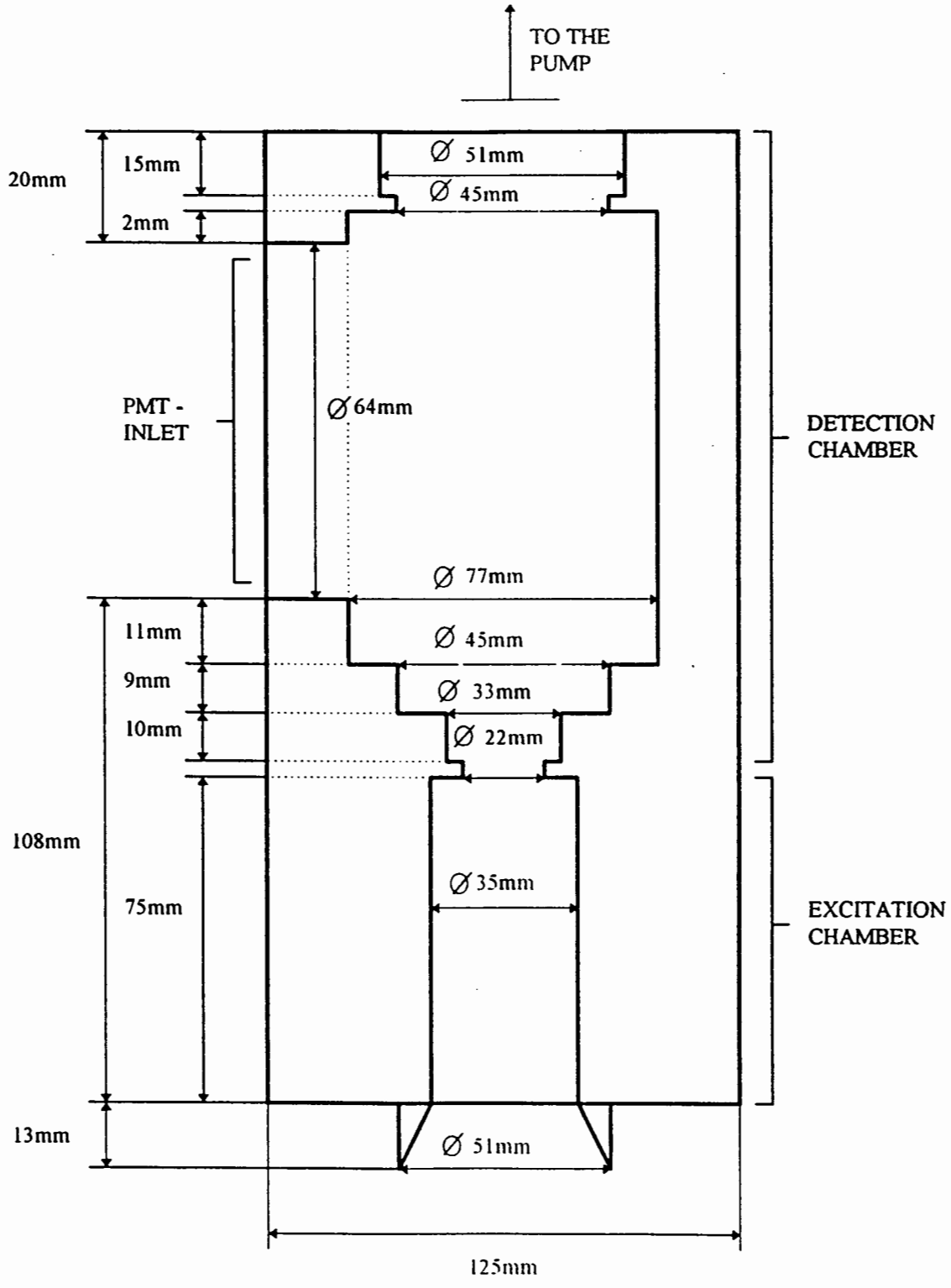

Figure 27. Profile of the Two-Chamber-Fluorescence-Cell.

Special focus was put on the nozzle design. The final shape can be seen in Figure 28. Spacers of variable thickness and interchangeable nozzle disks with diameters of 50μm, 75μm and 100μm enable a variation of inflow into the cell. The diameter of the opening between both chambers of the cell could be changed by using orifices with different diameters.

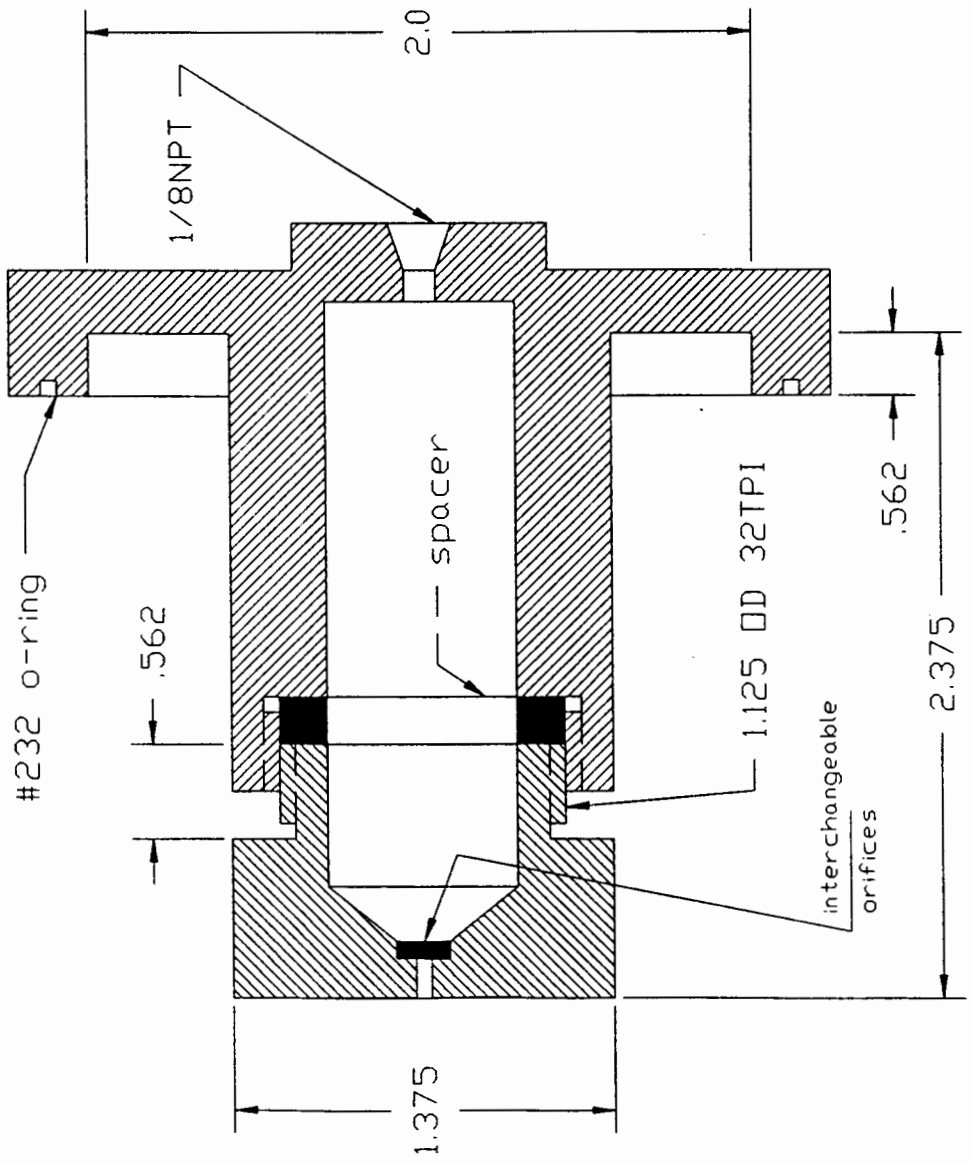

Figure 28. Schematic picture of the nozzle setup.

A major challenge was the reduction of the background signal due to scattering. One large source of the background signal is the scattering from laser light off the entrance and exit windows. This light can be detected as background signal when it is able to enter the detection chamber of the cell. Light baffles, made from absorbing paper, were positioned within the window arms in order to reduce the intensity of window scattering reaching the detection chamber. The size of the aperture is a compromise between the desire to minimize the scatter reaching the detection zone (decreasing baffle diameter) and minimizing the possibility that the laser beam hits the baffle (increasing baffle diameter). Placement of the baffles in the window arms was determined by the desire to avoid back reflection of scatter into the excitation chamber and therefore increasing the possibility of further reflection into the detection chamber. This results in a positioning of the baffle further away from the excitation zone. Regrettably, a positioning of the baffles too far away from the excitation zone does not provide optimal scatter attenuation. The compromise achieved in the final baffle configuration is shown in Figure 29. The optimal baffle setup was determined by peering into the excitation chamber with room lights turned off and connecting the PMT with an oscilloscope to optimize the signal, while various configurations of baffle size and placements were used. Since measured fluorescence is visible light, room light entering through the entrance and exit arms contributes to the background signal. Reduction of incoming room light was accomplished by attaching black tubing over the exit and entrance window arm.

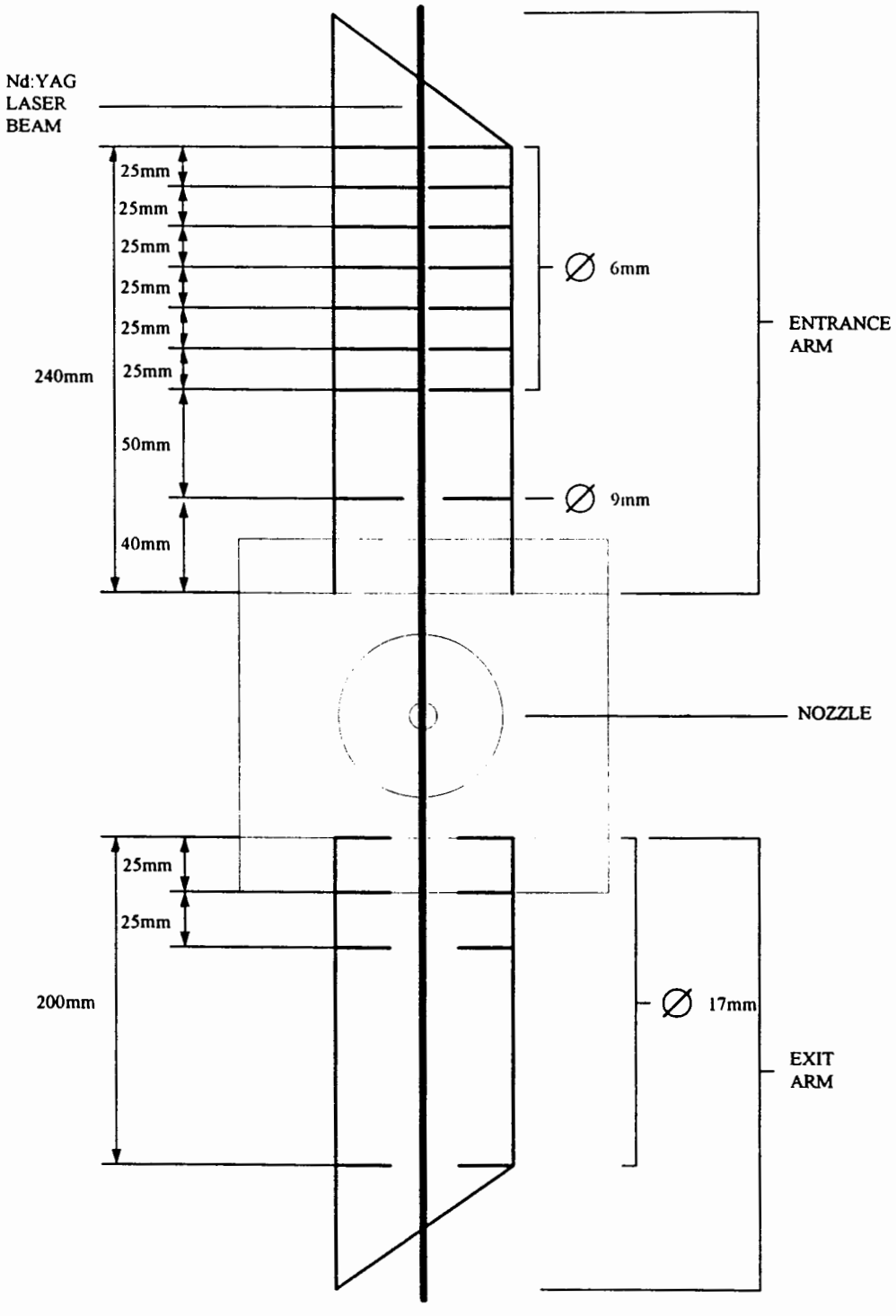

Figure 29. Optimal baffle placement in entrance and exit arm. Angle of the entrance and exit window corresponds to the Brewster Angle for glass.

Another way of reducing the detected scattering light and achieving an acceptable SNR is in varying the diameter of the orifice between both chambers of the cell. However, while a reduction of the diameter results in a decrease of the detected scatter, it also limits the amount of excited NO_2 molecules that reach the detection chamber of the cell by restricting the flow and causing different pressures in the excitation chamber with different diameters of the orifice for one and the same nozzle used.

The photon detection device was an EMI 9816B photomultiplier tube operating at 2200 Volts. The PMT was connected to a 400MHz oscilloscope (TEK 2467B) that was triggered via a MRD 500 trigger diode placed behind the first of two reflective coated mirrors in front of the cell. Intensity vs. time curves displayed by the oscilloscope were digitized by a digitizing camera system TEK DCS01GPH which was directly set up onto the oscilloscope screen. DCS software was running on a PC AT 286/6MHz. In order to make on-line changes in the camera setup, a video monitor was connected to the video output of the DCS card in the computer.

Figure 30 shows the experimental set up including the calibration system. Dry N_2 flow is sent via an $FeSO_4$ converter and a massflowmeter into a 50 liter Teflon bag. The $FeSO_4$ converter assures that NO_2 molecules within the dry N_2 are converted to NO via chemical reaction and therefore do not contribute to the signal detected. After filling the Teflon bag with a known volume of N_2, the needle valve near the massflowmeter is closed in order to prevent backflow from the Teflon bag. The other needle valve serves as flow restriction. NO_2 gas is injected into the Teflon

bag to provide an NO_2 - N_2 mixture of known NO_2 concentration which is provided to the nozzle via a three-way valve. Dry N_2 flow is also provided via the three-way valve to the nozzle in order to make background measurements. The three- way valve is connected to a microcomputer to provide flow control. For additional flow control a second pressure gauge (Pennwalt 61C-ID-0800) was established between the three-way valve and the nozzle. All tubing used for the calibration systems was made out of Teflon.

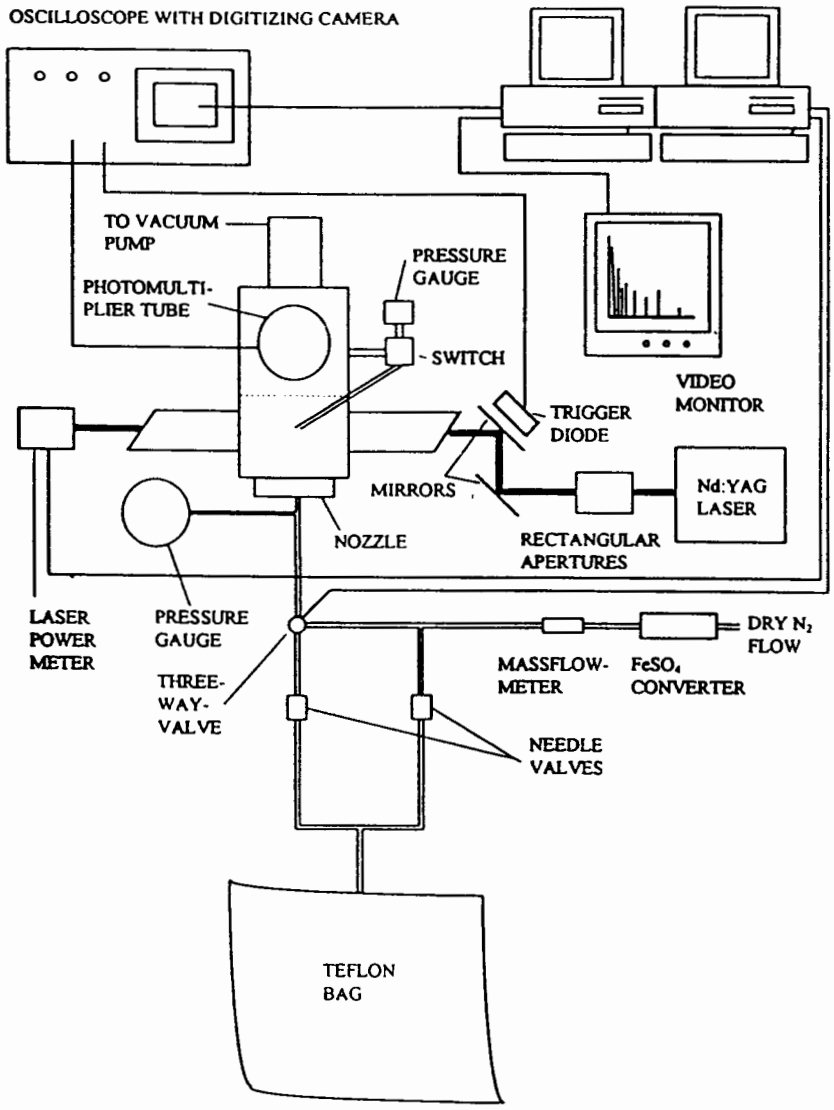

Figure 30. Experimental setup.

FLOW REGIME IN A TEST CELL

An important question to answer is whether or not it is justified to believe that signals observed by the detection devices really originate from excited NO_2 molecules decaying in the detection chamber. One way to clarify this question is to model the flow regime in the cell by using the program Quick and Simple by G.Recktenwald and S.Forbes. Since this was already done for the flow regime in a hypothetical experimental set up proposed in Chapter II, the discussion of details and limitations of this program and the modeling approach are described in the preceding chapter.

Modeling was done for all experimental set-ups referring to the input nozzle diameter in variation with chosen diameters of the orifice between both chambers of the cell. All calculations made were based on the actual measured pressure in the first chamber of the cell. Table 4 shows the predicted values for certain locations in the jet that is expanding into the first chamber from a nozzle with the diameter of d_0=100μm.

Absolute temperature at the nozzle exit is calculated to be 244K and the static pressure 401torr regardless of the diameter of the nozzle. Since a converging nozzle was used, the Mach number at the nozzle exit does not exceed the value of one and the absolute velocity for this special case is 313m/s .

As stated in Chapter III, the predicted flow properties immediately behind the Mach disk were used as input for the employed program. A flat velocity profile was chosen as profile of the inflow into the first chamber, since due to the rapid jet

expansion from the nozzle into the first chamber it can be assumed that by the time the jet flow passes the Mach disk, no velocity profile had been fully developed yet.

Table 4. Predicted flow characteristics for inflow nozzle diameter d_0=100μm, stagnation temperature T_t=290K and stagnation pressure p_t=760torr.

Diameter of the orifice between the two chambers,[cm]	measured pressure in the first chamber,[mtorr]	predicted flow properties shortly before the Mach disk	predicted flow properties shortly after the Mach disk	Mach disk location and diameter
2.0	40	M=22.1 T=3K v=763m/s p=0.083mtorr $\rho=1.278\ 10^{-5}kgm^{-3}$	T=288K v=129m/s p=47mtorr $\rho=7.637\ 10^{-5}kgm^{-3}$ $\mu=1.595\ 10^{-5}kgm^{-1}s^{-1}$ $D=0.209m^2s^{-1}$	x_m=9.2mm D_m=5.0mm
1.5	49	M=21.1 T=3.2K v=757m/s p=0.101mtorr $\rho=1.462\ 10^{-5}kgm^{-3}$	T=280K v=127m/s p=54mtorr $\rho=8.737\ 10^{-5}kgm^{-3}$ $\mu=1.533\ 10^{-5}kgm^{-1}s^{-1}$ $D=0.175m^2s^{-1}$	x_m=8.3mm D_m=4.5mm
0.9	131	M=17.3 T=4.8K v=760m/s p=0.429mtorr $\rho=4.142\ 10^{-5}kgm^{-3}$	T=284K v=129m/s p=150mtorr $\rho=2.469\ 10^{-4}kgm^{-3}$ $\mu=1.597\ 10^{-5}kgm^{-1}s^{-1}$ $D=0.065m^2s^{-1}$	x_m=5.1mm D_m=2.7mm

Figures 31, 32 and 33 show the obtained velocity distributions over the whole cell for the conditions mentioned above. "Slicing" of the surface plot along a certain location of the cell width would give the velocity profile at this point.

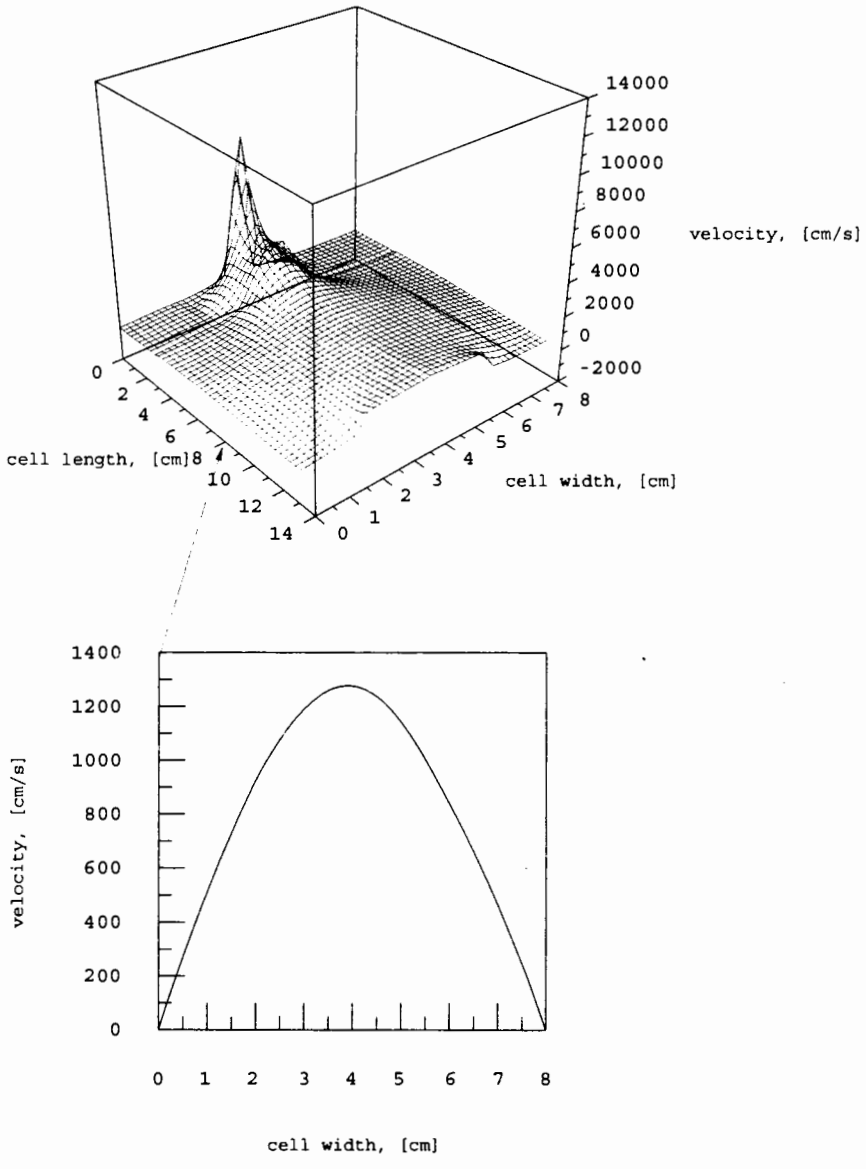

Figure 31. Velocity distribution for nozzle diameter of d_0=100μm and diameter of the orifice between both chambers of the cell $d_{orifice}$=2cm. Re with respect to the Mach disk diameter and the flow properties behind the Mach disk was 3.1. QUICK was the numerical algorithm used. The grid size was 43x42.

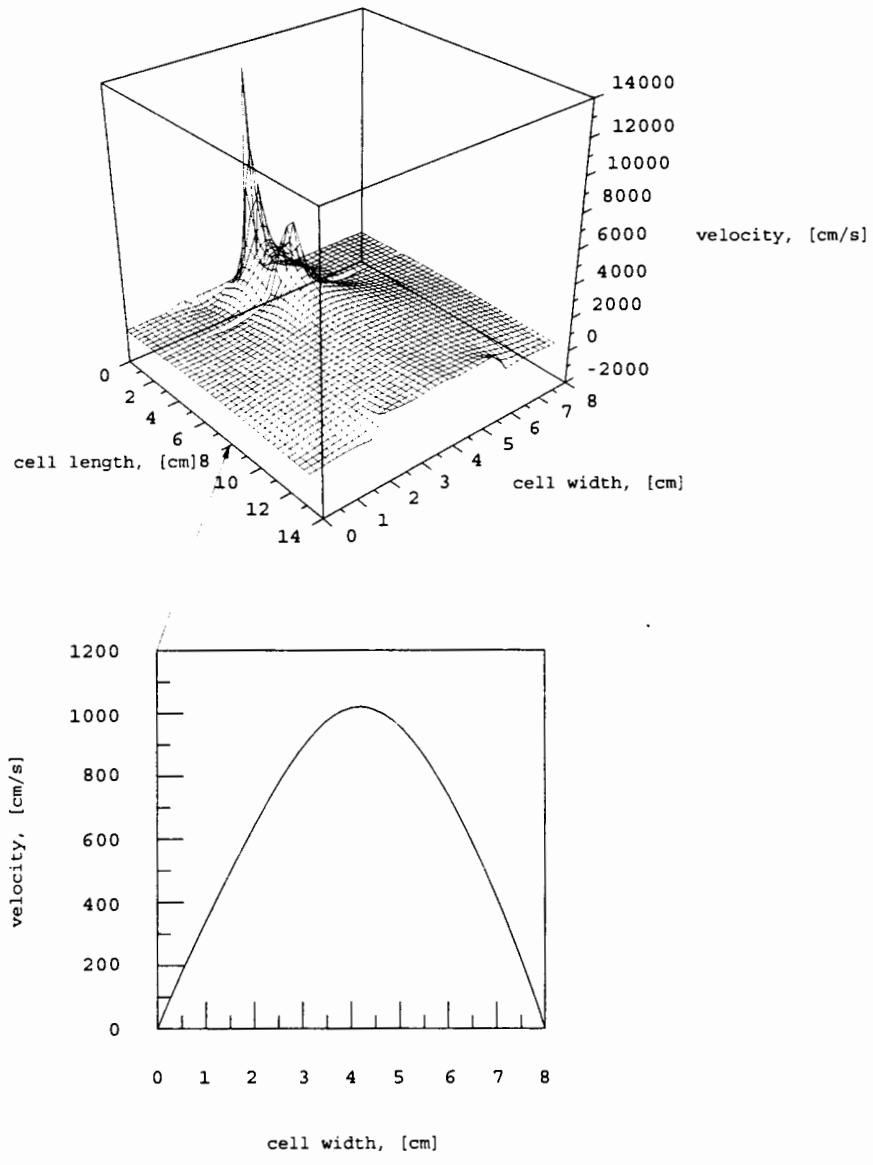

Figure 32. Velocity distribution for nozzle diameter of d_0=100μm and diameter of the orifice between both chambers of the cell $d_{orifice}$=1.5cm. Re with respect to the Mach disk diameter and the flow properties behind the Mach disk was 2.9. QUICK was the numerical algorithm used. The grid size was 45x41.

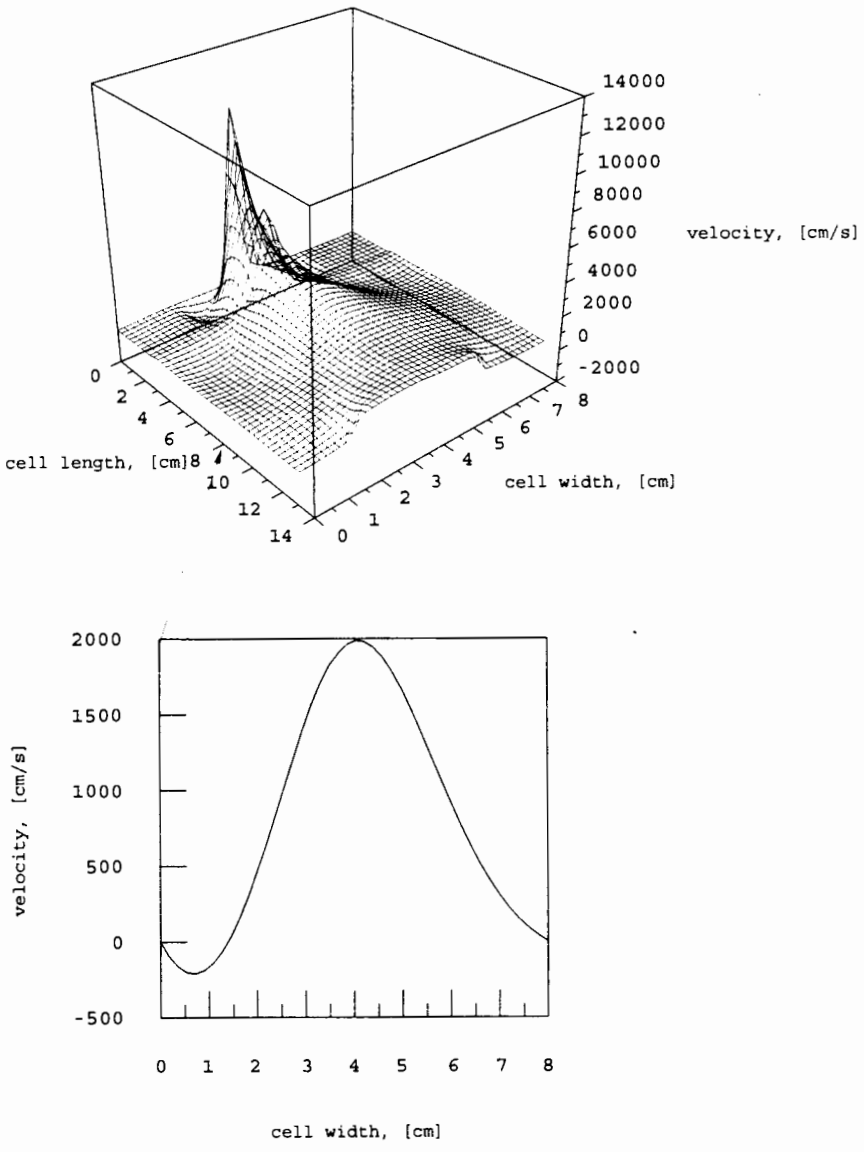

Figure 33. Velocity distribution for nozzle diameter of d_0=100μm and diameter of the orifice between both chambers of the cell $d_{orifice}$=0.9cm. Re with respect to the Mach disk diameter and the flow properties behind the Mach disk was 10.0. QUICK was the numerical algorithm used. The grid size was 43x41.

The figures clearly show the influence of the diameter of the orifice between both cells on the velocity distribution. A decrease in orifice diameter results in sharper velocity profiles for all locations in the first chamber. In addition, the jet gets more confined and the gas accelerates to higher velocities while passing the orifice. Occurring eddies, indicated by negative velocities, are growing with decreasing orifice diameter. This is due to the limiting effect of the orifice diameter on the expanding cone which leads to more backstream towards the inflow nozzle, and therefore to larger eddies and increasing entrainment into the expanding jet.

The passage of the orifice between both chambers is followed by an expansion into the second chamber. This causes the velocity profiles at the beginning of the second chamber to be sharper and then to become broad and parabola-like. Magnitudes of the velocities in the second chamber are significantly smaller compared to those in the first chamber. The results of the smallest modeled orifice of $d_{orifice}$=9mm show that for this diameter maximum velocities in the second chamber are significantly higher and also the velocity profiles tend to be sharper than in the cases of larger diameters of the orifice between both chambers of the cell. In contrast to the other cases, the velocity profile is not symmetric and more eddies occur.

In general it can be said that the major fraction of the inflowing gas stays in the jet core or its vicinity and does not get trapped in the occurring eddies. Therefore, according to the model results, most of the excited molecules would make it over to the detection chamber. How fast this happens and what influence this has on the

fluorescence quantum yield of the detection chamber will be shown in the next paragraph.

Tables 5 and 6 show the predicted values for certain locations in the jet that is expanding into the first chamber from a nozzle with the diameter of d_0=75μm and 50μm respectively. Figures 34, 35 and 36 give the model results for the nozzle with the diameter of d_0=75μm and Figure 37, 38 and 39 for the nozzle with a diameter of d_0=50μm.

Table 5. Predicted flow characteristics for inflow nozzle diameter d_0=75μm, stagnation temperature T_t=290K and stagnation pressure p_t=760torr.

Diameter of the orifice between the two chambers,[cm]	measured pressure in the first chamber,[mtorr]	predicted flow properties shortly before the Mach disk	predicted flow properties shortly after the Mach disk	Mach disk location and diameter
2.0	26	M=24.1 T=2.5K v=763m/s p=0.047mtorr $\rho=8.712\ 10^{-6}kgm^{-3}$	T=282K v=127m/s p=32mtorr $\rho=5.209\ 10^{-5}kgm^{-3}$ $\mu=1.566\ 10^{-5}kgm^{-1}s^{-1}$ $D=0.301m^2s^{-1}$	x_m=8.6mm D_m=4.6mm
1.5	35	M=22.7 T=2.8K v=761m/s p=0.065mtorr $\rho=1.076\ 10^{-5}kgm^{-3}$	T=286K v=129m/s p=39mtorr $\rho=6.431\ 10^{-5}kgm^{-3}$ $\mu=1.606\ 10^{-5}kgm^{-1}s^{-1}$ $D=0.250m^2s^{-1}$	x_m=7.4mm D_m=4.0mm
0.9	85	M=18.9 T=4.0K v=762m/s p=0.234mtorr $\rho=2.684\ 10^{-5}kgm^{-3}$	T=284K v=129m/s p=97mtorr $\rho=1.601\ 10^{-4}kgm^{-3}$ $\mu=1.586\ 10^{-5}kgm^{-1}s^{-1}$ $D=0.099m^2s^{-1}$	x_m=4.7mm D_m=2.5mm

Table 6. Predicted flow characteristics for inflow nozzle diameter d_0=50μm, stagnation temperature T_t=290K and stagnation pressure p_t=760torr.

Diameter of the orifice between the two chambers,[cm]	measured pressure in the first chamber,[mtorr]	predicted flow properties shortly before the Mach disk	predicted flow properties shortly after the Mach disk	Mach disk location and diameter
2.0	14	M=27.3 T=2.0K v=764m/s p=0.018mtorr $\rho=4.278\ 10^{-6}kgm^{-3}$	T=284K v=128m/s p=16mtorr $\rho=2.560\ 10^{-5}kgm^{-3}$ $\mu=1.585\ 10^{-5}kgm^{-1}s^{-1}$ $D=0.619m^2s^{-1}$	x_m=7.8mm D_m=4.2mm
1.5	13	M=27.7 T=1.9K v=765m/s p=0.017mtorr $\rho=4.146\ 10^{-6}kgm^{-3}$	T=285K v=129m/s p=15mtorr $\rho=2.481\ 10^{-5}kgm^{-3}$ $\mu=1.589\ 10^{-5}kgm^{-1}s^{-1}$ $D=0.641m^2s^{-1}$	x_m=8.1mm D_m=4.3mm
0.9	41	M=22.0 T=3.0K v=763m/s p=0.083mtorr $\rho=1.282\ 10^{-5}kgm^{-3}$	T=285K v=128m/s p=47mtorr $\rho=7.676\ 10^{-5}kgm^{-3}$ $\mu=1.597\ 10^{-5}kgm^{-1}s^{-1}$ $D=0.208m^2s^{-1}$	x_m=4.6mm D_m=2.4mm

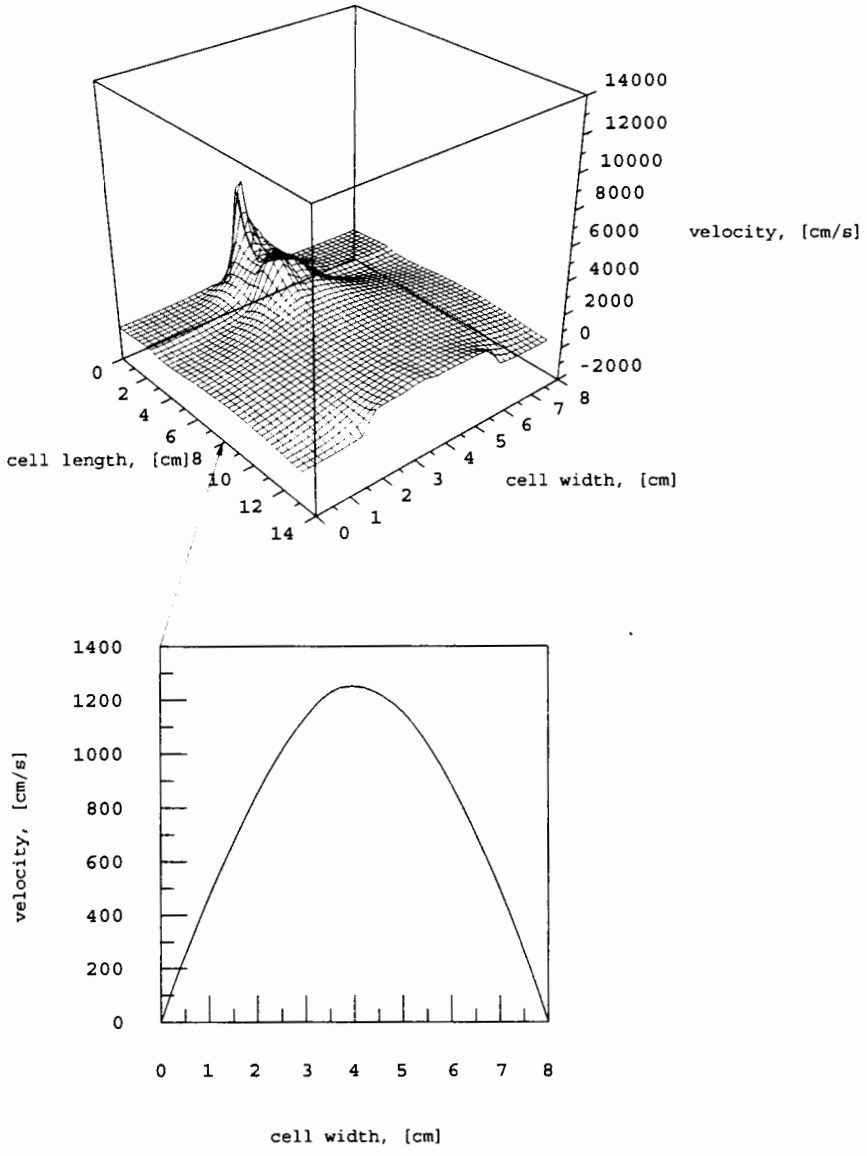

Figure 34. Velocity distribution for nozzle diameter of d_0=75μm and diameter of the orifice between both chambers of the cell $d_{orifice}$=2.0cm. Re with respect to the Mach disk diameter and the flow properties behind the Mach disk was 1.9. QUICK was the numerical algorithm used. The grid size was 41x41.

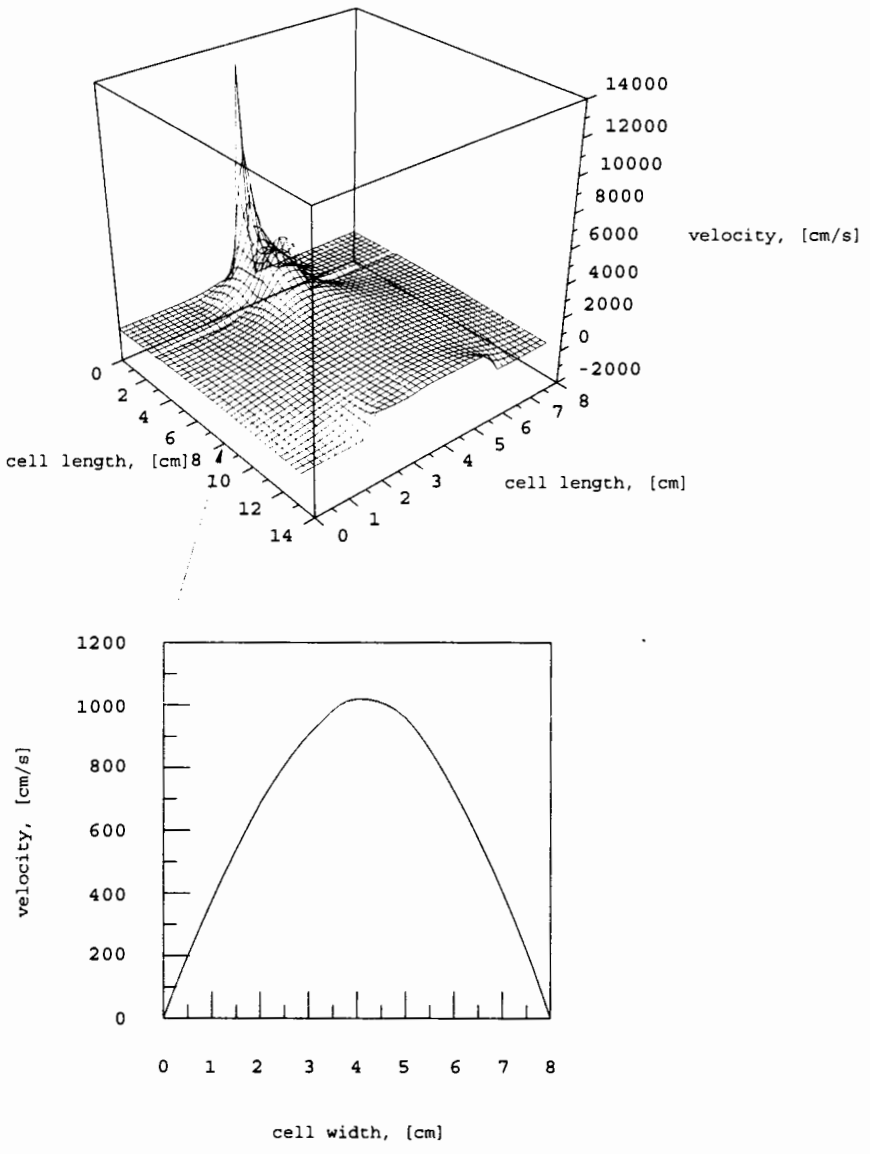

Figure 35. Velocity distribution for nozzle diameter of d_0=75μm and diameter of the orifice between both chambers of the cell $d_{orifice}$=1.5cm. Re with respect to the Mach disk diameter and the flow properties behind the Mach disk was 2.1. QUICK was the numerical algorithm used. The grid size was 41x41.

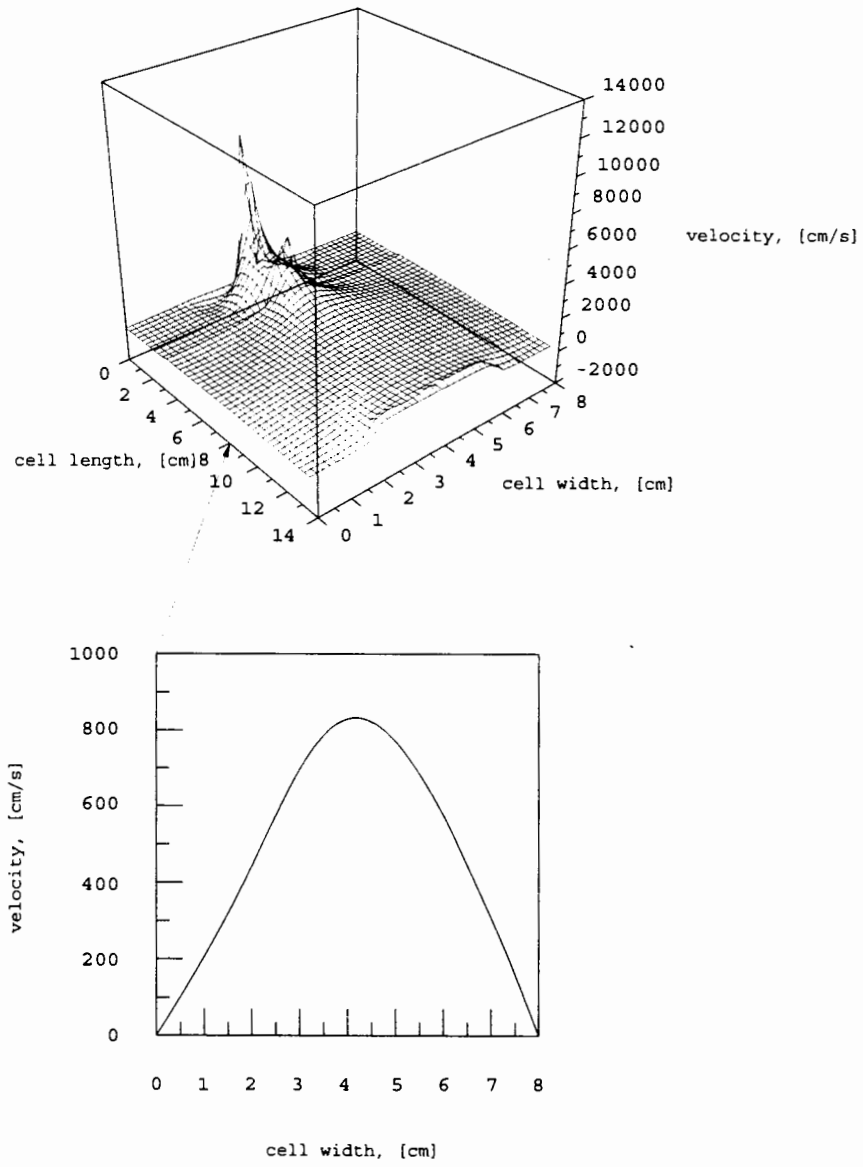

Figure 36. Velocity distribution for nozzle diameter of d_0=75μm and diameter of the orifice between both chambers of the cell $d_{orifice}$=0.9cm. Re with respect to the Mach disk diameter and the flow properties behind the Mach disk was 3.3. QUICK was the numerical algorithm used. The grid size was 40x41.

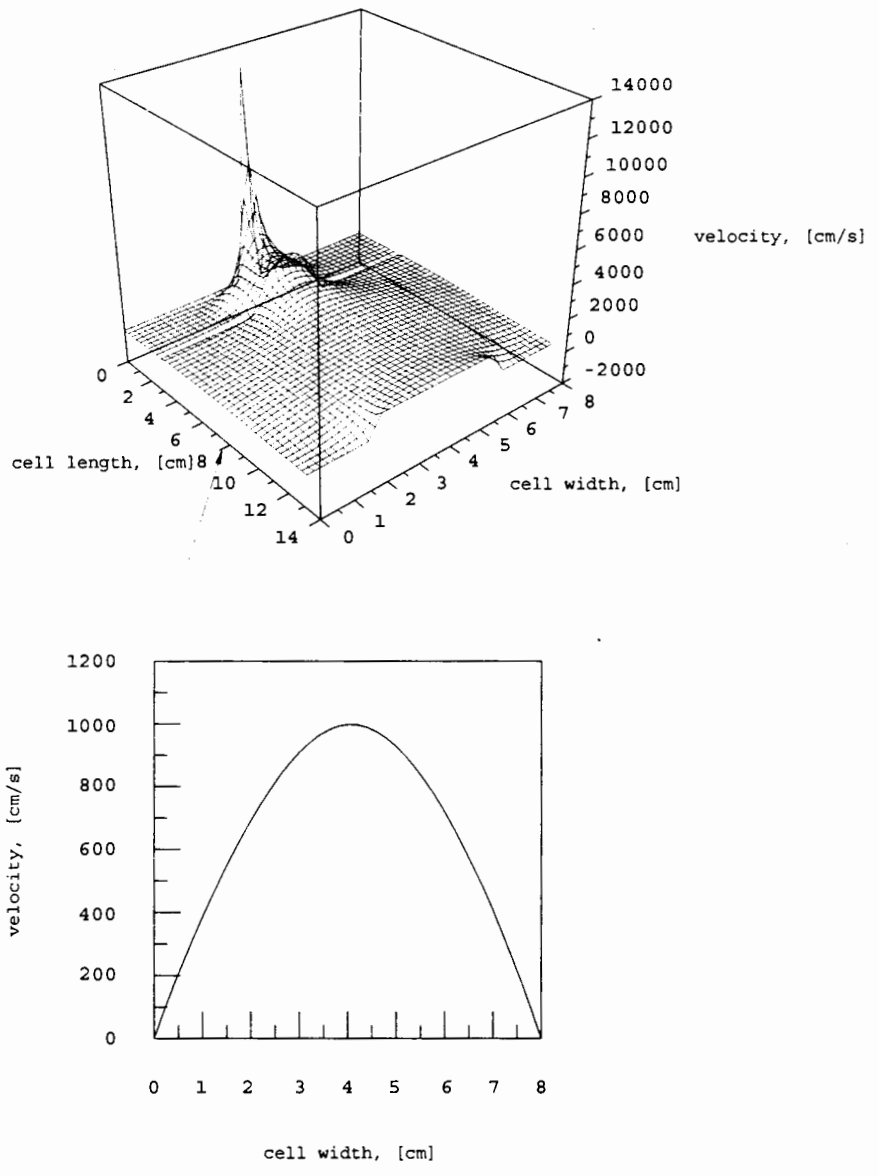

Figure 37. Velocity distribution for nozzle diameter of d_0=50μm and diameter of the orifice between both chambers of the cell $d_{orifice}$=2.0cm. Re with respect to the Mach disk diameter and the flow properties behind the Mach disk was 0.9. QUICK was the numerical algorithm used. The grid size was 41x41.

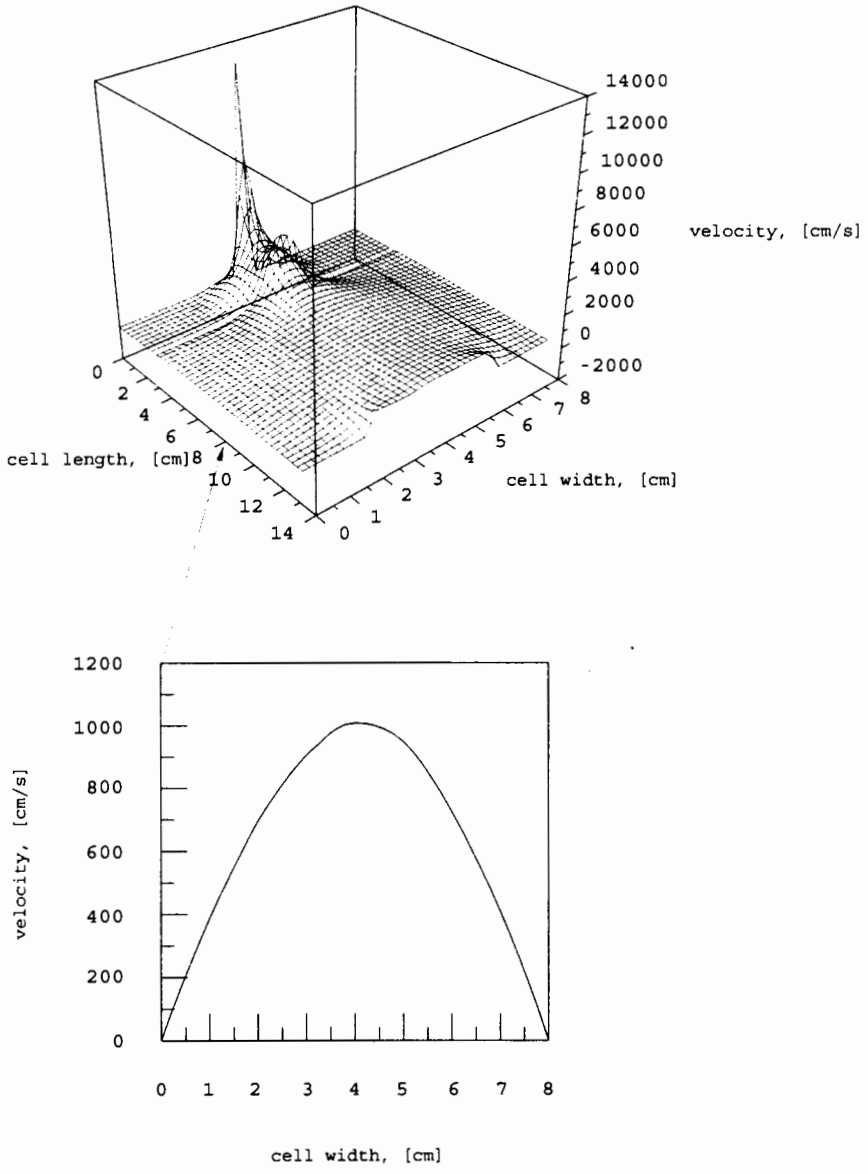

Figure 38. Velocity distribution for nozzle diameter of d_0=50μm and diameter of the orifice between both chambers of the cell $d_{orifice}$=1.5cm. Re with respect to the Mach disk diameter and the flow properties behind the Mach disk was 0.9. QUICK was the numerical algorithm used. The grid size was 41x41.

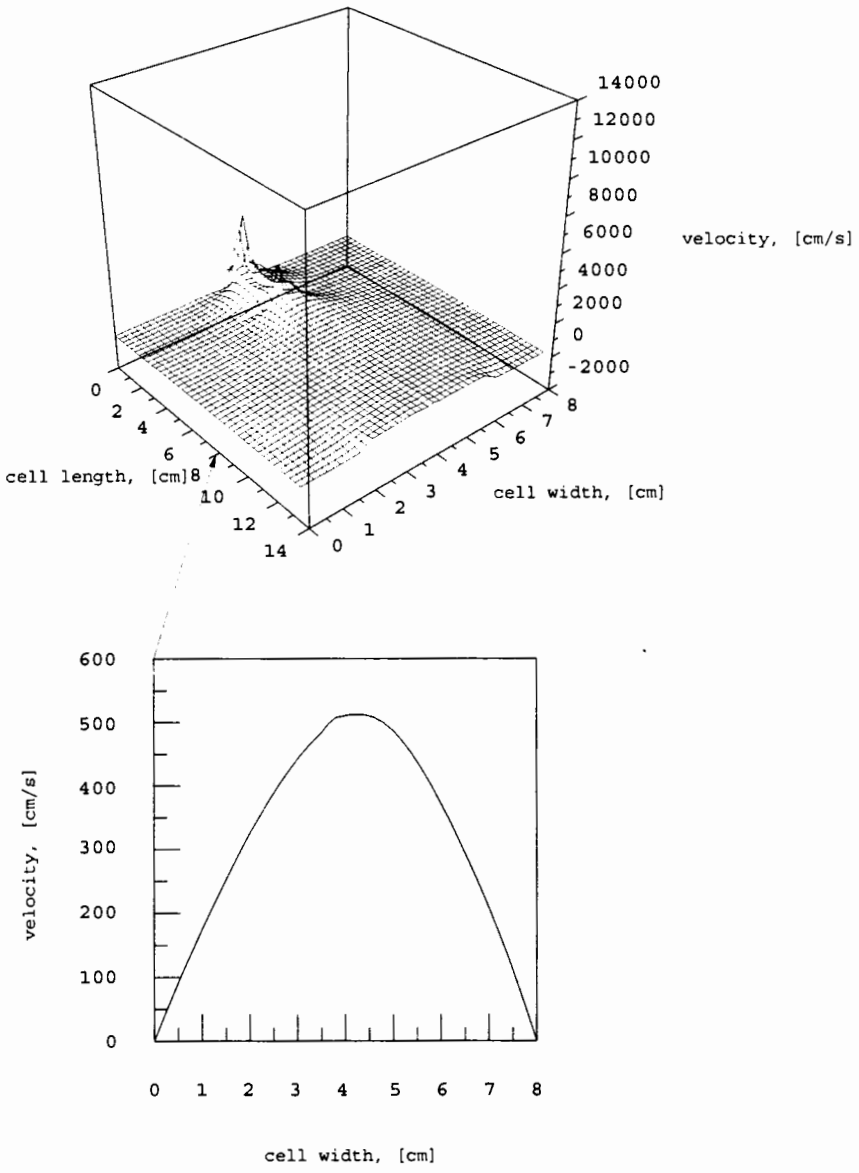

Figure 39. Velocity distribution for nozzle diameter of d_0=50μm and diameter of the orifice between both chambers of the cell $d_{orifice}$=0.9cm. Re with respect to the Mach disk diameter and the flow properties behind the Mach disk was 1.5. QUICK was the numerical algorithm used. The grid size was 40x41.

While comparing the results for a fixed diameter of the inflow nozzle but with a varying diameter of the orifice between both chambers, a similar conclusion as mentioned above can be drawn. However, if results for fixed diameters of the orifice between both chambers but with a varying diameter of the inflow nozzle are compared, less inflow due to smaller diameters of the choked inflow nozzle seems to weaken occurring eddies in the first chamber. The resulting reduced inflow into the second chamber leads to a decline in the effects of expansion in the second chamber, which can be summarized by fewer occurring eddies and a lower magnitude of velocities in the second chamber.

Considering the calculated results in Tables 4, 5 and 6 raises the very important question of where to let the laser beam cross the jet flow. An excitation of the NO_2 molecules at a location before the Mach disk would certainly benefit from very low quenching rates due to the very low densities of the gas, but also would suffer from a loss of absorption rates for the same reasons. In addition, the undergoing rapid changes of flow properties while passing the normal shock seem to circumvent all advantages of excitation before the Mach disk since it seems that quenching would increase significantly while passing the normal shock. Excitation at a location behind the Mach disk assures high absorption rates, but also is characterized by more quenching due to higher densities, as well as increased thermal and less directed motion of the molecules in one direction.

Another advantage of excitation before the Mach disk is the effect of temperature on the rotational population. Since the energy spacing between rotational

levels is sufficiently small, the contribution of available thermal energy at room temperature is sufficient enough to populate higher rotational levels. By excitation at room temperature, an excitation spectrum could be seen that consists of vibrational lines superimposed on a strong rotational background. Rotational lines can be suppressed by depopulation of higher rotational levels due to very low temperatures, which would yield to sharp vibrational features and less rotational background. Tuning the laser wavelength to such a strong absorption band would result in a higher signal usable for detection. Such low temperatures are provided by the jet expansion before passing the Mach disk. An excitation of the incoming NO_2 molecules would certainly take advantage of this. But still, these excited molecules would have to pass the Mach disk.

FLUORESCENCE SIGNAL

This paragraph shall yield an evaluation of the theoretical performance of the provided Two-Chamber-NO_2-Fluorescence-Cell. This can be done by calculating the fluorescence signal achievable by this particular set up. The starting point is Equation 3 derived in Chapter II. Since the incident intensity of the laser beam and the absorption cross section are parameters which depend on the laser system used, the only variable that must be adjusted to the current setup is the fluorescence quantum

yield Φ. The fluorescence quantum yield for this particular setup can be obtained beginning with Equation 29 derived in Chapter II.

$$\Phi = \frac{k_f[M_I]}{(k_q[M_{II}]+k_f)[M_0]}\left\{exp\left[-(k_q[M_I]+k_f)t_{RI}\right] - exp\left[-(k_q[M_{II}]+k_f)t_{RII} + ([M_{II}]-[M_I])t_{RII}k_q\right]\right\} \quad (54)$$

Special attention has to be given to the residence times in both chambers of the cell. The results in the preceding paragraph about the flow regime in the cell imply, that the flow in the first chamber could generally be described by plug flow. The residence time in the first chamber can therefore be described by

$$t_{RI} = \frac{\Pi r_1^2 l_1[M_I]}{188493 r_0^2[M_0]} \quad (55)$$

Modeling results also show that there is an intermediate regime between the desired exponential dilution and plug flow in the second chamber. Due to the more directed flow pattern and only minor eddies, the plug flow case was chosen to characterize the flow regime in the second cell. This also yields to a slight underestimation of the calculated fluorescence quantum yield in the detection chamber. Since the flow in this chamber can be idealized by a cone that is expanding from the radius of the orifice between both chambers, r_1, to the radius of the outflow orifice, r_2, the residence time t_{RII} can be calculated by the following expression.

$$t_{RII} = \frac{\pi l_2\left(r_1^2 + r_2^2 + r_1 r_2\right)[M_{II}]}{188493 r_0^2[M_0]} \quad (56)$$

l_2 and l_1 are the length of the first and second chambers respectively, r_0 the radius of the inflow nozzle, r_1 the radius of the orifice between both chambers and r_2 the radius of the outflow orifice. $[M_0]$ is the ambient pressure, while $[M_I]$ and $[M_{II}]$ represent the pressures in the first and second chambers. Substituting the corresponding residence times into Equation 53, plotting the resulting expression into Equation 3 and using different pressure units (mtorr) gives the following fluorescence signal Θ for the chosen setup.

$$\Theta = \frac{\bar{I}_0 \sigma_\lambda k_f p_1}{\left(\frac{k_q 0.133 p_2 N_a}{RT} + k_f\right) p_0} \left\{ exp\left[-\left(\frac{k_q 0.133 p_1 N_a}{RT} + k_f\right) \frac{\pi r_1^2 l_1 p_1}{188493 r_0^2 p_0} \right] - exp\left[-\left(\frac{k_q 0.133 p_2 N_a}{RT} + k_f\right) \frac{\pi l_2 \left(r_1^2 + r_2^2 + r_1 r_2\right) p_2}{188493 r_0^2 p_0} + \left(p_2 - p_1\right) \frac{\pi r_1^2 l_1 k_q 0.133 p_1 N_a}{188493 r_0^2 p_0 RT} \right] \right\} \quad (57)$$

Actually measured pressures are used for the calculation of the fluorescence signal for inflow nozzle diameters of 50μm, 75μm and 100μm. Calculation of the fluorescence signal for an inflow nozzle diameter of 20μm is based on extrapolated pressures. According to the available experimental equipment, the average laser output power was assumed to be 200mW@532nm, which gives an absorption coefficient σ_λ of 1.47 10^{-19}cm^{2}molec^{-1} and an incident intensity of the laser beam I_0 of 5.36 10^{17}photons s^{-1}. Graphs in Figure 40 show the calculated fluorescence signal for different inflow nozzle diameters and variable diameters of the orifice between both chambers.

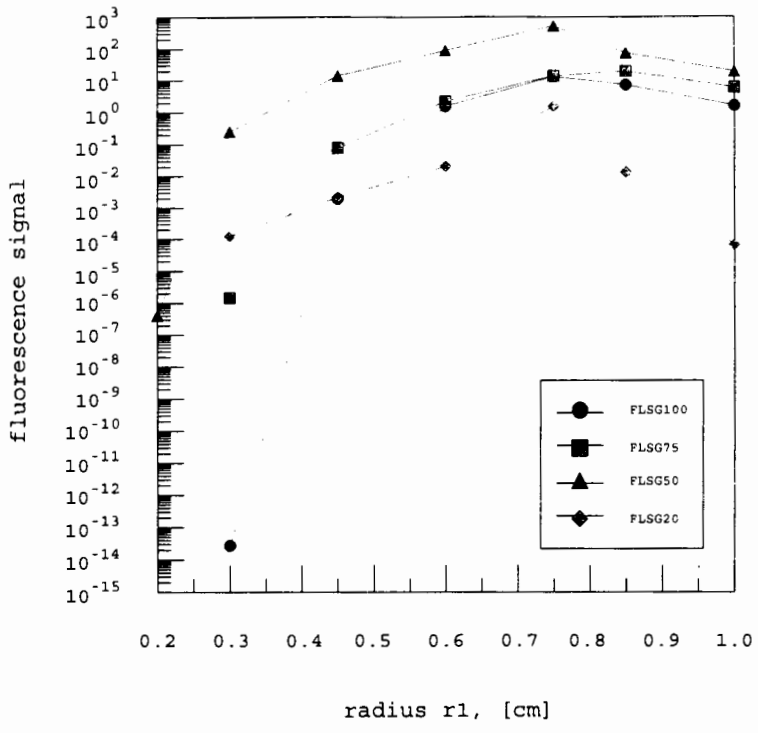

Figure 40. Fluorescence signal, Θ, vs. radius of the orifice between both chambers, r_1 , for different diffuser nozzle diameters, d_0. The fluorescence signal is calculated in photons per sec. and ppb of NO_2.
(FLSG100 refers to the calculated fluorescence signal Θ for d_0=100μm, FLSG75 to Θ for d_0=75μm, FLSG50 to Θ for d_0=50μm and FLSG20 to Θ for d_0=20 μm)

The graphs indicate that for all diameters of the inflow nozzle the fluorescence signal is rising with an increasing diameter of the orifice between both chambers and undergoes then a broad maximum. For one and the same inflow nozzle, increasing diameters of the orifice between two chambers has a lengthening influence on the residence time in the first chamber and leads also to less concentrations of the monitored species in the first chamber. These effects are compensated by resulting lower pressures and less quenching of the excited molecules. This causes the

fluorescence signal to rise. After reaching the maximum signal, the further lengthening of the residence time of the excited molecules in the first chamber overcomes the advantages of less quenching due to lower pressures and forces the fluorescence signal to decrease again.

Furthermore, it can be observed that all maxima seem to occur at around the same diameter of the orifice between both chambers. The magnitude of the maximum fluorescence signal is increasing with decreasing diameters of the inflow nozzle. This rise results in the fact that, although less inflow through the choked inflow nozzle provides less concentration of the monitored species and has a lengthening influence on residence time in the first chamber, these effects are more than compensated by lower cell pressures and less quenching. The more the diameter of the inflow nozzle is decreased, the more the lengthening of the residence time in the first chamber and the further declining analyte concentrations become dominant in their influence and cause the fluorescence signal to reach a maximum and to drop afterwards.

Referring to the results, the best theoretical set-up for this cell would be with a inflow nozzle of d_0=50μm and with an orifice between the both chambers of d_{orf}=1.5cm. However, the optimal set-up has still to be found experimentally and is determined by the behavior of the background signal for different set-ups, as well as the influence of quenching on the signal detected by the PMT in the second chamber. According to the calculations made, the chosen setup would yield a fluorescence signal Θ of 528 photons per second and ppb of NO_2 supplied to the detection cell.

This would result in a signal of 17 fluorescence photons per laser shot and ppb of NO_2, when the laser would have a repetition rate of 30Hz. Whether this signal is detectable or not, and how sensitive the measuring technique is, depends strongly on the background signal in the experimental setup employed. The improvement of the sensitivity by reducing the background signal would be a topic for further experimental research.

EXPERIMENTAL RESULTS

In this paragraph, the actual measured data are presented which were obtained by using the experimental set up in Figure 30. For technical reasons the nozzle inflow diameter was chosen to be d_0=100μm and the diameter of the orifice between both chambers of the cell was d_{orf}=1.5cm. This resulted in a pressure in the first chamber p_1 of 49mtorr and a pressure in the second chamber p_2 of 37mtorr. The supplied stream of dry nitrogen was seeded with an amount of 100ppm of NO_2. This is rather high but necessary to achieve any visual results on the screen of the oscilloscope. The supplied high voltage to the photomultiplier was 22kV. The final waveform averaged over 200 accumulated waveforms. Figure 41 shows the background and the gross signal accumulated for the conditions mentioned above. Subtracting the background signal from the gross signal leads to the net signal which can be seen in Figure 42.

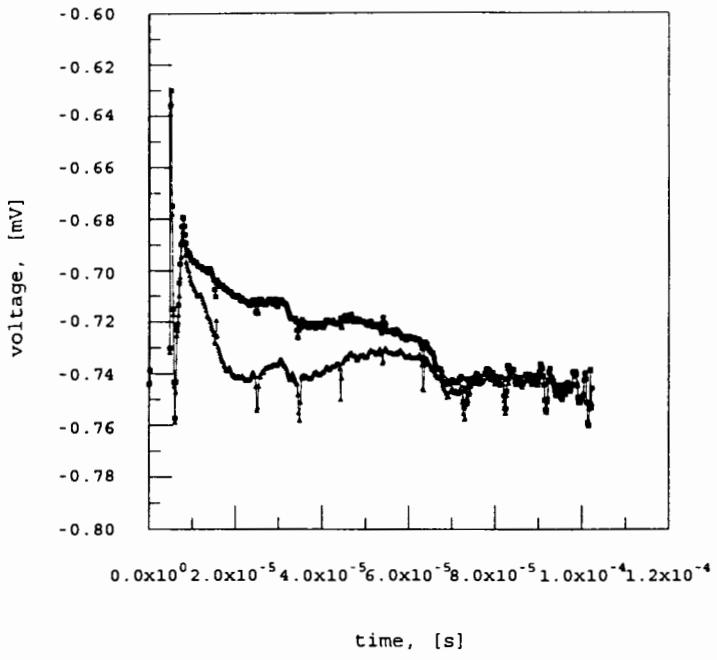

Figure 41. Background and gross signal for d_0=100μm, d_{orf}=1.5cm, p_1=49mtorr and p_2=37mtorr. The supplied voltage to the PMT was 22kV. Final signal averaged over 200 accumulated waveforms. The provided concentration of NO_2 was 100ppm. The average laser power was 119mW for both, the background and the gross signal measurement.
gross signal, background signal

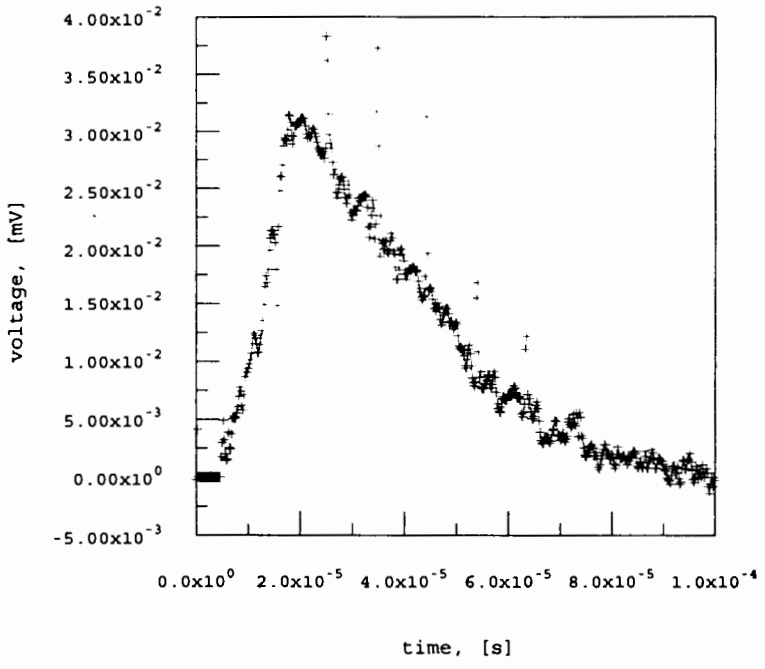

Figure 42. Net signal for d_0=100μm, d_{orf}=1.5cm, p_1=49mtorr and p_2=37mtorr. The supplied voltage to the PMT was 22kV. Final signal averaged over 200 laser shots. The provided concentration of NO_2 was 100ppm. Average laserpower is 119mW.

Both figures show that after the laser fires and triggers the oscilloscope, it takes the PMT about 5μs to start detecting any incoming signal at all. Since even scattered photons would have passed by this time, this behavior is due to saturation effects of the PMT caused by the scattered photons originating from the laser beam. After this incoming saturation peak, both signals -the background and the gross signal- start building up with time. But Figure 41 also shows that even after the saturation peak, this behavior is due to a rising background. The second peak, which occurs around 10μs might be due to some ringing or electronical pick up which extends until about 17μs. The rising and falling part of the fluorescence signal can be seen in Figure 42. According to Figure 42 the fluorescence decay curve also undergoes a maximum at around 20μs.

In order to determine whether or not the observed net signal is caused by fluorescence decay of excited NO_2 molecules, the declining part has to be observed in more detail. Figure 43 gives the smoothed declining part of the signal. According to the fluorescence characteristics, this curve should follow an exponential decay that is characterized by the effective fluorescence lifetime for the pressure combination employed.

$$I = I_0 \exp\left[-\frac{t}{\tau_{eff}}\right] \tag{58}$$

where I is the fluorescence intensity and I_0 the initial fluorescence intensity.

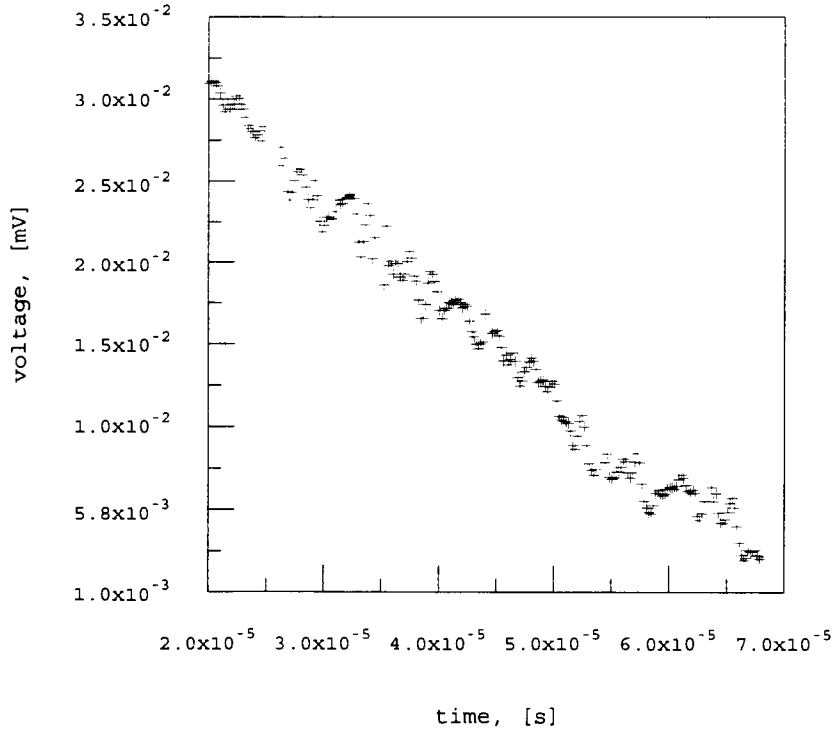

Figure 43. Enlargement of the region between 20μs and 70μs in Figure 42.

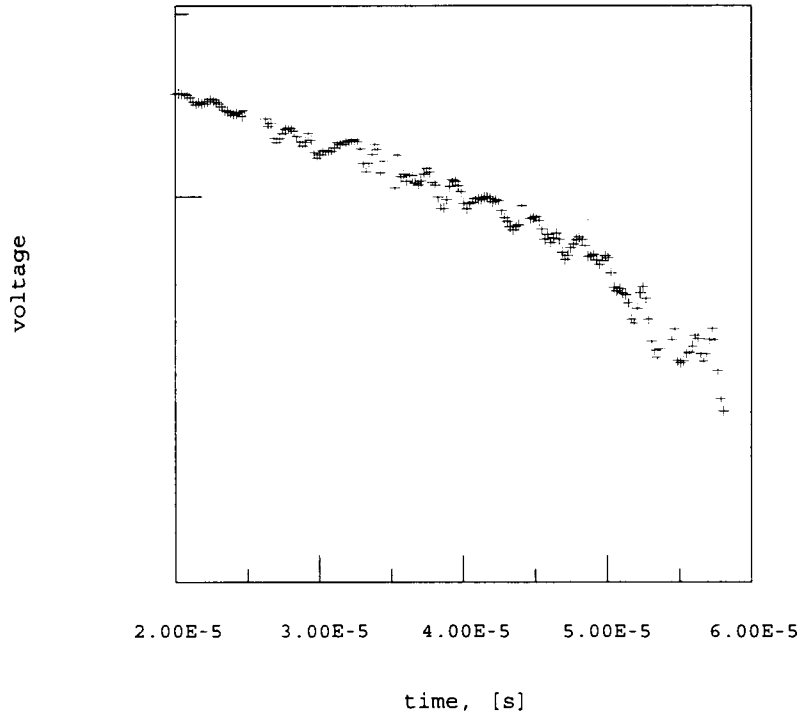

Figure 44. Logarithmic plot of Figure 43.

Analyzing the data shown in Figure 44 by linear regression should yield to the reciprocal value of the effective fluorescence lifetime for this particular set up. Analyzation results are listed in Table 7.

Table 7. Regression results.

reciprocal effective lifetime	$\tau_{eff}^{-1}=42657s^{-1}$
correlation coefficient	r=0.966

This would give an effective fluorescence lifetime of $\tau_{eff}=(23\pm4)\mu s$. Effective lifetimes based on the measured pressure in the first and the second chamber, τ_1 and τ_2, are $(12\pm1)\mu s$ and $(15\pm1)\mu s$, respectively. Due to the different pressures in both chambers, the fluorescence decay should be a combination of the decay curves at different pressures and therefore the effective fluorescence lifetime should be in between the calculated lifetimes.

The calculated effective lifetimes are based on a value for the quenching rate constant k_q for NO_2 quenching in nitrogen that was taken from the literature [George *et al.*, 1991]. Different, excited states of molecules are quenched with different rate constants. The sum over all quenching rate constants gives the effective quenching rate constant. Since the fluorescence spectra of NO_2 is pressure dependent, excited states might be differently populated and contribute differently to the effective quenching rate constant at different pressures. In addition, the effective quenching rate constant is a function of excitation wavelength. The value for the quenching rate constant of NO_2 in nitrogen that was taken from [George *et al.*, 1991], was

determined at much higher pressures and at other wavelengths than employed in this particular set up. This might explain the longer measured than calculated effective fluorescence lifetime. Therefore, the observed signal can be assigned to fluorescence decay of excited NO_2 molecules.

In order to determine whether or not the observed signal originates from molecules that fluoresce in the first chamber or from molecules which fluoresce while passing the orifice to or already within the second chamber, the rising part of the signal has to be discussed in detail. Calculation of the residence time of excited NO_2 molecules in the first chamber, based on data for this particular set-up, results in a value of (97±22)μs. This indicates that even the fastest molecules would not contribute to the signal by fluorescing in the second chamber. This conclusion would further be supported by evaluating the maximum velocities obtained in the flow modeling section for this particular set up according to Figure 32. Proceeding with the facts, the observed fluorescence signal might be partially due to decay of excited NO_2 molecules in the first chamber. Fluorescence photons get then directly or by reflection off the cell walls through the orifice between the two chambers into the second chamber.

CHAPTER IV

CONCLUSION

The question that still has to be answered is, whether or not a detection device based on a Two-Chamber-NO_2-Fluorescence-Cell-Principle could be built. Following the theoretical considerations in Chapter II, such a detection device could be created and would work with very high sensitivity, as long as the approximations made hold true in the practical case. The experimental section in Chapter III showed that regardless of the validity of most of the approximations made, the performance of the test cell did not quite satisfy the predictions made. An explanation can be found by taking a closer look at the flow regime in the test cell. All predictions and calculations on a possible fluorescence signal of the test cell were based on the assumption that most of the excited NO_2 molecules would be able to get into the detection chamber and fluoresce there. The detected fluorescence would then result in a fluorescence signal Θ of 10 photons per second and ppb of NO_2 for the used setup.

From the measurements on the test cell, it was concluded that the detected fluorescence signal was due to decay of excited NO_2 molecules that happened in the first chamber. The fluorescence signal for 100ppm NO_2 was observed from around

17μs to about 90μs, and then is indistinguishable from the background. A calculated residence time of around 97μs for the first chamber, based on the assumption of plug flow, indicates that no proof could be produced regarding a contribution to the fluorescence signal originating from excited NO_2 molecules decaying in the second chamber due to the high background signal. In addition, the real residence time of excited NO_2 molecules might be even longer than that, since the flow regime in the first chamber seems to be rather an intermediate case between plug flow and exponential dilution. This would lead to a further lengthening of the residence time in the first chamber. Considerations of the course of the modeled maximum velocity from the inflow nozzle to the Mach disk, Figure 45, and from the Mach disk to the orifice between both chambers, Figure 46, would also support the statement that the observed fluorescence signal in the test cell is mainly due to fluorescence decay that happens within the first chamber of the cell.

Nevertheless, even considering the fact that most of the observed fluorescence signal is due to decay of excited NO_2 molecules in the first chamber, the test cell is already an improvement to other measuring procedures due to its temporal and spatial separation of excitation and detection chamber. This results in a reduction of saturation effects of the detection device caused by scattered laser photons.

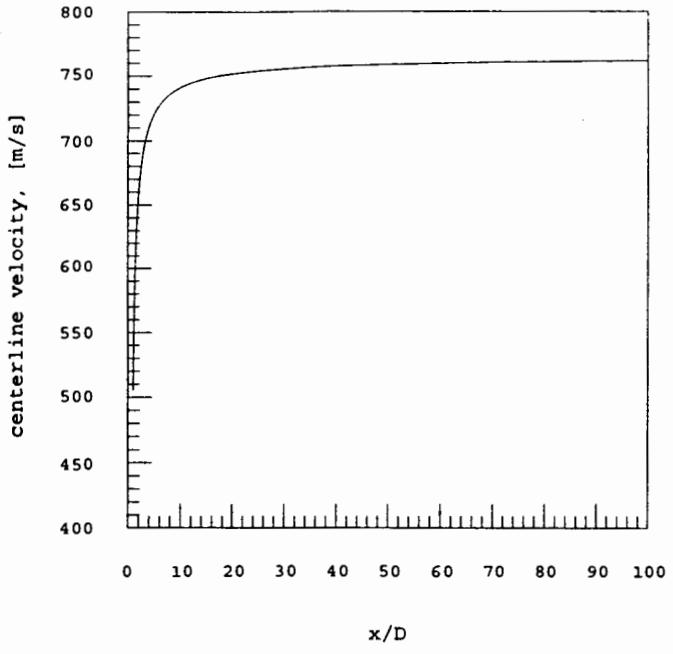

Figure 45. Absolute centerline velocity for the distance between the inflow nozzle and the Mach disk for the case of the test cell. d_0=100μm, d_1=1.5cm, p_1=49mtorr and p_2=37mtorr. The Mach disk is located at x/D=83.

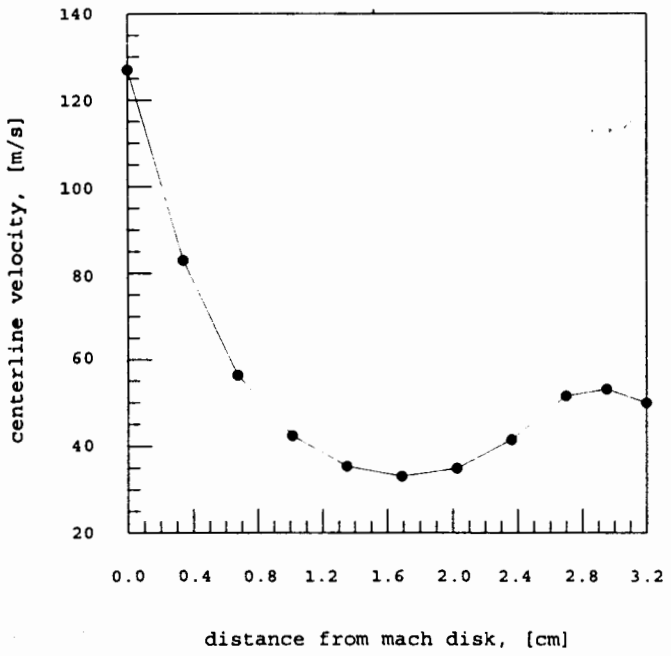

Figure 46. Maximum velocity at the centerline for the distance between the Mach disk and the orifice between the two chambers. Velocities are modeled with QnS. d_0=100μm, d_1=1.5cm, p_1=49mtorr and p_2=37mtorr.

From the results in Chapters II and III, another cell design can be suggested, that would ensure that the excited molecules get from the detection chamber into the excitation chamber and emit most of their fluorescence there. Figure 47 proposes a possible cell design.

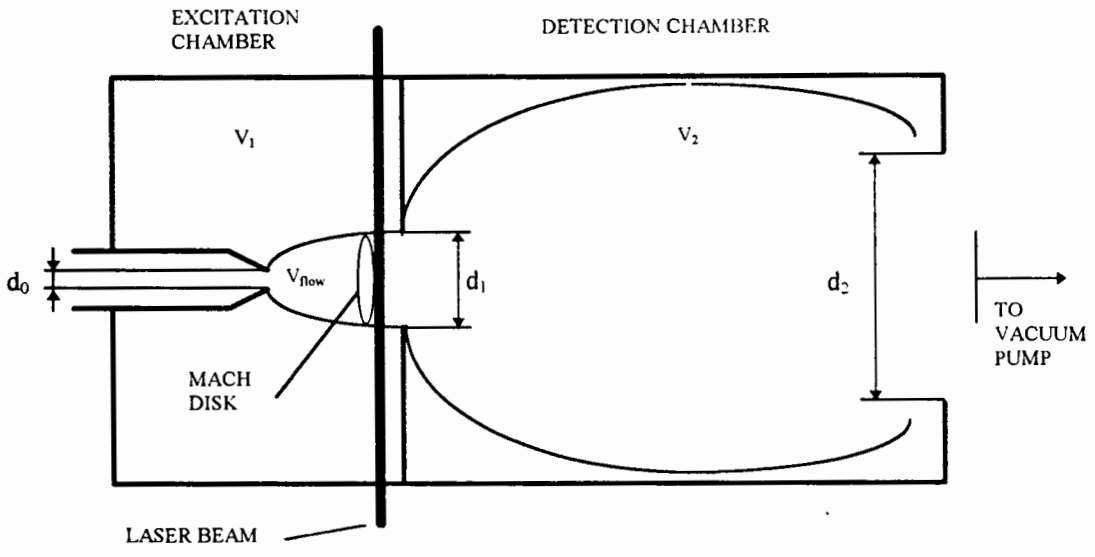

Figure 47. Proposed cell design of a Two-Chamber-NO_2-Fluorescence-Cell. Excitation occurs behind the location of the Mach disk.

The cell in Figure 47 should be characterized by a large inflow which can be provided by a large diameter of the inflow nozzle, by a small flow volume in the first chamber, V_{flow}, and by a large detection chamber volume, V_2. V_{flow} should be very small to ensure short residence times in the first chamber. Since the volume of chamber one, V_1, does not have any effect on the flow regime in the cell, it should be rather large compared to V_{flow}, in order to reduce the probability that scattered laser photons could get into the detection chamber by reflecting off the walls in the first chamber through the orifice between both chambers. Those conditions can be

provided by using a nozzle holder that can be varied in its location in the excitation chamber. Problems would occur by providing the optimal pressure combination for the cell. It has to be made sure that the orifice between both cells and also the outflow orifice are not choked. A choked orifice between the chambers would result in a second Mach disk in the detection chamber and a choked outflow orifice would prevent pressure variations in the same chamber. Choking of the orifice between the chambers could be prevented by introducing the method of differential pumping in the first chamber, if necessary. This would lower the pressure in the first chamber, but also changes the location and the diameter of the Mach disk.

Figure 47 also indicates, that the location of the Mach disk should be close to the orifice between both chambers, in case the excitation occurs behind the Mach disk. This certainly assures a low residence time in the first chamber, but also might be of a certain disadvantage due to the possibility that more laser photons would get directly into the detection chamber the closer the excitation occurs to the orifice between both chambers, regardless of the large volume of the first chamber. This has to be further investigated experimentally, as well as the effect which the diameter of the orifice between both chambers has with respect to the amount of scattered photons detectable by the detection device.

If it should be decided to excite the incoming NO_2 molecules already before passing the Mach disk and take advantage of low densities and low quenching rates, as well as low rotational temperatures, Figure 48 suggests a possible cell design. The only difference here to the cell design proposed earlier is a different pressure

combination in the cell, in order to provide pressure ratios of ambient pressure to pressure in the first cell, which would allow the Mach disk to form at the end of the second chamber.

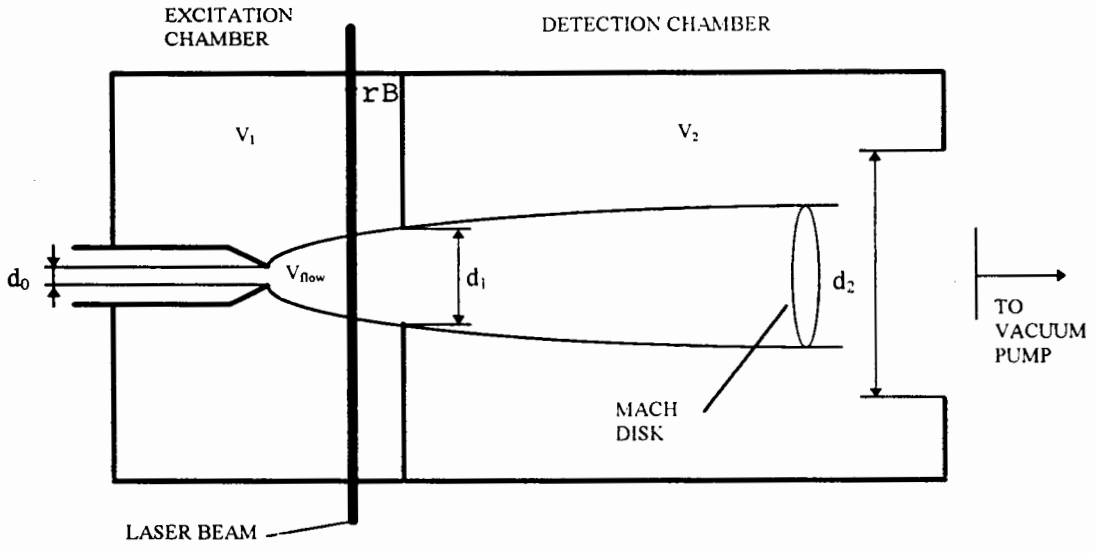

Figure 48. Proposed cell design of a Two-Chamber-NO_2-Fluorescence-Cell. Excitation occurs before the location of the Mach disk.

This could be achieved by differential pumping in the first chamber. Other ways to avoid the formation of a Mach disk are the usage of the orifice between both chambers as a skimmer or to ensure a jet expansion in the molecular flow region. An advantage would be that the location of the excitation by the laser beam is not limited to locations close to the orifice between both chambers. Due to high velocities in the expanding jet (see Figure 46) short residence times in the first chamber are assured for all excitation locations. How much the excitation before the Mach disk proves to be superior over excitation behind the Mach disk, or vice versa, has to be investigated experimentally.

REFERENCES

Addy, A.L., Effects of axisymmetric sonic nozzle geometry on Mach disk characteristics, AIAA Journal, 19 (1), 121-122, **1981**.

Anastasi, C. and Hancock, D.U., NO_2 kinetic studies using laser-induced fluorescence, Chem.Soc., Faraday Trans.2, 84 (10), 1697-1706, **1988**.

Anderson, J.B. and Fenn, J.B., Velocity distributions in molecular beams from nozzle sources, The Physics of Fluids, 8 (5), 780-787, **1965**.

Anderson, J.B., Andres, R.P., Fenn, J.B., and Maise, G., Studies of low density supersonic jets, in de Leeuw, ed., Rarefield Gas Dynamics, Academic Press, New York, 107-127, **1968**.

Ashkenas, H. and Sherman, F.S., The structure and utilization of supersonic free jets in low density wind tunnels, in de Leeuw, ed., Rarefield Gas Dynamics, Academic Press, New York, 84-105, **1968**.

Blevins, R.D., Applied fluid dynamics handbook, Van Nostrand Reinhold Company Inc., New York, **1984**.

Bradshaw, J.D., Rodgers, M.O., Sandholm, S., KeShent, S., and Davis, D.D., A two-photon laser-induced-fluorescence field instrument for ground-based and airborne measurements of atmospheric NO, J.Geophys.Res., 90, 12861-12873, **1985**.

Calvert, J.G. and Stockwell, W.R., Deviations from the O_3-NO-NO_2 photostationary state in tropospheric chemistry, Can.J.Chem., 61, 983-992, **1983**.

Carlslaw, H.S. and Jaeger, J.C., Conduction of heat in solids, Clarendon Press, Oxford, **1947**.

Chen, K., Wang, G., Kuo, C. and Pei, C., Vibrational analyses of the $^2B_2$-$^2A_1$ fluorescence spectra of NO_2 under dye laser excitations, Chem.Phys., 144, 383-389, **1990**.

Chuech, S.G., Lai, M.C., and Faeth, G.M., Structure of turbulent sonic underexpanded free jets, AIAA Journal, 27 (5), 549-559, **1989**.

Clinton, W.J. and Gore Jr., A., The climate change action plan, **1993**.

Crist, S., Sherman, P.M., and Glass, D.R., Study of the highly underexpanded sonic jet, AIAA Journal, 4 (1), 68-71, **1966**.

Crutzen, P.J. and Gidel, L.T., A two-dimensional photochemical model of the atmosphere 2: the tropospheric budgets of the anthropogenic chlorocarbons CO, CH_4, CH_3Cl and the effect of various NO_x sources on tropospheric ozone, J.Geophys.Res., 88 (C11), 6641-6661, **1983**.

Cumber, P.S., Fairweather, M., Falle, S.A.E.G., and Giddings, J.R., Predictions of the structure of turbulent, moderately underexpanded jets, Journal of Fluids Eng., 116, 707-713, **1994**.

Cumber, P.S., Fairweather, M., Falle, S.A.E.G., and Giddings, J.R., Predictions of the structure of turbulent, highly underexpanded jets, Journal of Fluids Eng., 117, 599-603, **1995**.

Davidor, W. and Penner, S.S., Shock standoff distances and Mach-disk diameters in underexpanded sonic jets, AAIA Journal, 9 (8), 1651-1653, **1971**.

Delon, A. and Jost, R., Laser induced dispersed fluorescence spectra of jet cooled NO_2: The complete set of vibrational levels up to $10000cm^{-1}$ and the onset of the X^2A_1-A^2B_2 vibronic interaction, J.Chem.Phys., 95 (8), 5686-5700, **1991**.

Di Rosa, M.D., Chang, A.Y., and Hanson, R.K., Continuous wave dye- laser technique for simultaneous, spatially resolved measurements of temperature, pressure, and velocity of NO in an underexpanded free jet, Applied Optics, 32 (21), 4074-4087, **1993**.

Donnelly, V.M. and Kaufman, F., Fluorescence lifetime studies of NO_2. I. Excitation of the perturbed $^2B_2$ state near 600nm, J.Chem.Phys., 66 (9), 4100-4110, **1977**.

Donnelly, V.M. and Kaufman, F., Mechanism of NO_2 fluorescence quenching, J.Chem.Phys., 67 (10), 4768-4769, **1977**.

Donnelly, V.M. and Kaufman, F., Reply to comment on mechanism of NO_2 fluorescence quenching, J.Chem.Phys., 68 (12), 5671, **1978**.

Donnelly, V.M. and Kaufman, F., Fluorescence lifetime studies of NO_2. II. Dependence of the perturbed $^2B_2$ state lifetimes on excitation energy, J.Chem.Phys., 69 (4), 1456-1460, **1978**.

Dulcey, C.S., McGee, T.J. and McIlrath, T.J., Laser induced fluorescence in NO_2: absolute fluorescence cross sections and quantum yields, Chem.Phys.Letters, 76 (1), 80-84, **1980**.

Fehsenfeld, F.C., Drummond, J.W., Roychowdhury, U.K., Galvin, P.J., Williams, E.J., Buhr, M.P., Parrish, D.D., Huebler, G., Langford, A.O., Calvert, J.G., Ridley, B.A., Grahek, F., Heikes, B.G., Kok, G.L., Shetter, J.D., Walega, J.G., Elsworth, C.M., Norton, R.B., Fahey, D.W., Murphy, P.C., Hovermale, C., Mohnen, V.A. Demerjian, K.L., Mackay, G.I., and Schiff, H.I., Intercomparison of NO_2 measurement techniques, J.Geophys.Res., 95 (D4), 3579-3597, **1990**.

Finlayson-Pitts, B.J. and Pitts Jr., J.N., Atmospheric chemistry: fundamentals and experimental techniques, Wiley and Sons, New york, **1986**.

Fleagle, R.G. and Businger, J.A., Academic Press, New York and London, **1963**.

Fujimoto, T., Kato, S., Usami, M., Niimi, T., and Kamiya, S., A study on the structure of free-jets of mixture by laser-induced fluorescence, Rarefield Gas Dynamics, Edited by H. Oguchi, University of Tokyo Press, 467-475, **1984**.

George, L.A., Development of a direct, low pressure, laser-induced fluorescence measurement technique for NO_2, ambient measurements and urban NO_x chemistry, PhD Thesis, Portland State University, Portland/OR, **1991**.

George, L.A. and O'Brien, R.J., Prototype FAGE determination of NO_2, J.Atmosph.Chem., 12, 195-209, **1991**.

Gerald, L., Gregory, G.L., Hoell Jr., J.M., Torres, A.L., Carrol, M.A., Ridley, B.A., Rodgers, Bradshaw, J., Sandholm, S.T., and M.O., Davis, An intercomparison of airborne nitric oxide measurements: a second opportunity, J.Geophys.Res., 95 (D7), 10129-10138, **1990**.

Giles, R.V., Fluid mechanics & hydraulics, Schaums Outline Series, McGraw-Hill Book Company, New York, **1962**.

Gillispie, G.D., Khan, A.U., Wahl, A.C., Hosteny, R.P. and Kraus, M., The electronic structure of NO_2. I. Multiconfiguration self-consistent-field calculation of low-lying electronic states, J.Chem.Phys., 63 (8), 3425-3443, **1975**.

Graedel, T.E. and Crutzen, J.P., Atmospheric change- an earth system perspective, Freeman and Company, New York, **1993**.

Gregory, G.L., Hoell Jr., J.M., Carrol, M.A., Ridley, B.A., Davis, D.D., Bradshaw, J., Karecki, D.R., Rodgers, M.O., Sandholm, S.T., Schiff, H.I., Hastie, D.R., Karecki, D.R., Mackay, G.I., Harris, G.W., Torres, A.L., and Fried, A., An intercomparison of airborne nitrogen dioxide instruments, J.Geophys.Res., 95 (D7), 10103-10127, **1990**.

Guthrie, A., Vacuum technology, Wiley & Sons, **1963**.

Hard, T.M., O'Brien, R.J., Chan, C.Y., and Mehrabzadeh, A.A., Tropospheric free radical determination by FAGE, Environ.Sci.Technol., 18, 768-777, **1984**.

Hardwick, J.L., Quantum ergodicity in small molecules: The continuum fluorescence of NO_2, J.Mol.Spec., 85-89, 109, **1985**.

Hemond, H.F. and Fechner, E.J., Chemical fate and transport in the environment, Academic Press, San Diego, **1994**.

Herzberg, G., Molecular spectra and molecular structure. III. Electronic spectra and electronic structure of polyatomic molecules, D.Van Nostrand Company, Inc., Princeton, New Jersey, **1966**.

Hiraoka, S., Shibuya, K. and Obi, K., Laser-induced fluorescence excitation spectrum of rotationally cooled NO_2 in the region 500-550nm, J.Mol.Spec., 126, 427-435, **1987**.

John, J.E.A., Gas dynamics, Allyn and Bacon, Inc., Boston, **1969**.

Keil, D.G., Donnelly, V.M. and Kaufman, F., Fluorescence lifetime studies of NO_2. IV. Temperature dependence of fluorescence spectra and of collisional quenching of fluorescence, J.Chem.Phys., 73 (4), 1514-1520, **1980**.

Kizirnis, S.W., Garcia Jr., F., Schreiber, P.W. and Gupa, R., Direct measurement of quenching cross sections of NO_2 by He, Ar and N2, J.Phys.B: At.Mol.Phys., 17, 2875-2881, **1984**.

Logan, J.A., Nitrogen oxides in the troposphere: global and regional budgets, J.Geophys.Res., 88 (C15), 10785-10807, **1983**.

Koichi Kurita, Takashi Okai, Kazuaki Ueno, Noriyuki Kawada and Mitsuo Kato, Velocity and temperature distributions in an underexpanded supersonic jet by using a laser induced fluorescence, Analytical Sciences, 7, Supplement, 1459-1462, **1991**.

Lewis Jr., C.H. and Carlson, D.J., Normal shock location in underexpanded gas and gas-particle jets, AIAA Journal, 2 (4), 776-777,**1964**.

McAndrew, J.F., Preses, J.M.Weston Jr., R.E. and Flynn, G., Infrared fluorescence from NO_2 excited at 400-500nm, J.Chem.Phys., 90 (9), 4772-4782, **1989**.

Mehrabzadeh, A., O'Brien, R.J., and Hard, T.M., Generalized response of chemiluminescence analyzer, Rev.Sci.Instr., 54, 1712-1718, **1983**.

Mises v., F., Die Differential-und Integralgleichungen der Mechanik und Physik, Vol.II, F.Vieweg Verlag, Braunschweig, **1961**.

Muntz, E.P., The direct measurement of velocity distribution functions, in de Leeuw, ed., Rarefield Gas Dynamics, Academic Press, New York,129-149, **1968**.

Myers, G.H., Silver, D.M. and Kaufmann, F., Quenching of NO_2 fluorescence, J.Chem.Phys., 44 (2), 718-723, **1965**.

Noyes Jr., W.A. and Leighton, P.A., The photochemistry of gases, Dover Publications, Inc., New York, **1966**.

Okabe, H., Photochemistry of small molecules, Wiley, New York, **1978**.

Persch, G., Mehdizadeh, E. and Demtroeder, W., Vibronic level density of excited NO_2-states and its statistical analysis, Berichte der Bunsen Ges. fuer Physikal. Chemie, 92, 312-318, **1988**.

Sandholm, S.T., Bradshaw, J.D., Dorris, K.S., Rodgers, K.S. and Davis, D.D., An airborne compatible photofragmentation two-photon laser-induced fluorescence intrument for measuring background tropospheric levels of NO, NO_x, and NO_2, J.Geophys.Res., 95 (7), 10155-10161, **1990**.

Schneider, W., Moartgat, G.K., Tyndall, G.S. and Burrows, J.P., Absorption cross-sections of NO_2 in the uv and visible region (200-700nm) at 298K, J.Mol.Spec., 11, 100-110, **1987**.

Seinfeld, J.H., Atmospheric chemistry and physics of air pollution, Wiley & Sons, New York, **1986**.

Schofield, K., Atomic and molecular fluorescence as a stratospheric species monitor, J.Quant.Spectros.Radiat.Transfer., 17, 13-51, **1977**.

Singh, H.B., Salas, L.J., Ridley, B.A., Shetter, J.D., Donahue, N.M., Fehsenfeld, F.C., Fahey, D.W., Parrish, D.D., Williams, E.J., Liu, S.C., Huebler, G., and Murphy, P.C., Relationship between peroxyacetyl nitrate and nitrogen oxides in the clean troposphere, Nature, 318, **1985**.

Sommerfeld, A., Partial differential equations in physics, Academic Press, New York, **1949**.

Steinfeld, J.I., Molecules and radiation: an introduction to modern molecular spectroscopy, The MIT Press, Cambridge, **1978**.

Sugimoto, N., Takeuchi, N. and Takezawa, S., Time-resolved, dispersed laser-induced energy transfer effect, Jap.J.Appl.Phys., 21 (11), 1536-1538, **1982**.

Sugimoto, N., Takeuchi, N. and Takezawa, S., Rotational analysis of the $^2B_2(K'=1)$-$^2A_1(K''=0)$ subband of NO_2 at 464.9nm in the time-gated excitation spectrum, Chem.Phys.Letters, 99 (56), 475-478, **1983**.

The National Research Council, Nitrogen Oxides, National Academy of Sciences, Washington, D.C., **1977**.

U.S.Department of Energy, The climate change action plan: technical supplement, **1994**.

U.S.Goverment, U.S. climate action report, **1993**.

Wayne, R.P., Chemistry of atmospheres, Oxford Science Publications, Oxford, **1985**.

Wayne, R.P., Principles and applications of photochemistry, Oxford Science Publications, Oxford, **1988**.

Zucker, R.D., Fundamentals of gas dynamics, Matrix Publishers, Inc., **1977**.

Zapryagaev, V.I. and Solotchin, A.V., Three-dimensional structure of flow in a supersonic underexpanded jet, J.Appl.Mech.Tech.Phys., 32 (4), 503-506, **1991**.